UNIVERSIDADE FEDERAL DE PERNAMBUCO
CENTRO DE CENTRO DE TECNOLOGIA E GEOCIÊNCIAS
DEPARTAMENTO DE ENGENHARIA MECÂNICA
PROGRAMA DE PÓS-GRADUAÇÃO EM ENGENHARIA MECÂNICA

ELDER SOARES DA SILVA

EAFD-AA7075 COMPOSITES FABRICATED BY SPARK PLASMA SINTERING (SPS): experiments and electro-thermo-mechanical-microstructural simulation

Recife
2022

ELDER SOARES DA SILVA

EAFD-AA7075 COMPOSITES FABRICATED BY SPARK PLASMA SINTERING (SPS): experiments and electro-thermo-mechanical-microstructural simulation

Thesis submitted to the Post-Graduate Program in Mechanical Engineering of the Universidade Federal de Pernambuco in partial fulfilment of the requirements for the degree of Doctor of Science in Mechanical Engineering.

Concentration area: Materials Engineering and Manufacturing.

Advisor: Prof. Dr. Nadège Sophie Bouchonneau da Silva.

Co-advisor: Prof. Dr. Claude Estournès.

Recife

2022

Catalogação na fonte:
Bibliotecária Sandra Maria Neri Santiago, CRB-4 / 1267

S586 Silva, Elder Soares da.
EAFD-AA7075 composites fabricated by Spark Plasma Sintering (SPS): experiments and electro-thermo-mechanical-microstructural simulation / Elder Soares da Silva. – 2022.
117 f.: il., figs., tabs. e abrev.

Orientadora: Profa. Dra. Nadège Sophie Bouchonneau da Silva.
Coorientador: Prof. Dr. Claude Estournès.
Tese (Doutorado) – Universidade Federal de Pernambuco. CTG. Programa de Pós-Graduação em Engenharia Mecânica. Recife, 2022.
Inclui referências e apêndices.

1. Engenharia mecânica. 2. Spark plasma sintering. 3. Compósitos de matriz de alumínio. 4. Reaproveitamento de resíduos. 5. Metalurgia do pó. 6. Pó de aciaria elétrica. I. Silva, Nadège Sophie Bouchonneau da (Orientadora). II. Estournès, Claude (Coorientador). III. Título.

UFPE

621 CDD (22. ed.) BCTG/2022-436

ELDER SOARES DA SILVA

EAFD-AA7075 COMPOSITES FABRICATED BY SPARK PLASMA SINTERING (SPS): experiments and electro-thermo-mechanical-microstructural simulation

Thesis submitted to the Post-Graduate Program in Mechanical Engineering of the Universidade Federal de Pernambuco, Centro de Tecnologia e Geociências in partial fulfilment of the requirements for the degree of Doctor of Science in Mechanical Engineering. Concentration area: Materials Engineering and Manufacturing.

Approved in: 31/08/2022.

ACADEMIC JURY

_____

Profa. Dra. Nadège Sophie Bouchonneau da Silva (President)
Universidade Federal de Pernambuco

_____

Prof. Dr. Claude Estournès (External Examiner)
Université de Toulouse

_____

Prof. Dr. Ricardo Artur Sanguinetti Ferreira (Internal Examiner)
Universidade Federal de Pernambuco

_____

Profa. Dra. Yeda Medeiros Bastos de Almeida (External Examiner)
Universidade Federal de Pernambuco

_____

Profa. Dra. Danielle Guedes de Lima Cavalcante (External Examiner)
Universidade Federal da Paraíba

I dedicate this work to my family and everyone who contributed in any way to its realization.

ACKNOWLEDGEMENTS

I would like to thank Dr. Nadège Bouchonneau, from UFPE, for her orientation, friendship, and mainly for her support and patience, without which this work would not have been accomplished.

To thank Dr. Kléber Alves and Dr. Elizeth Alves for their help in defining the research topic and for providing the material tested as reinforcement in the AA7075 aluminum matrix, the EAFD. To Dr. Oscar de Araújo Filho for his support in supplying the AA7075 powder, for lending his laboratory for processing the starting powders and, mainly, for his teachings and incentive.

I would like to thank the whole CIRIMAT team, University of Toulouse, France, especially Claude Estournès for co-supervising the thesis and also for having guided me during the execution of the experiments performed at Plateforme Nationale de frittage Flash (PNF2-CNRS), Dr. Christophe Laurent for accepting to receive me at CIRIMAT and for contributing to the production of the papers, Geoffroy Chevallier for the technical support in the sintering of the samples, and Dr. David Mesguich for helping me in the characterization of the samples and contributing to the papers.

To my wife Tatiana Alves for her support, incentive and understanding. To my son Heitor Felipe for simply existing and being my source of inspiration and encouragement. To all my family, especially my mother Cacilda Ferreira, my sisters Vanessa, Valéria and Vangéssica, my grandparents, for the simple fact of being part of my life and especially for the encouragement and support.

To the professors of the PPGEM/UFPE for their valuable teachings. To the course colleagues who contributed a lot in the accomplishment of the disciplines through discussions about the studied subjects and for the friendship that contributed in some way to my personal and academic growth.

Finally, to all those who helped me directly and indirectly to make this work come true.

RESUMO

A utilização de resíduos industriais, como o Pó de Aciaria Elétrica (PAE), resíduos em pó recuperados após a produção de aço em fornos elétricos a arco, como reforço em AMCs ainda é pouco explorado, embora tenha mostrado potencial para melhorar algumas propriedades mecânicas do material base, tais como dureza e resistência. Com o objetivo de propor uma nova alternativa para o reaproveitamento do PAE, compósitos de matriz AA7075 reforçados com PAE, utilizando diferentes frações e tamanhos de partículas, foram produzidos. Os pós de partida foram processados utilizando um moinho tipo SPEX. A densificação das amostras de PAE-AA7075 foi realizada por meio da técnica Spark Plasma Sintering (SPS), em uma única etapa, sendo a amostra aquecida a partir da temperatura ambiente, a uma taxa de 100 °C/min, até 550 °C, sendo essa mantida por 15 min ou 30 min, dependendo da amostra. Durante esse patamar, uma pressão uniaxial de 100 MPa foi aplicada. Nenhum tratamento térmico adicional é executado. Para avaliar a influência da fração de PAE e tamanho de partícula nas propriedades mecânicas e na microestrutura do material compósito, testes de microdureza Vickers, microscopia óptica e microscopia eletrônica de varredura foram realizados nas amostras sinterizadas. Observações em MEV mostram que a distribuição das partículas de reforço no material é homogênea, sem aglomeração das partículas. A microdureza dos compósitos AA7075/PAE tende a aumentar com o aumento do teor de PAE, mostrando que o PAE apresenta potencial promissor para ser aplicado como reforço em compósitos matriz AA7075. O aumento máximo da microdureza ocorreu usando o PAE com tamanho de partícula menor que 53 μm (denominado G1), aumentando de 108 para 168 HV com os teores de PAE de 0 a 15% em peso, respectivamente, correspondendo a um aumento máximo de 55,6% em relação à microdureza do material de base. O Método dos Elementos Finitos (MEF) foi utilizado como ferramenta preditiva para obter a melhor rota de densificação pela técnica SPS. Ao comparar os resultados obtidos por meio da simulação com os resultados experimentais, foi possível notar que as curvas de densificação são muito semelhantes, o que valida o estudo realizado e comprova que o MEF é uma boa ferramenta preditiva do processo SPS e das propriedades dos materiais resultantes.

Palavras-chave: spark plasma sintering; compósitos de matriz de alumínio; reaproveitamento de resíduos; metalurgia do pó; pó de aciaria elétrica.

ABSTRACT

The use of industrial waste, such as Electric Arc Furnace Dust (EAFD), the generic name for powdered waste recovered after the production of steel in electric-arc furnaces, as reinforcement in AMCs is still little explored, although it has shown potential to improve some mechanical properties of the base material, such as hardness and strength. Aiming to propose a new alternative for the reuse of EAFD, AA7075 matrix composites reinforced with EAFD, using different fractions and particle sizes, were produced. The starting powders were processed using a SPEX type ball mill. The densification of the EAFD-AA7075 samples was performed using the innovative Spark Plasma Sintering (SPS) technique, in a single step, where the sample was heated from room temperature at a rate of 100 °C/min to a temperature of 550° C, this temperature was maintained for 15 min or 30 min, depending on the sample. During this process, a uniaxial pressure of 100 MPa was applied. No further heat treatment is carried out. To evaluate the influence of EAFD fraction and particle size on the mechanical properties and the microstructure of the composite material, Vickers microhardness, optical microscopy and scanning electron microscopy (SEM) tests were carried out on the sintered samples. Observations in SEM show that the distribution of the reinforcement particles in the material is homogeneous, without agglomeration of the particles. The microhardness of AA7075/EAFD composites tends to increase with increasing EAFD content, showing that EAFD presents promising potential to be applied as reinforcement in AA7075 matrix composites. The maximum increase in microhardness occurred using EAFD with particle size smaller than 53 μm (termed G1), increasing from 108 to 168 HV with the EAFD contents from 0 to 15% by weight, respectively, corresponding to a maximum increase of 55.6% over the microhardness of the base material. Finite Element Method (FEM) was used as a predictive tool to obtain the best densification route by the SPS technique. By comparing the results obtained through simulation with the experimental results, it was possible to notice that the densification curves are very similar, which validates the study and proves that FEM is a good predictive tool for the SPS process and the resulting material properties.

Keywords: spark plasma sintering; aluminum matrix composites; waste reuse; powder metallurgy; electric-arc furnace dust.

LIST OF FIGURES

LIST OF TABLES

LIST OF ABREVIATIONS

ASR	Auto Shredder Residue
CIRIMAT	Centre Interuniversitaire de Recherche et d'Ingénierie des Matériaux
CNRS	Centre national de la recherche scientifique
EPA	Environmental Protection Agency
ETMM	Electro-thermo-mechanical-microestrutural
EAF	Electric-Arc Furnace
HIP	Hot Isostatic Pressing
HP	Hot Pressing
IAB	Instituto Aço Brasil
FEM	Finite Element Method
EAFD	Electric-Arc Furnace Dust
PNF²	Plateforme Nationale de Frittage Flash (French)
SPS	Spark Plasma Sintering
UFPE	Universidade Federal de Pernambuco

LIST OF SYMBOLS

E	Young modulus/elasticity
ε	Strain
ν	Poisson coefficient
k	Thermal conductivity
$\vec{J}$	Current density
$\vec{E}$	Electric field
σ	Electrical conductivity
C_p	Calorific capacity
λ	Thermal conductivity
T	Temperature
ϕ_c	Heat flow by conduction
σ_s	Stefan–Boltzmann constant
$\dot{q}$	Heat flow
h_{cr}	Thermal conductance
K_p	Proportional gain
K_i	Intregrative gain
K_d	Derivative gain
$\sigma(W)$	Effective mechanical stress
W	Equivalent strain rate
φ	Shear modulus
ψ	Bulk modulus
$\dot{e}$	Shrinkage rate
P_L	Effective sintering stress
θ	Porosity of the material
K	Consistency factor
$\dot{\gamma}$	Shape change rate
$\underline{\sigma}$	Stress tensor
A	Power law frequency factor
r_p	Pore radius

CONTENTS

1 INTRODUCTION

According to the Instituto Aço Brasil (IAB), Brazil is the 9th largest producer of crude steel, with 1.9% of world production in 2020, and the largest steel producer in Latin America, accounting for 55.9% of production. Brazilian steelmakers consumed 5.46 million tons of iron and steel scrap from external sources and 2.50 million tons produced in-house as raw material in 2020 (IAB, 2020). It is estimated that 1.13 tons of scrap is needed to produce 1 ton of steel (CIUCCIO, 2004 apud RECKZIEGEL et al., 2012).

Among the various residues, the Electric Arc Furnace Dust (EAFD) must be given special attention, as they contain chemical components that are harmful to nature and human health. EAFD is generated during the melting of ferrous scrap in an electric arc furnace (EAF) and collected by large bag filters. The EAF, designed to manufacture steel from recycled ferrous scrap, as the main filler material, mixed with pig iron and/or direct-reduced iron, co-produces between 15 to 25 kg of EAFD per ton of steel (ARAÚJO; SCHALCH, 2014; GUÉZENNEC *et al.*, 2005). With the growing need for steel production and the preservation of natural resources, through reuse and recycling, it is necessary to develop alternatives to reuse the waste generated in the production process, to reduce the amount of waste disposed in industrial landfills, which has become a major environmental problem. The inadequate management of industrial waste can contaminate soils, rivers, and groundwater and, consequently, affect public health. On the other hand, the concern with the amount of waste has become more present in steel companies because the legislation has also become more stringent. Economically, reusing the waste would help to reduce the costs of extracting raw materials and disposing of them in industrial landfills. Greater efficiency in the reuse of waste can also bring benefits to the company's image before society, as good environmental practices reveal a vision of commitment to the future of humanity.

Therefore, despite it is considered a renewable resource (MUHD *et al.*, 2017) and a secondary ray material (HAMUYUNI *et al.*, 2018), finding a suitable use for the EAFD represents a strong challenge and some studies have reported its recycling as filler in composite materials with polymer (BARRENECHE *et al.*, 2014; NIUBÓ *et al.*, 2009), ceramic (STATHOPOULOS *et al.*, 2013b), cement (ALSHEYAB; KHEDAYWI, 2013), concrete- (MUHD *et al.*, 2017), metal-matrix (ADEOSUN *et al.*, 2012; FLORES-VÉLEZ *et al.*, 2001; OLIVEIRA ALVES *et al.*, 2018), among others (LEDESMA *et al.*, 2017; METZ *et al.*, 2020; STATHOPOULOS *et al.*, 2013b). This approach has shown itself to be a promising alternative, presenting advantages to the environment by stabilizing harmful elements.

Regarding the metal-matrix, aluminum-matrix composites (AMCs) in particular are of great interest because alloys such as the 7075 aluminum alloy (AA7075) exhibit characteristics (low density, high strength-to-weight ratio) which are of a great importance, including for applications in the automotive, aeronautics and naval industries. The incorporation of EAFD into aluminum matrix composites also proved to be a good alternative and in some cases the composites produced showed improvements in mechanical properties, notably on the mechanical resistance and microhardness in relation to the base material (ADEOSUN *et al.*, 2012; FLORES-VÉLEZ *et al.*, 2001; OLIVEIRA ALVES *et al.*, 2018). However, this approach needs further studies.

In this context, this work proposes to develop new metallic materials, in particular low-cost metallic composites in which the waste will be used as reinforcement. For this, an innovative manufacturing technology, called Spark Plasma Sintering (SPS), will be used. If the results are promising, the methodology applied can help companies to reduce costs with the disposal of this waste, as well as add value to these steel-making co-products.

The Spark Plasma Sintering (SPS) technique has great potential to produce parts very close to the final size and shape in a single step (it can be considered a near-net-shape manufacturing technology), requiring a minimum number of finishing processes, such as machining, and also to avoid waste (ARNAUD et al., 2015; MANIÈRE et al., 2016b, 2017b). The finite element method (FEM) is widely used to develop predictive models to evaluate the sample properties and the final densification state of the material (such as ceramics, metals and polymers) with very good approximation (MANIÈRE et al., 2016d, 2016c). To understand and advance of SPS technology, it has become necessary to develop efficient numerical models capable of representing and simulating coupled multiphysics phenomena involving the thermal, mechanical and chemical of materials. One of the most promising commercial software for dealing with associated problems is COMSOL Multiphysics®. This software is a particularly suitable tool for developing such simulations, as it allows, through the use of specific modules (each of these modules integrating specific equations), the implementation and simulation of coupled multiphysics phenomena (COMSOL, 2018).

Therefore, due to the lack of studies about incorporating steel residues in metal matrix composites and the potential shown in these few applications (ADEOSUN *et al.*, 2012; FLORES-VÉLEZ *et al.*, 2001), the present work aims to investigate the influence of the addition of the EAFD on the mechanical properties on aluminum matrix composites AA7075. These composites will be fabricated using the Spark Plasma Sintering (SPS) technique, using

different percentages of residues. Microstructure characterization tests (SEM-FEG, EBSD, among others) will be conducted on the materials produced.

In addition, for the understanding of the phenomena involved in the SPS of composites and the development of a predictive tool to produce new materials with a complex shape, an electro-thermo-mechanical-microstructural numerical modeling based on finite elements will be performed, using the commercial software COMSOL Multiphysics®.

Finally, this work is justified by the potential economic, environmental, and scientific gains that it may provide.

1.1 OBJECTIVES

In this section the general objective (1.1.1) and the specific objectives (1.1.2) of the work are presented.

1.1.1 General objective

The objective of this work is to produce an AA7075 aluminum alloy matrix composite reinforced with Electric Arc Furnace Dust (EAFD) waste manufactured by Spark Plasma Sintering technique and to develop a predictive electrothermal-mechanical-microstructural (ETMM) numerical model based on the Finite Element Method.

1.1.2 Specific objectives

The specific objectives of this study are as follows:

a) Characterize the Electric Arc Furnace Dust (EAFD);

b) Metallographic preparation to determine the mechanical and microstructural properties of AA7075 aluminum alloy matrix composites reinforced with the waste Electric Arc Furnace Dust - EAFD manufactured by the Spark Plasma Sintering technique;

c) Realize the microstructural characterization (Scanning Electron Microscopy with Field Emission (SEM-FEG)) of the materials manufactured by SPS, to obtain the diagrams of the sintering process and the evolution of the grain size as a function of densification;

d) Study of the SPS sintering mechanisms and determine the creep parameters of the materials produced by SPS, using the methodology developed at CIRIMAT-France (MANIÈRE et al., 2016a; MARTINS et al., 2017). This procedure will be done initially with the base material (aluminum alloy AA7075 without any addition of residue) and then with the composites;

e) Compare the results of finite element simulations with experimental densification tests to validate the predictive model.

2 LITERATURE REVIEW

This chapter is dedicated to the literature review of the manuscript. Section 2.1 presents the Spark Plasma Sintering (SPS) technique, section 2.2 presents aspects of the modeling of the SPS technique by the finite element method (FEM), section 2.3 deals with the electric arc furnace dust (EAFD) residue, section 2.4 deals with the aluminum alloy used as base material for the fabrication of AA7075/EAFD composites and, finally, section 2.5 is about crystallite size and micro-strain determination.

2.1 SPARK PLASMA SINTERING (SPS)

The increasing demands on the properties of structural materials as multifunctional materials lead to stringent demands on the control of microstructure and multiscale architecture. When the characteristic dimensions are sub-micronic or nanometric, it is no longer possible to use conventional melting/solidification technologies (for metals) and natural sintering technologies (for ceramics), since these techniques involve high temperatures or very long production times that cause excessive grain growth of the materials.

This has led to the development of unconventional sintering techniques, including spark plasma sintering (SPS), which has had a very important global development in the last twenty years, after being used mainly in Japan (GRASSO; SAKKA; MAIZZA, 2009; GUILLON *et al.*, 2014; MUNIR; QUACH; OHYANAGI, 2011; ORRÙ *et al.*, 2009). Spark plasma sintering is a high-speed powder consolidation/sintering technology, capable of processing all types of conductive and non-conductive materials (metals and alloys, ceramics, polymers, and composites). This technology allows to obtain pieces with personalized shapes, from the simplest to the most complex. In addition, this technique offers a potential for the development of multimaterials with the possibility of reactive sintering *in situ*. The main difference between SPS and other pressing assisted sintering techniques lies in the fact that there is no furnace in the SPS technique. An electric current applied through electrodes flows through the pressure cell and, eventually, through the sample, according to its electrical conductivity (ANSELMI-TAMBURINI *et al.*, 2005). The cell thus acts as a heat source, which allows high heating rates (up to 1000 °C/min) to be achieved and ensures good heat transfer to the sample. In addition, the low inertia of the system allows for a rapid decrease in temperatures at which the diffusion processes are insignificant.

Fundamentally, it is difficult to separate the intrinsic effects of the current from its thermal effect (Joule effect), as temperature and current are not independent parameters. Studies have been conducted on the specific effects and mechanisms that can cause this mode of heating. The main researchers of the SPS technique are based on hypotheses and propose conclusions that are sometimes fundamentally opposite about the phenomena involved in SPS (HULBERT et al., 2008; LANGER; HOFFMANN; GUILLON, 2009; AMAN; GARNIER; DJURADO, 2011; SANTANACH et al., 2011; MARDER et al., 2014a, 2014b, 2015).

The choice of the SPS technique for the consolidation of the samples in the present work is justified by its great potential to produce parts very close to the size and the final shape in a single step (it can be considered a near-net-shape manufacturing technology), requiring a minimum number of finishing processes, such as machining, and also for avoiding waste (ARNAUD et al., 2015; MANIÈRE et al., 2016b, 2017b); its wide application spectrum, which can be applied to the consolidation of all types of materials; ability to produce parts with controlled microstructure; efficient production with low energy consumption, when compared to traditional techniques; potential application of this process in industries, among others.

The context of the appearance and some important aspects about the SPS technique are presented in more detail in the following subsections.

2.1.1 Appearance and Development of SPS

The great interest of the powder metallurgy industry and of academy materials researchers in the SPS technique began about two decades ago, both for product manufacturing and for the research of advanced materials and development. Due to its great advantages over other sintering techniques, it has been used for the processing of nanostructured materials, amorphous materials, intermetallic components, metallic matrix and ceramic matrix composites, highly refractory metals and ceramics, functionally graded material (FGM), new materials wear-resistant, thermoelectric semiconductors, biomaterials, etc., which are largely difficult to sinter by common methods (TOKITA, 2013; ZHANG *et al.*, 2014).

According to Tokita (2013), a similar technique to SPS was first studied in Germany around 1910, which was a technique applied by electrical energization to consolidate a porous material. However, the first patent for a resistive sintering method was applied for in the United States by G.F. Taylor, who had the idea of applying an electric current during the hot

pressing of cemented carbides. (TAYLOR, 1933). Then, in 1944, also in the United States, Cremer patented a sintering method by Joule effect to consolidate copper, brass or aluminum powder materials in a spot-welding machine (CREMER, 1944). These techniques developed by Taylor (1933) and Cremer (1944) are considered the origin of a hot pressing (HP) technique, which commonly applies a high frequency induction heating method (TOKITA, 2013).

In 1966, Inoue filed a patent for a sintering apparatus activated / assisted by electric current, which had a mechanism for simultaneous application of an electric current and a mechanical pressure of about 10 MPa (INOUE, 1966a) and also the patent for the electric discharge sintering technique (INOUE, 1966b). According to Grasso, Sakka e Maizza (2009), Inoue was the pioneer of the method of sintering by pulsed electric current and considered the method of applying pressure and current waveforms.

In the 1980s, with the expiration of Inoue's patents (INOUE, 1966a, 1966b), several companies started to produce machines based on Inoue's inventions. Tokita (2015) states that the SPS method in modern form was developed by Sumitomo Coal Mining Co, Ltd. in 1989, constituting a new phase in powder technology, thanks to the improvement of hardware and software combined with the simultaneous application of high pulsed current and mechanical pressure. Inoue patented the first SPS machine to be commercialized worldwide in 1991, working for Sumitomo Coal Mining Co, Ltd. (GRASSO; SAKKA; MAIZZA, 2009).

2.1.2 Basic configuration of a typical SPS system

The basic configuration of a typical SPS system is shown schematically in Figure 1. The SPS system has a vertical uniaxial pressure device (Z-axis), where the water-cooled punches also serve as electrodes; a water-cooled reaction chamber, which can be evacuated; a pulsed direct current (DC) generator; units for control and measurement of the position on the Z-axis, temperature and pressure applied; parameter display unit and various safety devices. In an SPS experiment, an amount of powder mass is introduced into a die. The die can be built from several materials, such as carbon, tungsten carbide, refractory alloys, amoung others. (HUNGRÍA; GALY; CASTRO, 2009; TOKITA, 2013).

Figure 1 – SPS basic configuration of a typical SPS system

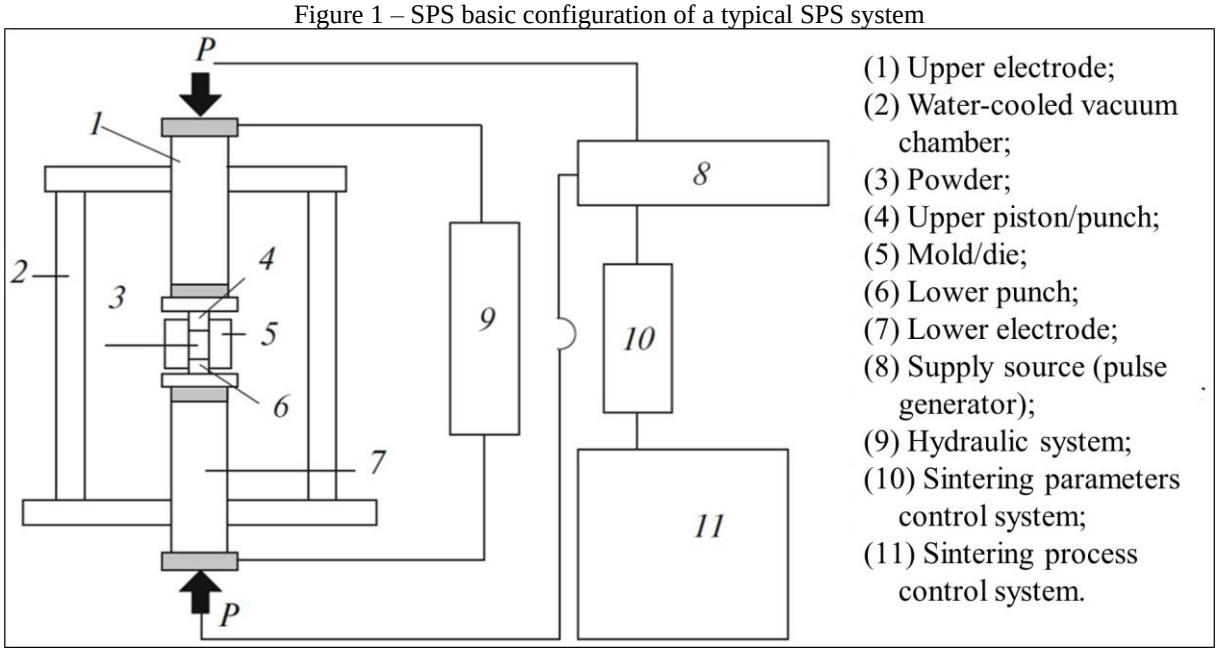

Source: Adapted from Tokita (2015).

Furthermore, it is worth mentioning that modern SPS devices include sophisticated control systems with feedback or programmed thermal cycles. These systems adjust the process parameters simultaneously and in real time. Automatic SPS machines allow simultaneous temperature control at various locations on the device. Limits for temperature changes are notified using an alert system (GRASSO; SAKKA; MAIZZA, 2009).

2.1.3 Advantage over Conventional Sintering

There are many advantages to using the SPS technique, this technology has some characteristics that offer wide possibilities for the development of new materials. Among the advantages of using SPS, compared to conventional sintering technologies, the following can be highlighted: Rapid sintering (heating rate up to 2000 °C/min); short consolidation times (in most cases 0-10 min); low sintering temperatures (200-300° C lower than most conventional sintering techniques, allowing the sintering of amorphous materials and magnetic materials below Curie temperature); low energy consumption, between 1/5 and 1/3, compared to conventional sintering techniques, such as sintering without pressure, hot pressing and hot isostatic pressing; reliable control of parameters of the sintering process and, as a result, control of the microstructure of the material; possibility of combining sintering methods, such as SPS – HP, SPS in a magnetic field, SPS – SHF (microwave), etc.; generation of

temperature gradients during sintering, enabling the sintering of functionally graded material; among many other advantages (TOKITA, 2013, 2015; ZHANG *et al.*, 2014).

2.1.4 Industrial applications

As mentioned before, SPS is considered a near-net shape technique, because it is able to produce parts very close to the final shape. This technique has been shown to be capable of manufacturing materials that would be difficult or even impossible to obtain through conventional manufacturing techniques.

Voisin, Monhoux and Couret showed that it is possible to produce titanium-aluminum jet engine turbine blades via SPS in one cycle, without any post-process thermal treatments. The blade obtained is shown in the Figure 2, in this work the finite element method was also applied to help optimize the results(VOISIN; MONCHOUX; COURET, 2019).

Figure 2 – Titanium-aluminum jet engine turbine blade produced via SPS.

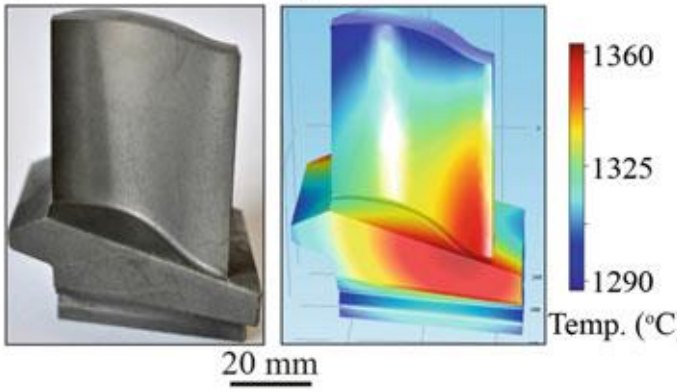

Source: Voisin; Monchoux; Couret (2019).

Today there are companies such as NORIMAT (NORIMAT, 2022) and SINTERMAT (SINTERMAT, 2022) that use the SPS technique to produce high value-added parts. According to information provided by these companies, through SPS it is possible to densify ultra-high strength ceramic materials (such as alumina, zirconia, composites, spinels) without changing the pigments used, and it is possible to produce ceramics with unprecedented colors: red, orange, pink or purple. By SPS, it is feasible to create high-performance components for use in the aerospace industry, enabling the creation of nearly net-shaped components in less than an hour of heat treatment. Numerous metals and alloys, including superalloys and intermetallics (TiAl), can be processed using this method. It is also

possible to produce military grade materials for ballistic applications (SiC, B4C, ZrB2) and production of high-performance cutting tools (thanks to spark plasma sintering, the production of tungsten carbide cutting inserts is improved).

Figure 3 shows some parts manufactured by SPS from NORIMAT.

Figure 3 – Applications of SPS in Industry

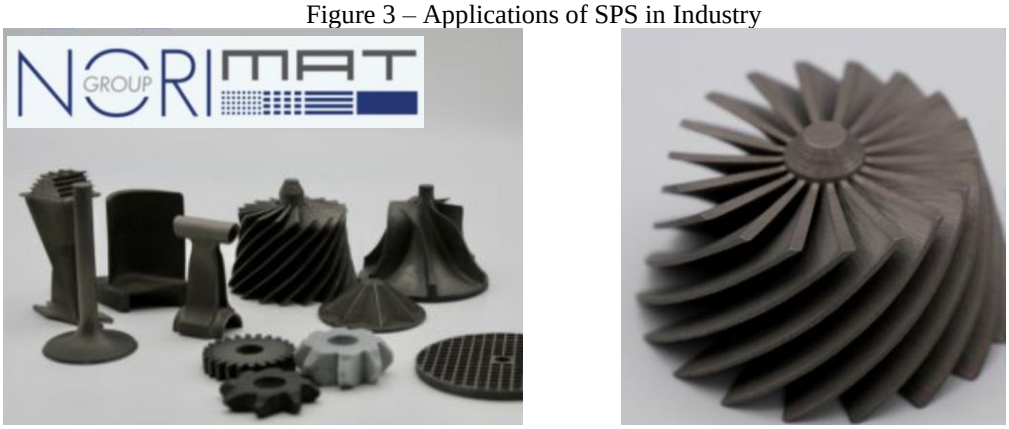

Source: Norimat (2022)

2.2 SPS MODELING BY THE FINITE ELEMENT METHOD

SPS allows high rates of consolidation and densification with negligible grain growth. However, despite many years of work and research on the subject by many researchers in the field of materials, many questions still remain unclear regarding both the mechanisms involved and the electrical and thermal behavior of the tools during the SPS cycles (PAVIA *et al.*, 2013; TOKITA, 2013). For this reason, it is important that theoretical and numerical analyzes are conducted in relation to the technique, in order to obtain approximate models capable of predicting some parameters at the end of the process such as: density, inhomogeneity, grain size, among others.

Numerical approaches using the Finite Element Method (FEM) have shown to be quite promising and reliable in several engineering areas to assess the behavior of materials or structures. FEM allows to implement complex models and perform simulations of the various phenomena involved, making it a more economical and faster method than experimental methods. Thus, the use of numerical simulation using the Finite Element Method (FEM) allows to answer some of these questions (VANMEENSEL *et al.*, 2005; ZAVALIANGOS *et al.*, 2004).

The finite element method is also widely used to develop predictive models, in order to assess the properties of the sample and the final state of densification of the material (such

as ceramics, metals and polymers) with very good approximation. The number of articles published on the simulation of SPS processes has increased dramatically since the 2000s, so as the development of Finite Element Modeling (FEM) softwares (MANIÈRE et al., 2016d, 2016c).

For the study of SPS technology, it became necessary to develop efficient numerical models capable of representing and simulating coupled multiphysical phenomena, involving the thermal, mechanics and chemistry of materials. One of the most promising commercial software for dealing with coupled problems is COMSOL Multiphysics®. This software is a particularly suitable tool for the development of such simulations, as it allows, through the use of specific modules (each of these modules integrating specific equations), the implementation and simulation of coupled multiphysical phenomena (COMSOL, 2018).

During the SPS process, the heating is generated by the Joule effect, which is generated by the passage of electrical current through a conductive material. At the interfaces of the parts in contact, as there is a discontinuity, it is important to consider the electrical and thermal losses in these regions in numerical modeling, in order to obtain more realistic models. Some important works in this line were also developed by CIRIMAT researchers (MANIÈRE *et al.*, 2016d, 2017a) and will serve as a basis for determining the thermal and electrical contact resistances in this work.

Finite Element modeling of SPS is very important and promising to optimize the sintering process, reduce the number of experiments and can also be used as a predictive tool. In the following sections, some works dealing with the use of FEM for numerical modeling of SPS are presented, from simple approaches to more complex approaches.

2.2.1 Electro-Thermal Modeling

This subsection presents the equations and the boundary conditions for performing the electro-thermal modeling of the SPS process.

2.2.1.1 Equations of the Electro-Thermal Model

The heating generated in the SPS process is due to an electrothermal phenomenon called the Joule effect, which is caused by the passage of current through a conductive material. The laws that describe the phenomenon must take into account the conservation of

electrical and thermal energy. Thus, in the simulation the current conservation eq. (1) and the heat eq. (2) are used.

$$\vec{\nabla} \cdot \vec{J} = \vec{\nabla} \cdot (\sigma \vec{E}) = \vec{\nabla} \cdot (-\sigma \vec{\nabla} U) = 0 \quad (1)$$

$$\vec{\nabla} \cdot (-\lambda \vec{\nabla} T) + \rho C_p \frac{\partial T}{\partial t} = \vec{J} \cdot \vec{E} \quad (2)$$

Where: $\vec{J}$ is the current density, $\vec{E}$the electric field, U the electric potential, σ the electrical conductivity, C_p the heat capacity, λ the thermal conductivity and T the temperature.

2.2.1.2 Boundary Conditions (Simplest Case)

Due to the axial symmetry of the SPS apparatus and the reduction in computational time, 2D axisymmetric geometries (Figure 4) are generally used to simulate the sintering process. In the simplest models, the electrical and thermal contact resistances at the interfaces of the parts are neglected, which does not correspond to reality. This simplification can only be done in cases where the compaction pressure is high, above 50 MPa (ANSELMI-TAMBURINI *et al.*, 2005). The importance of considering contact resistances will be discussed in the next section.

Figure 4 – Simplified boundary conditions

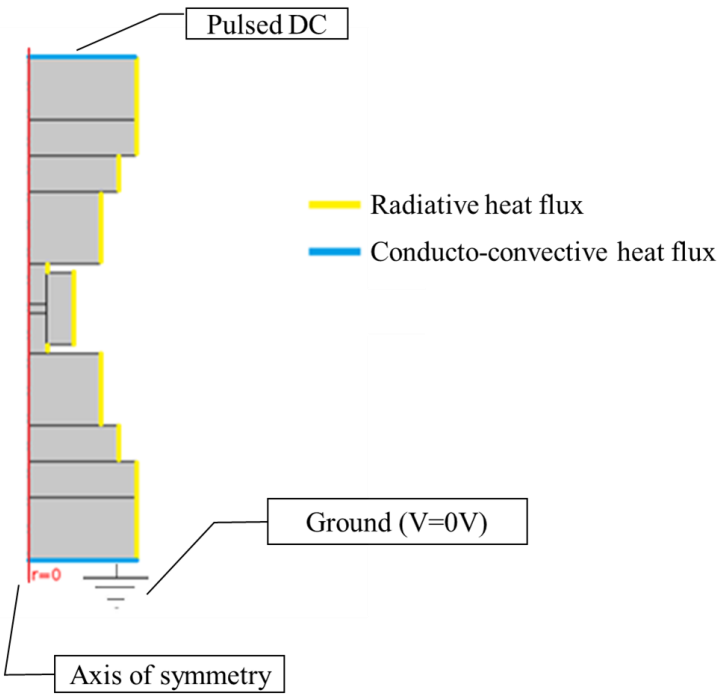

Source: The Author (2022)

The electrical boundary conditions are generally imposed by applying a voltage or an electric current to the top of the tool and the outer faces are considered electrically insulated (Figure 4). The thermal boundary conditions are conducto-convective heat flux (eq. (3)) in the areas in contact with the water-cooling circuit (condition represented by the blue lines), radiative heat flux (eq. (4)) on the outer vertical surfaces (condition represented by the yellow lines), and thermal insulation on the other horizontal surfaces. On the external vertical surfaces, convective heat flux is generally neglected, because the SPS chamber in most cases works in a vacuum.

$$\phi_c = h_c(T_i - T_w) \tag{3}$$

$$\phi_r = \sigma_s \varepsilon (T_e^4 - T_a^4) \tag{4}$$

In the eq. (3), ϕ_c represents the conductive heat flux; h_c, the convective coefficient; T_i, the surface temperature and T_w, the water-cooling circuit temperature. In the eq. (4), ϕ_r is the radiative heat flux; σ_s, The Stefan-Boltzmann constant; ε , the emissivity; T_e, the emission surface temperature; $T_{a,}$ the chamber temperature.

2.2.1.3 Boundary Conditions (With Contact Resistances)

In order to obtain a more realistic temperature distribution in the simulation throughout the SPS apparatus and in the sample (conductive or insulating), it is important that the electrical and thermal contact resistances (condition represented by the red lines in the Figure 5) are taken into account, especially the vertical contact resistances. In the outer horizontal areas, black lines in the Figure 5, the Comsol Multiphysics defaut boundary conditions (electrical and thermal insulation) are maintained.

Contact resistances are important to explain the sudden drops in temperature from one part to the other in the interfacial region (thermal gaps), which is verified experimentally with infrared thermal images (MANIÈRE *et al.*, 2016d). In addition, it serves to more accurately simulate the passage of current through the SPS column, making the current lines according to the experiment (ANSELMI-TAMBURINI *et al.*, 2005; PAVIA *et al.*, 2013). Figure 5 below shows where the boundary conditions of the contact resistances are applied.

Figure 5 – Boundary conditions (considering contact resistances)

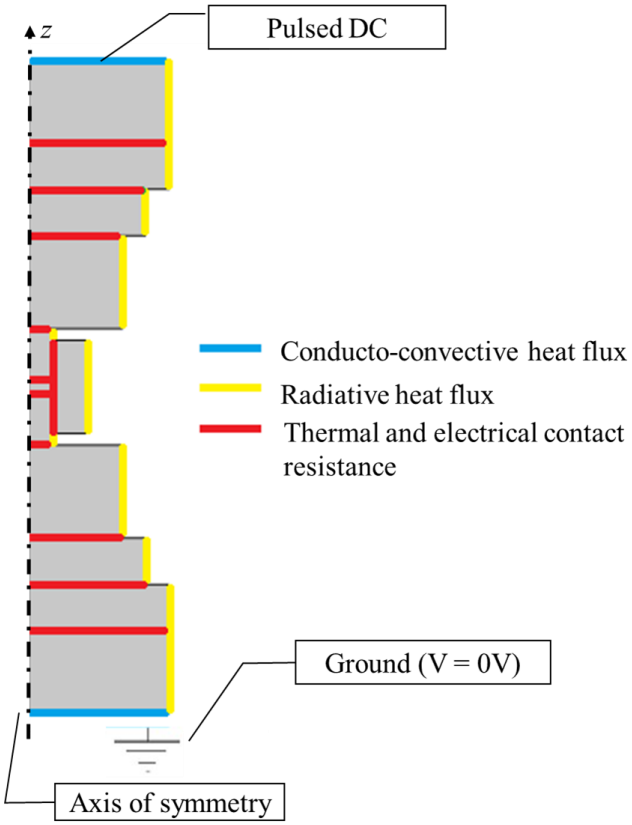

Source: The Author (2022)

When two parts are in contact, due to the roughness of the parts (irregularities in the geometry) and surface deposits, the thermal and electrical contact is not perfect, that is, the electrical potential and the temperature are discontinuous functions in the imperfect interfaces. Figure 6 illustrates this phenomenon schematically.

Figure 6 – Contact areas

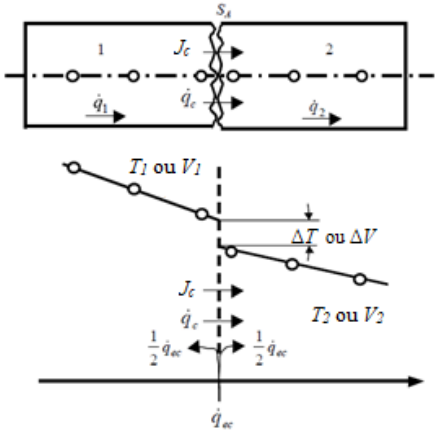

Source: Adapted of Zavaliangos et al. (2004).

Figure 6 represents the temperature drops, ΔT, or voltage, ΔV, in an imperfect interface with apparent contact area S_A, due to the thermal or electrical contact resistances. In addition, $\dot{q}_1$ and $\dot{q}_2$ are the heat flows in regions 1 and 2, respectively. It is important to point out that, due to the thermal contact resistance, Joule heating occurs, $\dot{q}_{ec}$, at the contact interfaces when there is an electric current flow (ZAVALIANGOS *et al.*, 2004).

It is important to point out that, due to the thermal contact resistance, Joule heating occurs, at the contact interfaces when there is an electric current passing through.

The current density (through the electrical contact), J_c, and the heat flux (through the thermal contact), $\dot{q}_c$, in the interface area between the parts, obeys eq. (5) and eq. (6), respectively:

$$J_c = \sigma_c(V_1 - V_2) \tag{5}$$

$$\dot{q}_c = h_{cr}(T_1 - T_2) \tag{6}$$

where: σ_c ($\Omega^{-1}m^{-2}$) and $h_{cr}(\mathrm{W/m^2K})$ are the contact electrical conductivity and convective coefficient, respectively. *V* and *T* are, respectively, the electrical potential and the temperature on each side of the contact interface.

2.2.1.4 Determination of Contact Resistances

As previously mentioned, the heating in the SPS is due to the Joule effect, due to the current flow through the SPS tooling and, in the sample, if it is an electrically conductive material. If the sample is not conductive, it will heat by thermal conduction, as it is in contact with a graphite mold and punches, which are conductive and heat up by the electrothermal effect.

Electrothermal modeling is important to know the temperature distribution throughout the sample, to allow better control and helps in the process of optimizing the temperature distribution in the sample, which can be either nearly constant, if the intention is to obtain a homogeneous sample, or to apply a gradient, if the intention is to create a functionally graded material sample.

Researchers from the University of Toulouse and CIRIMAT, France (MANIÈRE *et al.*, 2016d), developed a relatively simple methodology for determining the electrical and thermal contact resistances of SPS tooling, both for conductive and non-conductive samples.

The main advantage of this innovative methodology is that it allows to determine the set of contact resistances over the entire SPS column in a single test.

In the referred work, the authors performed SPS experiments using an open mold to reveal the distribution of internal temperature and highlight the effects of the predominant electrical and thermal contacts. They performed this procedure with dense samples, to avoid sintering and allow the construction of a finite element model that faithfully reproduces the experimental results. Figure 7 below shows the thermal infrared image of these experiments.

Figure 7 – Infrared thermal images of open mold containing sample of: (a) alumina (b) copper

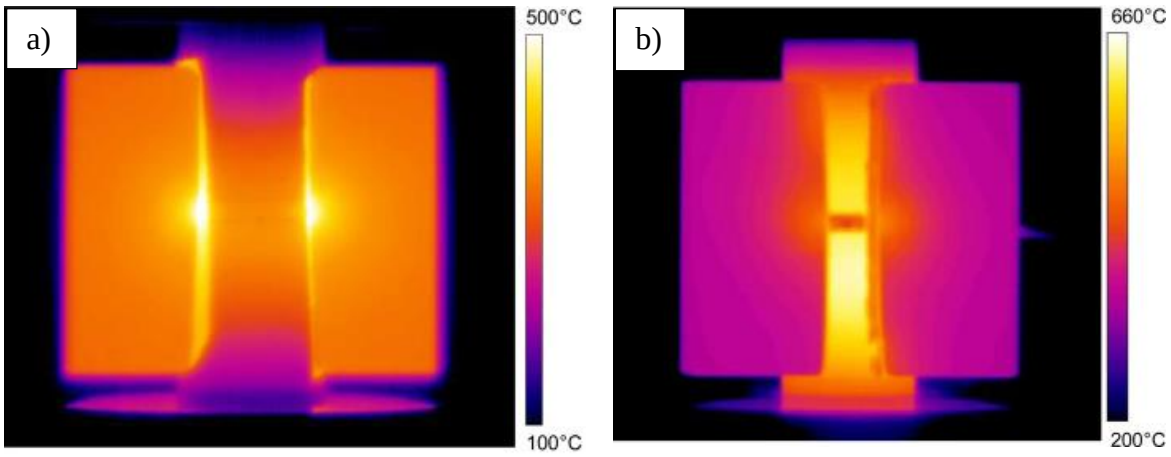

Source: Manière et al (2016d).

It is important to note in Figure 7 that when the sample is an insulating material (Figure 7a) the temperature of the graphite mold is higher than in the punch (also graphite), because the current is deflected by the mold (it does not pass through the sample). In the case of the conductive sample (Figure 7b), it is noticed that the temperature along the punches is higher than in the mold, because, in this case, the current tends to flow directly from the punch towards the copper sample (heating it directly by Joule effect). It is possible to notice that hot spots appear next to the non-conductive sample, indicating a strong contact resistance between sample and mold. These experiments were conducted on the SPS machine of the "Plateforme Nationale CNRS de Frittage Flash" located at the University of Toulouse III-Paul Sabatier (Dr. Sinter 2080, SPS Syntex Inc., Japan), the sample was heated from room temperature (20 °C) up to 1000 °C, with a heating rate of 100 K/min. The applied pressure was 100 MPa. Figure 8 shows the tool geometry of the SPS machine used and the contact regions studied in that work.

Figure 8 – SPS tooling and its contact regions

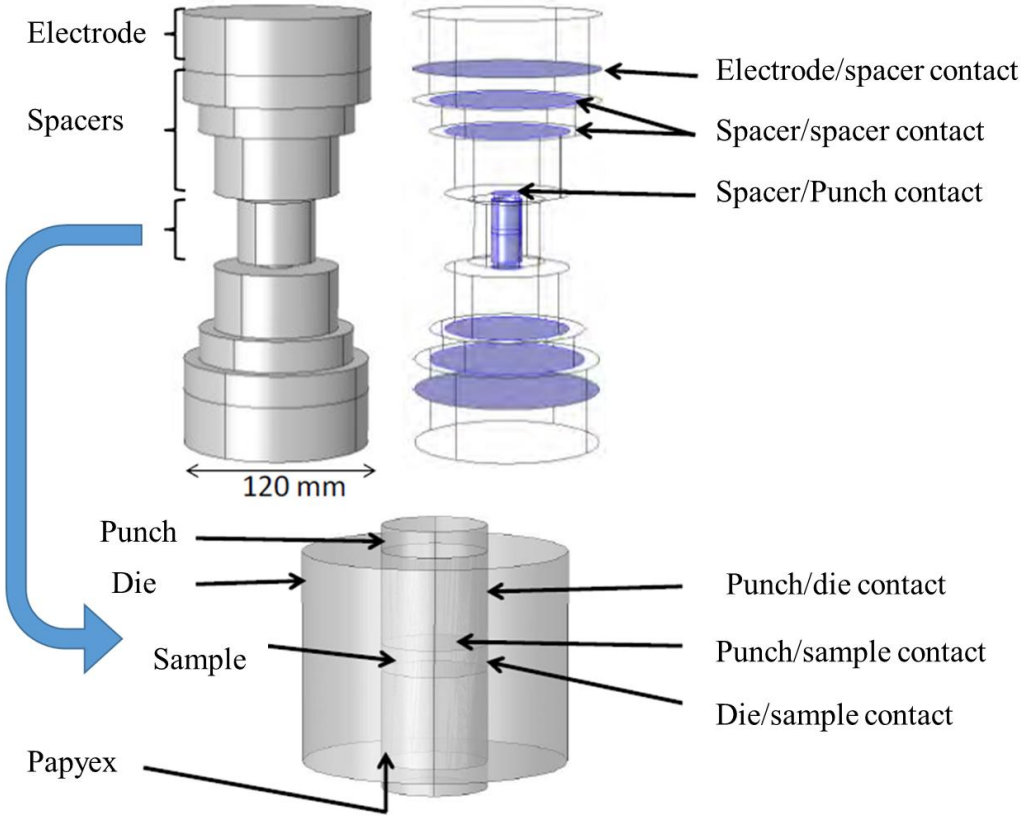

Source: Adapted from Manière (2015).

As described in the article (MANIÈRE *et al.*, 2016d), the calibration process is initiated by determining the horizontal contact resistances, specifically the contact resistance generated in the contact of the sample with the graphite punches, for different applied pressures. Initially, the current passing through the column without any sample is measured, I_0, then the configuration is modified, inserting a graphite sample between two graphite sheets (Papyex) and the current measurement is redone, obtaining a different current due to contacts, I_c. The contact resistance can be obtained by the difference in the current that passes through the column, maintaining the difference in electrical potential of the first case (MANIERE *et al.*, 2015).

Figure 9 shows in a schematic way this process of determining horizontal contact electrical resistances.

Figure 9 – Determination of horizontal contact resistances

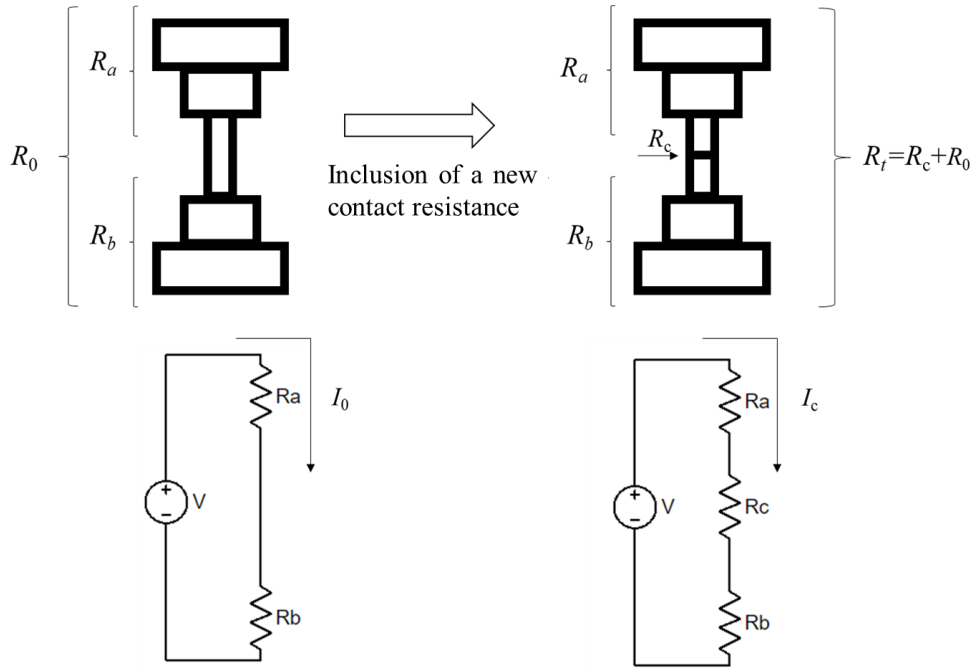

Source: The Author (2022)

Ohm's law (eq. (7)) states that the potential difference, *V*, is expressed as the product of the current, *I*, by the electrical resistance, *R*:

$$V = IR \tag{7}$$

If, during the process, the electrical potential is kept constant:

$$V = I_0 R_0 = I_1 R_1 = I_1 (R_0 + R_c) \tag{8}$$

Here the indexes 0 and 1 refer to the values before and after the addition of the contact resistance R_c (eq.(9)), respectively. Contact resistance can be achieved simply by:

$$R_c = \frac{V}{I_1} - R_0 = \frac{V}{I_1} - \frac{V}{I_0} = V\left(\frac{1}{I_1} - \frac{1}{I_0}\right) \tag{9}$$

For the determination of other horizontal contacts and vertical contacts, the authors use a reverse analysis where the graphite-Papyex-Graphite contact phenomena are studied experimentally and modeled by finite element calculations. The determination of experimental temperatures is done by placing thermocouples in specific regions of the SPS column.

Figure 10 shows the boundary conditions used in the modeling and the values of the contact resistances obtained in the calibration process.

Figure 10 – Boundary conditions used in modeling

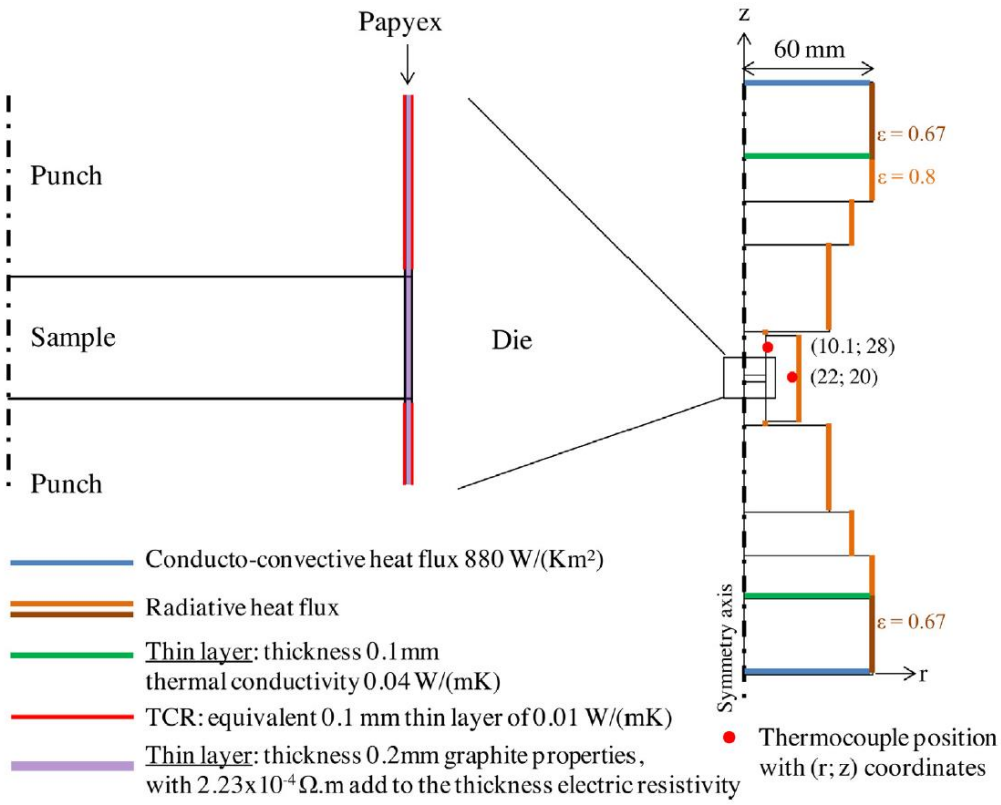

Source: Manière et al. (2016d).

Figure 11 shows the temperature profiles obtained through numerical simulation at the end of the calibration steps (Figure 11a) and the experimental temperature profile obtained by infrared thermography (Figure 11b).

Figure 11 – Comparison between temperature profiles: a) modeling and b) experimental

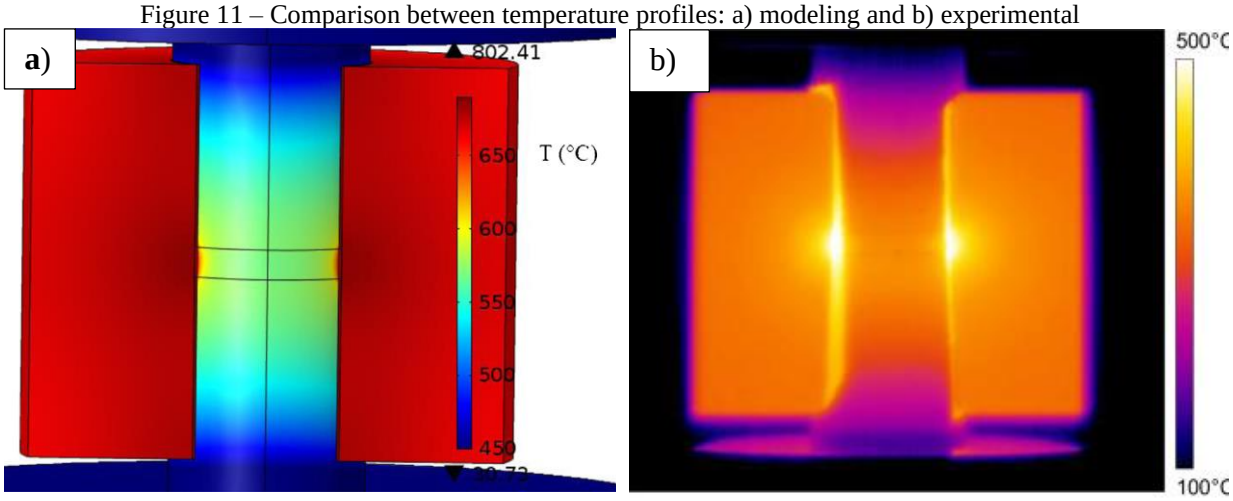

Source: Manière et al. (2016d).

Figure 12 compares the experimental heating curve, obtained by using thermocouples placed on the mold surface (blue circles) and on the Papyex (green squares), with those obtained in the numerical simulation (blue and green lines).

Figure 12 – Experimental heating curve obtained by modeling compared to the experiment

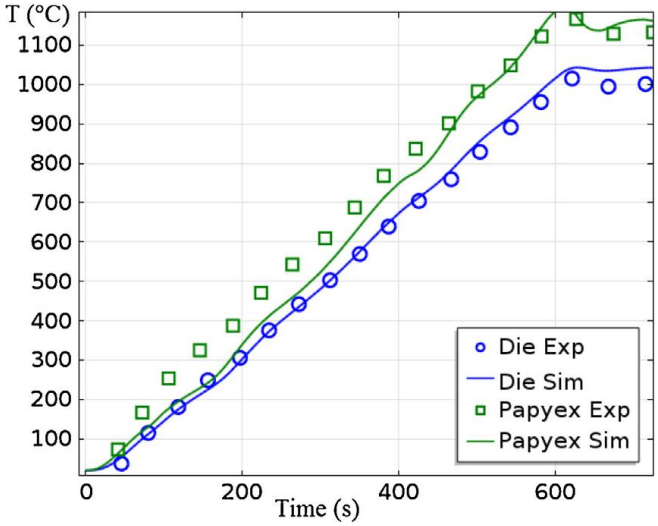

Source: Manière et al. (2016d).

The results presented in Figure 11 and Figure 12 show how efficient this methodology is, as it is noted that the simulations performed reproduce the experimental results very well.

Another approach taken by the same research group gave rise to a more general result, which is able to provide the values of the thermal and electrical contact resistances of the SPS device as a function of the geometric parameters of the "punch, mold and sample" system, taking into account the effect of the scale. These measurements were conducted under various conditions of temperature and pressure (MANIÈRE *et al.*, 2017a). The main results obtained are presented in Table 1.

Table 1 – Thermal and electrical contact resistances as a function of the temperature and geometry of the SPS device

ECR spacer/punch ($\Omega\,m^2$)	$5 * 10^{-9}\,\frac{(2000-T)}{(T-100)}$
TCR spacer/punch (m^2 K/W)	$5 * 10^{-6} + 3 * 10^{-5}\,\frac{(2000-T)}{(T-50)}$
TCR punch/sample (m^2 K/W)	$2.5 * 10^{-5} + 1.5 * 10^{-5}\,\frac{(2000-T)}{(T-50)}$
TCR sample/die (m^2 K/W)	$8 * 10^{-6} + 4 * 10^{-6}\,\frac{(2000-T)}{(T-80)}$
ρ_{ex} (punch/die) (Ω m)	$\left(1.7 * 10^{-3} - 9.5 * 10^{-7} * T\right) * F_e$
ρ_T (punch/die) (K m/W)	$\left(80 + 50\frac{(2000-T)}{(T-80)}\right) * F_T$

Source: Manière et al. (2017a).

In Table 1, F_T and F_e factors depend on the diameter of the punch Φ: $F_T = 3.11 \cdot 10^{-2} e^{1.15 \cdot 10^{-1} \Phi}$ and $F_e = 4.50 \cdot 10^{-2} \Phi - 3.67 \cdot 10^{-1}$.

For the ease of implementation, we will use the results obtained in this last work cited to determine the electrical and thermal contact resistances in this thesis.

2.2.1.5 Proportional-Integral-Derivative (PID) Controller

The PID controller is the most widely used feedback algorithm in control systems in the industry (in process control, it is estimated that more than 95% of the control loops are of the PID type). Feedback can reduce the effects of disturbances, can make the system insensitive to variations in the process, and can cause a system to faithfully follow its input signals (ASTRÖM; HÄGGLUND, 2009). This type of algorithm can also be applied to finite element computational models and has been widely used for temperature control in SPS modeling (MUÑOZ; ANSELMI-TAMBURINI, 2010; PAVIA et al., 2013; MANIÈRE et al., 2016c; SCHWERTZ et al., 2016).

As the name suggests, the PID controller involves three constant parameters (called a three-term control): the proportional *P*; the integral *I* and the derivative *D*. The integral action allows the PID controller to be able to eliminate errors in steady state, the derivative action allows to predict future errors (ASTRÖM; HÄGGLUND, 2009).

Defining $u(t)$ as the output signal (which may be voltage $V(t)$, current $i(t)$, current density $J(t)$), the PID controller algorithm is described by eq. (10) below:

$$u(t) = K_p e(t) + K_i \int_0^t e(t)\, dt + K_d \frac{de(t)}{dt} \tag{10}$$

Where K_p, K_i and K_d are constant denominated, respectively, proportional gain, integral gain and derivative gain, these constants must be determined for each process; t is time and e is the control error, which is the difference between the reference (or desired) value and the measured value of the process variable (provided by a sensor).

In finite element simulations regarding SPS, the process variable is temperature $T(t)$. Therefore, the control error $e(t)$ (eq. (11)) will be the difference between the setpoint temperature T_{sp} and the process temperature T, that is,

$$e(t) = \Delta T(t) = T_{sp}(t) - T(t) \tag{11}$$

For the implementation of the PID algorithm in COMSOL Multiphysics®, the point that will be used for temperature control must be established (as seen in Figure 13). For calculating the integral $\int_0^t e(\tau)\, d\tau$, the module Mathematics\Global ODEs and DAEs is used, which uses the following eq. (12):

$$\frac{dF(t)}{dt} = e(t), \tag{12}$$

with the initial conditions: $F(0) = 0$ e $\frac{dF(0)}{dt} = 0$.

Figure 13 – Temperature point probe

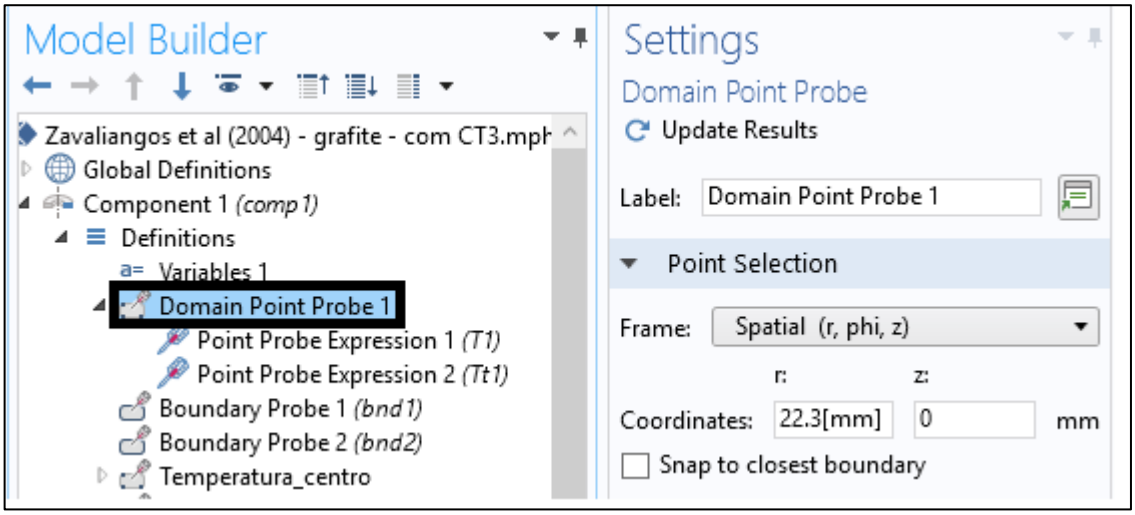

Source: The Author (2022)

Therefore, due to the fact that the PID controller is widely used in SPS modeling for temperature control, for its proven effectiveness and for the considerable simplicity of application, its algorithm will be used in the models presented in this work.

2.2.2 SPS Electro-Thermo-Mechanical Modeling

The application of mechanics in the modeling of SPS by finite elements requires the use of an adequate constitutive model, which is able to correctly describe the dependence of the mechanical properties of the material as a function of porosity. In this sense, one of the most used models to describe the densification of porous materials by SPS is the Olevsky

model (OLEVSKY, 1998; OLEVSKY *et al.*, 2012; OLEVSKY; TIKARE; GARINO, 2006; OLEVSKY; FROYEN, 2006), Cam-Clay model (SCHWERTZ *et al.*, 2016; VERMA; MAHESH; ANWAR, 2012) and Norton-Green model, which is also called the Abouaf model (ABOUAF *et al.*, 1988). In the present work, only the Olevsky model will be used, its mathematical description will be presented below.

2.2.2.1 Olevsky constitutive model

As mentioned earlier, Olevsky model (OLEVSKY, 1998; OLEVSKY *et al.*, 2005; OLEVSKY; KANDUKURI; FROYEN, 2007; OLEVSKY; TIKARE; GARINO, 2006; OLEVSKY; FROYEN, 2006) is one of the most used constitutive models in computational modeling, *via* finite elements, of the sintering kinetics of powder materials by spark plasma sintering. The reason for its wide use is the ability to predict, with good approximation, the final state of the microstructure of the consolidated material, including the prediction of porosity and final density, average grain size and even possible phase transitions. This model is based on concepts of the continuum theory and can encompass the dominant phenomena in SPS, such as: surface energy of the grain, electro-migration and loading effect.

According to Olevsky (1998), the development of a model linked to the mechanics of the continuum, based on the theories of plastic and viscous nonlinear deformation of pore bodies, for the analysis of the compaction of this type of material, arose from the need for the incorporation of macroscopic factors such as external forces applied, kinematic restrictions and heterogeneities in the properties in the sample under investigation. Also according to him, the original theoretical concepts, based on ideas of the discrete nature of particulate media, did not sufficiently address these questions mentioned above, which hindered their use.

As Olevsky et al. (2005) describes, eq. (13) presents the nonlinear viscous constitutive relationship between the external stresses applied (σ_{ij} corresponding to the components of the stress tensor) with the components of the strain rate tensor $\dot{\varepsilon}_{ij}$.

$$\sigma_{ij} = \frac{\sigma(W)}{W}\left[\varphi\dot{\varepsilon}_{ij} + \left(\psi - \frac{1}{3}\varphi\right)\dot{e}\delta_{ij}\right] + P_L\delta_{ij} \tag{13}$$

Where $\sigma(W)$ is the effective stress, W is the equivalent strain rate, φ is the normalized viscous shear modulus, ψ is the normalized viscous bulk modulus, $\dot{e}$ volume change rate, δ_{ij} is the Kronecker Delta ($\delta_{ij} = 1$ if $i = j$ or $\delta_{ij} = 0$ if $i \neq j$) and P_L the effective

sintering stress. φ, ψ and P_L can be written in terms of porosity, θ, respectively, as eq. (14), eq. (15) and eq. (16).

$$\varphi = (1-\theta)^2 \tag{14}$$

$$\psi = \frac{2}{3}\frac{(1-\theta)^3}{\theta} \tag{15}$$

$$P_L = P_{L0}(1-\theta)^2;\ P_{L0} = \frac{3\alpha}{r_0} \tag{16}$$

Physically, $\dot{e}$ represents the volume change rate of a porous body. Porosity θ is defined as the volumetric fraction of voids in a porous body.

Olevsky sintering model is based on the power-law creep (eq. (17)) defined for a viscous material, as follows:

$$\sigma(W) = KW^m \tag{17}$$

where W is the equivalent strain rate, $\sigma(W)$ is the equivalent stress, K is the consistency factor and m is a constant.

The equivalent strain rate W is dependent on the invariants of the strain rate tensor, defined by:

$$W = \frac{1}{\sqrt{1-\theta}}\sqrt{\varphi\dot{\gamma}^2 + \psi\dot{e}^2} \tag{18}$$

where $\dot{e}$ and $\dot{\gamma}$ are the volume change rate (eq. (19)) and the shape change rate (eq. (20)), respectively.

$$\dot{e} = \dot{\varepsilon}_x + \dot{\varepsilon}_y + \dot{\varepsilon}_z \tag{19}$$

$$\dot{\gamma} = \sqrt{2\left(\dot{\varepsilon}_{xy}^2 + \dot{\varepsilon}_{xz}^2 + \dot{\varepsilon}_{yz}^2\right) + \frac{2}{3}\left(\dot{\varepsilon}_x^2 + \dot{\varepsilon}_y^2 + \dot{\varepsilon}_z^2\right) - \frac{2}{3}\left(\dot{\varepsilon}_x\dot{\varepsilon}_y + \dot{\varepsilon}_x\dot{\varepsilon}_z + \dot{\varepsilon}_y\dot{\varepsilon}_z\right)} \tag{20}$$

The stress tensor $\underline{\sigma}$ is then defined by the eq.(21):

$$\boldsymbol{\sigma} = \frac{\sigma_{eq}}{\dot{\varepsilon}_{eq}}\left(\varphi\dot{\boldsymbol{\varepsilon}} + \left(\psi - \frac{1}{3}\varphi\right)tr(\dot{\boldsymbol{\varepsilon}})\boldsymbol{I}\right) \tag{21}$$

The evolution of porosity is linked to the volume change rate by the equation of mass conservation, eq.(22):

$$\frac{\dot{\theta}}{1-\theta} = \dot{\varepsilon}_x + \dot{\varepsilon}_y + \dot{\varepsilon}_z \tag{22}$$

Specifically for the form of pressure application in SPS (uniaxial pressure in the x direction), we have $\dot{\varepsilon}_y = \dot{\varepsilon}_z = 0$.

Thus, the continuity (eq.(22)) becomes:

$$\dot{\theta} = (1-\theta)(\dot{\varepsilon}_x) \tag{23}$$

According to Olevsky and Froyen (2006), the total compression rate $\dot{\varepsilon}_x$ is expressed by:

$$\dot{\varepsilon}_x = \frac{\delta_{\mathrm{gb}} D_{\mathrm{gb}}}{kT} \frac{\Omega}{(G+r_{\mathrm{p}})^2} \left\{ \frac{Z^* e_q}{\Omega} \frac{U}{l} + \frac{3\alpha}{G} \left[\frac{1}{r_{\mathrm{p}}} - \frac{1}{2G} \right] - \bar{\sigma}_x \frac{G+r_{\mathrm{p}}}{G^2} \right\} - \left\{ \left(\frac{3\theta}{2} \right)^{\frac{3}{2}} \left[\frac{3\alpha}{2G} (1-\theta)^2 - \bar{\sigma}_x \right] \Big/ A(1-\theta)^{\frac{5}{2}} \right\}^{\frac{1}{m}} \tag{24}$$

where A is the frequency factor of the power law, which satisfies the eq. (25):

$$A = A_0 \, exp\left(\frac{Q_{\mathrm{cr}}}{RT}\right) \tag{25}$$

and r_{p} is the radius of the pore that depends on the grain size and porosity.

$$r_p = G \sqrt[3]{\frac{\theta}{[6(1-\theta)]}} \tag{26}$$

Replacing eq. (25) and eq. (26) in eq. (24), the relationship to densification kinetics can be obtained:

$$\dot{\theta} = -(1-\theta) \left\{ \frac{\delta_{\mathrm{gb}} D_{\mathrm{gb}}}{kT} \frac{\Omega}{(G+G\sqrt[3]{\theta/\left[6(1-\theta)\right]})^2} \left\{ \frac{Z^* e_q}{\Omega} \frac{U}{l} + \frac{3\alpha}{G} \left[\frac{1}{G\sqrt[3]{\theta/\left[6(1-\theta)\right]}} - \frac{1}{2G} \right] - \bar{\sigma}_x \frac{G+G\sqrt[3]{\theta/\left[6(1-\theta)\right]}}{G^2} \right\} - \left\{ \left(\frac{3\theta}{2} \right)^{\frac{3}{2}} \left[\frac{3\alpha}{2G} (1-\theta)^2 - \bar{\sigma}_x \right] \Big/ A_0 \exp\left(\frac{Q_{cr}}{RT} \right) (1-\theta)^{\frac{5}{2}} \right\}^{\frac{1}{m}} \right\} \tag{27}$$

The terms of the eq. (27) and their respective numerical values for aluminum are presented in the Table 2.

Table 2 – Properties of aluminum

	Term	Value	Unit
Effective charge	Ze_{q}	8*e*-19	[C]
Atomic volume	Ω	1.66*e*-29	[m^3]
Surface tension	α	1.12	[J/m^2]
Activation energy for grain-boundary diffusion	Q_{gb}	60	[kJ/mol]
Grain boundary diffusion frequency factor	$\left[\delta_{\mathrm{gb}} D_{\mathrm{gb}}\right]_0$ $\left[\delta_{\mathrm{gb}} D_{\mathrm{gb}}\right]$	3.00*e*-14 $\left[\delta_{\mathrm{gb}} D_{\mathrm{gb}}\right]_0 \exp(-Q_{\mathrm{gb}}/RT)$	[m^3/s]
Activation energy for power-law creep	Q_{cr}	1.2*e*2	[kJ/mol]
Power-law creep frequency factor	A_0	566	[MPa/s^m]
Power-law creep exponent	m	2.27*e*-1	
Grain Size	G	40	[µm]
Applied field	U/l	500	[V/m]
External stress in the x-direction	$\bar{\sigma}_x$	23.5	[MPa]

Source: Olevsky and Froyen (2006)

Eq.(27) was resolved numerically by Olevsky e Froyen (2006) applying the Fourth Order Runge-Kutta method. The results obtained by them are presented in the Figure 14.

Figure 14 – Sintering kinetics

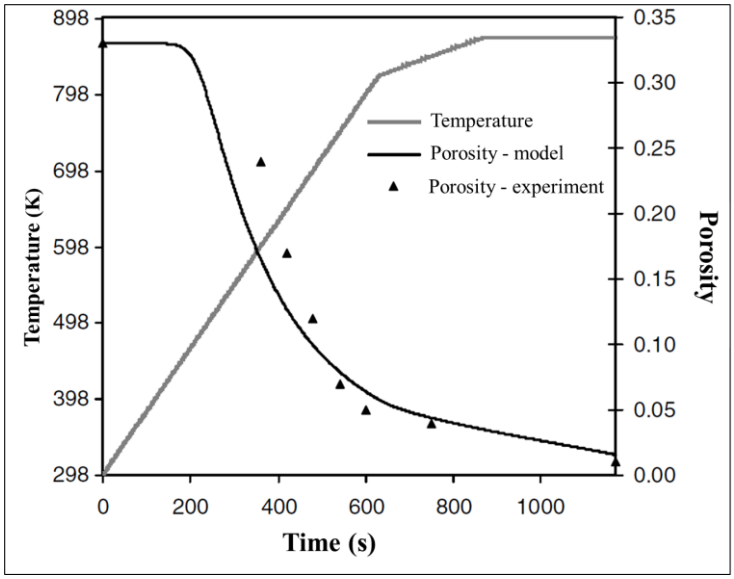

Source: Adapted from Olesky and Froyen (2006).

The results obtained by Olevsky and Froyen (2006) are satisfactorily close to the experimental data to which they referred, as can be seen in the Figure 14.

2.2.2.2 Abouaf constitutive model

In 1988, Abouaf extended the theory of plasticity to porous solids for hot deformation and within a more general thermodynamic structure, including finite deformations, for application in finite element sintering simulation using the hot isostatic pressing technique - HIP (ABOUAF *et al.*, 1988). This model can encompass the dominant phenomena in SPS sintering, such as: grain surface energy, electro-migration and charging effect. Researchers at the University of Toulouse, France, have developed simple methodologies based on the Abouaf model to identify creep parameters (MANIÈRE et al., 2016a, 2018; MARTINS et al., 2017).

As in the Olevsky model, the Abouaf model is based on the power-law creep for viscoplastic materials or Norton-Hoff's law, where the equivalent strain rate ($\dot{\varepsilon}_{eq}$) can be written as follows (eq. (28)):

$$\dot{\varepsilon}_{eq} = A\sigma_{eq}^{n} \tag{28}$$

where σ_{eq} and A are, respectively, the equivalent stress (eq.(29)) and frequency factor of the power-law creep (eq.(30)). These parameters are expressed by the following relationships:

$$\sigma_{eq} = \sqrt{3cJ_2 + fI_1^2} \tag{29}$$

$$A = A_0\, exp\left(-\frac{Q}{RT}\right) \tag{30}$$

In these equations, J_2 is the second principal invariant of the stress deviator tensor, $J_2 = \frac{1}{2}\boldsymbol{s}:\boldsymbol{s} = ||dev(\boldsymbol{\sigma})||$; I_1 is the first invariant of the Cauchy stress tensor, $I_1 = \sigma_{ii} = tr(\boldsymbol{\sigma})$; *c* and *f* are functions that depend on the relative density ρ. In addition, $A_0$the power-law creep frequency factor, *n* a constant, Q the power law creep activation energy, *R* gas constant and *T* absolute temperature (K).

The strain-rate tensor $\dot{\boldsymbol{\varepsilon}}$, according to the Norton-Green model, is expressed by eq. (31):

$$\dot{\boldsymbol{\varepsilon}} = A\sigma_{eq}^{n-1}\left(\frac{3}{2}c\boldsymbol{s} + fI_1\boldsymbol{I}\right) \tag{31}$$

Where $\boldsymbol{I}$ is the identity tensor.

Eq. (31) can also be written in the form of eq. (32):

$$\begin{bmatrix} \dot{\varepsilon}_x & \dot{\varepsilon}_{xy} & \dot{\varepsilon}_{xz} \\ \dot{\varepsilon}_{yx} & \dot{\varepsilon}_y & \dot{\varepsilon}_{yz} \\ \dot{\varepsilon}_{zx} & \dot{\varepsilon}_{zy} & \dot{\varepsilon}_z \end{bmatrix} = \frac{3}{2}A\sigma_{eq}^{n-1}c\begin{bmatrix} s_x & s_{xy} & s_{xz} \\ s_{yx} & s_y & s_{yz} \\ s_{zx} & s_{zy} & s_z \end{bmatrix} + A\sigma_{eq}^{n-1}fI_1\begin{bmatrix} 1 & 0 & 0 \\ 0 & 1 & 0 \\ 0 & 0 & 1 \end{bmatrix} \tag{32}$$

Being:

$$\left\| \begin{matrix} \dot{\varepsilon}_x = A\sigma_{eq}^{n-1}\left(\frac{3}{2}cs_x + fI_1\right) \\ \dot{\varepsilon}_{xy} = \dot{\varepsilon}_{yx} = A\sigma_{eq}^{n-1}\left(\frac{3}{2}cs_{xy}\right) \end{matrix} \right\| \quad \left\| \begin{matrix} \dot{\varepsilon}_{xz} = \dot{\varepsilon}_{zx} = A\sigma_{eq}^{n-1}\left(\frac{3}{2}cs_{xz}\right) \\ \dot{\varepsilon}_y = A\sigma_{eq}^{n-1}\left(\frac{3}{2}cs_y + fI_1\right) \end{matrix} \right\| \quad \left\| \begin{matrix} \dot{\varepsilon}_{yz} = \dot{\varepsilon}_{zy} = A\sigma_{eq}^{n-1}\left(\frac{3}{2}cs_{yz}\right) \\ \dot{\varepsilon}_z = A\sigma_{eq}^{n-1}\left(\frac{3}{2}cs_z + fI_1\right) \end{matrix} \right\| \tag{33}$$

In his thesis work, Manière (2015) uses these equations to build the mechanical model of SPS, in the present work these equations will be adapted to the Olevsky model, as will be explained below. The mass conservation equation (continuity) (eq. (34)) allows to assign the evolution of density according to the volume change rate, $tr(\underline{\dot{\varepsilon}})$.

$$\frac{\dot{\rho}}{\rho} = -tr(\underline{\dot{\varepsilon}}) = -\frac{3\dot{\varepsilon}_{eq}fI_1}{\sigma_{eq}} \tag{34}$$

In this model, the stress tensor $\boldsymbol{\sigma}$ is expressed by eq. (35).

$$\boldsymbol{\sigma} = \frac{\sigma_{eq}}{\dot{\varepsilon}_{eq}}\left(\frac{2}{3c}\dot{\boldsymbol{\varepsilon}} + \left(\frac{1}{9f} - \frac{2}{9c}\right)tr(\dot{\boldsymbol{\varepsilon}})\boldsymbol{I}\right) \tag{35}$$

In SPS, as the external loading is only in the axial direction, we can consider the stress tensor $\boldsymbol{\sigma}$ (eq. (36)) as:

$$\boldsymbol{\sigma} = \begin{pmatrix} 0 & 0 & 0 \\ 0 & 0 & 0 \\ 0 & 0 & \sigma_z \end{pmatrix} \tag{36}$$

We have $I_1 = \sigma_z$ and $J_2 = \frac{1}{3}\sigma_z^2$. Therefore, the equivalent stress σ_{eq} can be rewritten as follows (eq. (37)):

$$\sigma_{eq} = \sqrt{3c\frac{1}{3}\sigma_z^2 + f{\sigma_z}^2} = |\sigma_z|\sqrt{c+f} \tag{37}$$

To determine *c* and *f*, it is enough to know the experimental relationship between the strain rate as a function of the external stress applied and use the following system of equations (eq. (38)).

$$\begin{cases} c + f = \left(\dfrac{|\dot{\varepsilon}_z|}{A|\sigma_z|^n}\right)^{\frac{2}{n+1}} \\ \dfrac{4}{c} + \dfrac{1}{f} = \left(9A^{1/n}|\sigma_z||\dot{\varepsilon}_z|^{-1/n}\left(\dfrac{1}{3}\right)^{-\frac{1-n}{n}}\right)^{\frac{2n}{n+1}} \end{cases} \tag{38}$$

A and *n*, called Norton parameters, can be identified using compressive creep tests through the following linear regression (eq. (39)).

$$ln(\dot{\varepsilon}_{eq}) = ln(A) + n\,ln(\sigma_{eq}) \tag{39}$$

2.2.2.3 Identification of Creep Parameters by Olevsky model

To identify creep parameters using the Olevsky model, researchers from the University of Toulouse developed a simplified methodology using material densification curve data and linear regression (MANIÈRE *et al.*, 2016c, 2016b, 2018; MARTINS *et al.*, 2017).

When thermal kinetics is fast and applied pressure is high, the effective sintering stress, P_l, expressed by the eq. (16), can be ignored, because specifically in this case, creep is predominant. In this way, the eq. (24), strain rate, considering the pressure applied in the *z* direction and a constant heating rate, can be expressed by eq.(40):

$$\left|\dot{\varepsilon}_z\right|^{1/n} = \frac{-A^{1/n}\sigma_z}{\left(\psi + \frac{2}{3}\varphi\right)^{\frac{n+1}{2n}}\left(1-\theta\right)^{\frac{n-1}{2n}}}, \tag{40}$$

where: $A = \frac{\left(A_0 \exp\left(-\frac{Q}{RT}\right)\right)}{T}$ is the modified Arrhenius law.

Eq. (40) can be linearized by applying the natural logarithm on the left and right side, thus it becomes eq. (41).

$$n\ln\left(\frac{\left|\sigma_z\right|}{\left(\psi + \frac{2}{3}\varphi\right)^{\frac{n+1}{2n}}\left(1-\theta\right)^{\frac{n-1}{2n}}\left|\dot{\varepsilon}_z\right|^{1/n}}\right) - \ln(T) = -\ln(A_0) + \frac{Q}{RT}. \tag{41}$$

Except for constant *n*, which can be obtained qualitatively, as will be demonstrated below, all parameters on the left side of the eq. (41) can be obtained using the data provided by the SPS machine. From the sample compaction data, it is possible to obtain the porosity curve θ and strain rate $\dot{\varepsilon}_z$ depending on time, the other parameters, axial pressure σ_z and temperature *T*, are supplied directly by the SPS machine software.

Eq. (41) has the format: $Y = a + bX$, where: $X = 1/T$; θ is porosity; σ_z, the applied pressure; $\dot{\varepsilon}_z$, the strain rate; φ and $\psi$are porosity-dependent parameters, denominated, respectively, shear modulus and bulk modulus, expressed respectively by eq. (14) and eq. (15). To obtain A_0 and Q, the following relationships are used: $A_0 = exp(-a)$ and $Q = bR$.

In his article on the determination of sintering parameters of α-alumina, Manière et al. (2016b) obtained the densification curve of this material as a function of the time (Figure 15a) and applied this data to the eq. (41), assigning values to *n* between 1 and 3, with a step of 0.5, to get linear regression (Figure 15b), thus, a pair of parameters A_0 and Q was obtained for each *n*. The *n* is then qualitatively identified by the differential equation solution (eq. (49)).

$$\dot{\theta} = \left(1-\theta\right)\frac{\left(A_0/T\right)\exp\left(-\frac{Q}{RT}\right)\left|\sigma_z\right|^n}{\left(\psi + \frac{2}{3}\varphi\right)^{\frac{n+1}{2}}\left(1-\theta\right)^{\frac{n-1}{2}}}, \tag{42}$$

with the initial condition: $\theta(0) = \theta_0$ (initial porosity).

The data obtained by the model were compared with the experimental data (Figure 15c), thus, the *n* considered is that of the curve that best fits the experimental points. In this case, specifically, it is quite clear that the value of *n* that best suits the experimental data is equal to 1 (Figure 15(c)), thus, the *n* considered is that of the curve that best fits the experimental points. In this case, specifically, it is quite clear that the value of *n* that best suits the experimental data is equal to 1.

Figure 15 – Obtaining sintering parameters

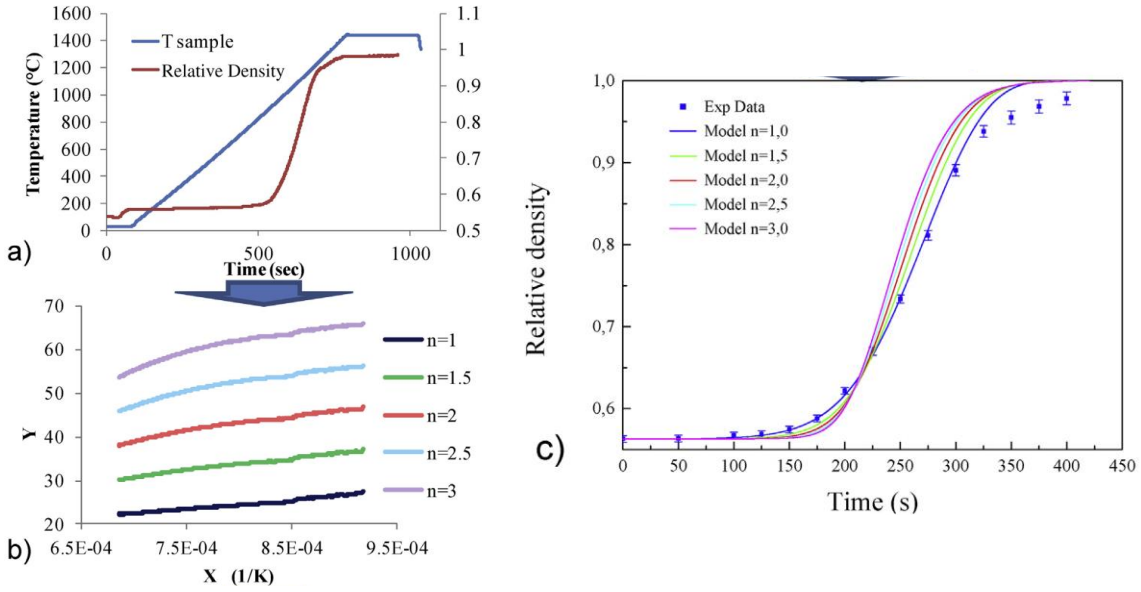

Source: Adapted from Manière et al (2016b).

2.2.2.4 Determination of parameter n quantitatively

For some materials, such as aluminum, the determination of *the n parameter* qualitatively is very complicated, due to this was developed the method of Li *et al.* (2012), which allows obtaining from the densification curve of the material. This method consists of a compaction test, which in this case is performed directly on the SPS machine, where the temperature is kept constant and the pressure is increased with fixed steps, where each step is maintained for a certain time and the compaction generated by each pressure level is measured, so the method is called *step-by-step*.

By the method of Li et al(2012), the *n* parameter is determined by the eq. (43)

$$n = \frac{ln\left(\frac{e^{-|\varepsilon_{z_2}|_{-(1-\theta_0)}|\dot{\varepsilon}_{z_1}|}}{e^{-|\varepsilon_{z_1}|_{-(1-\theta_0)}|\dot{\varepsilon}_{z_2}|}}\right)}{ln\left(\frac{\sigma_{z_1}}{\sigma_{z_2}} e^{|\varepsilon_{z_2}|-|\varepsilon_{z_1}|} \sqrt{\frac{e^{-|\varepsilon_{z_2}|_{-(1-\theta_0)}}}{e^{-|\varepsilon_{z_1}|_{-(1-\theta_0)}}}}\right)}, \tag{43}$$

where: θ_0, ε_{z_i}, $\dot{\varepsilon}_{z_i}$ e σ_{z_i} are, respectively, the initial porosity, strain, strain rate and the pressure applied (see diagram of the (Figure 16(a)).

The index *i* equal to 1 relates to step immediately preceding the pressure jump and the 2, the immediately subsequent step. As long as the mass is constant, the deformation (eq. (44)) and the strain rate (eq. (45)) are calculated according to the height of the sample.

$$|\varepsilon_z| = ln\frac{h_0}{h}, \tag{44}$$

$$|\dot{\varepsilon}_z| = \frac{d}{dt}\left[ln\frac{h_0}{h}\right], \tag{45}$$

Figure 16(b) presents the displacement and pressure curve as a function of the time obtained by Manière et al. (2018) for aluminum, this test was conducted performed at 250 °C.

Figure 16 – Compaction test for *n* determination

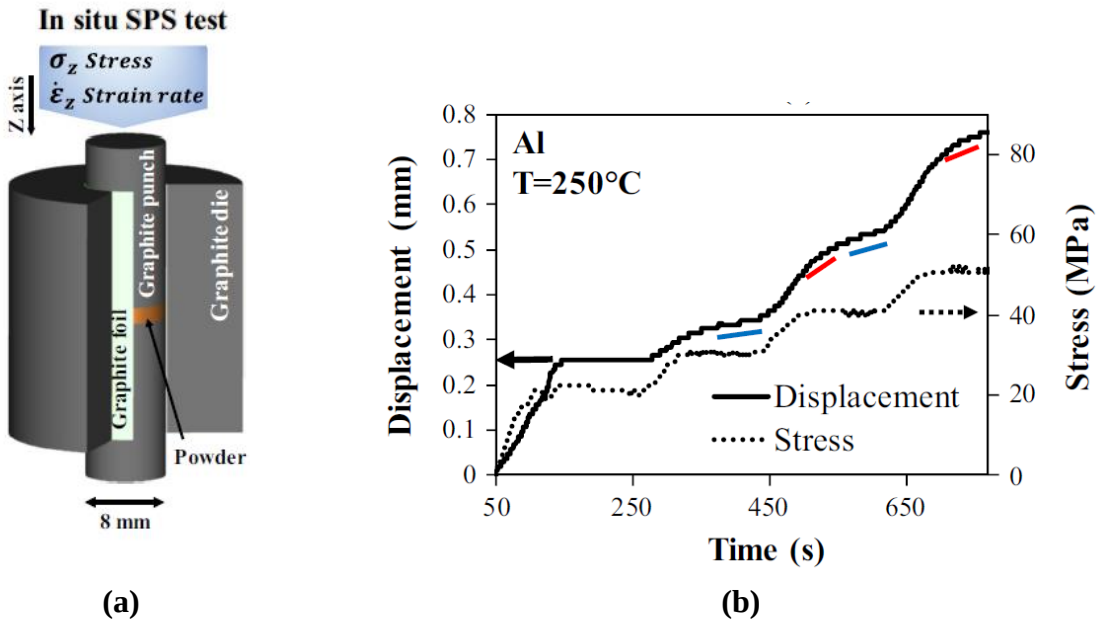

Source: Adapted from Manière et al (2018).

When the pressure jump occurs in a sufficiently short period of time, it can be considered that no significant change occurs in the microstructure in this interval. In this case, specifically, the eq. (43) can be reduced to eq. (46).

$$n = \frac{ln\left(\frac{|\dot{\varepsilon}_{z1}|}{|\dot{\varepsilon}_{z2}|}\right)}{ln\left(\frac{\sigma_{z1}}{\sigma_{z2}}\right)}, \tag{46}$$

which is the standard formula for determining exponent *n* of the creep-law from creep test data (LI *et al.*, 2012).

Manière *et al.* (MANIÈRE *et al.*, 2018) used this methodology to determine the creep parameters of aluminum (from the data of the Figure 16(b) quantitatively and compared with the values obtained qualitatively, using the concepts developed by Olevsky. By method *step-by-step* (LI *et al.*, 2012), was obtained *n* equal to 5.4 ± 0.9. By the qualitative method (Olevsky), an *n* is obtained between 4 and 5, this shows that the Li *et al.* method combined with the Olevsky method is a good option for determining the value of *n*.

2.2.2.5 Electro-Thermo-Mechanical Boundary Conditions

To perform a computational simulation of SPS that allows predicting some important information of the sintered part, such as final density, grain size and porosity, it is essential that mechanical boundary conditions are applied correctly. Therefore, mechanical boundary conditions are added to the electrothermal boundary conditions (as described in the subsection 2.2.1).

As seen previously, some parameters depend on the porosity of the material. In the Olevsky and Abouaf model, the porosity of the material is obtained by the use of differential equations. To solve these equations numerically, COMSOL Multiphysics has the module "Domain ODEs and DAEs". This module can also be used if the evolution of grain size is taken into account.

Figure 17 presents in a schematic way the electro-thermomechanical boundary conditions. In this case, it is worth noting that the mechanical analysis only needs to be done in the sample domain. The stresses generated in the sample and its contraction are controlled by the module of differential equations.

Figure 17 – Electro-thermo-mechanical boundary conditions

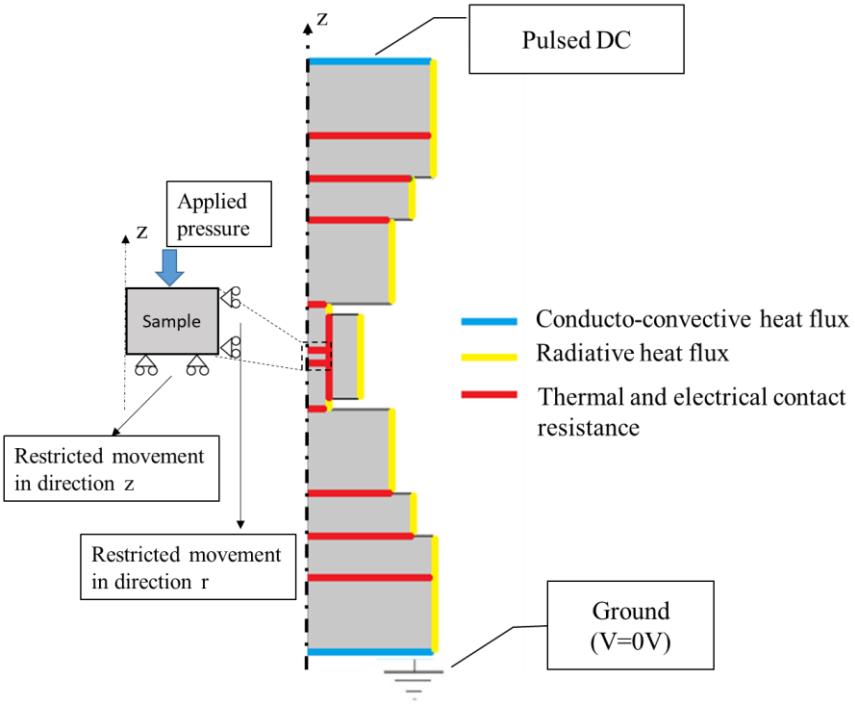

Source: The Author (2022)

As mentioned earlier, the local equilibrium equations of the Abouaf model used by Manière in his thesis to model the mechanical part of the SPS can be adapted to the Olevsky model, as they are equivalent models. Comparing the eq. (35) and eq. (21), we can observe that the parameters of Abouaf c and f can be written according to the parameters of Olevsky φ and ψ, respectively as:

$$\begin{cases} c = \dfrac{2}{3\varphi}, \\ f = \dfrac{1}{9\psi}, \end{cases} \tag{47}$$

In this way, the eq. (32) can be rewritten depending on the parameters φ and ψ, taking the form of the eq. (48).

$$\begin{bmatrix} \dot{\varepsilon}_x & \dot{\varepsilon}_{xy} & \dot{\varepsilon}_{xz} \\ \dot{\varepsilon}_{yx} & \dot{\varepsilon}_y & \dot{\varepsilon}_{yz} \\ \dot{\varepsilon}_{zx} & \dot{\varepsilon}_{zy} & \dot{\varepsilon}_z \end{bmatrix} = \frac{A\sigma_{eq}^{n-1}}{\varphi} \begin{bmatrix} s_x & s_{xy} & s_{xz} \\ s_{yx} & s_y & s_{yz} \\ s_{zx} & s_{zy} & s_z \end{bmatrix} + \frac{A\sigma_{eq}^{n-1} I_1}{9\psi} \begin{bmatrix} 1 & 0 & 0 \\ 0 & 1 & 0 \\ 0 & 0 & 1 \end{bmatrix} \tag{48}$$

Where:

$$\left\| \begin{matrix} \dot{\varepsilon}_x = A\sigma_{eq}^{n-1}\left(\frac{s_x}{\varphi}+\frac{I_1}{9\psi}\right) \\ \dot{\varepsilon}_{xy}=\dot{\varepsilon}_{yx}=A\sigma_{eq}^{n-1}\left(\frac{s_{xy}}{\varphi}\right) \end{matrix} \right\| \quad \left\| \begin{matrix} \dot{\varepsilon}_{xz}=\dot{\varepsilon}_{zx}=A\sigma_{eq}^{n-1}\left(\frac{s_{xz}}{\varphi}\right) \\ \dot{\varepsilon}_y = A\sigma_{eq}^{n-1}\left(\frac{s_y}{\varphi}+\frac{I_1}{9\psi}\right) \end{matrix} \right\| \quad \left\| \begin{matrix} \dot{\varepsilon}_{yz}=\dot{\varepsilon}_{zy}=A\sigma_{eq}^{n-1}\left(\frac{s_{yz}}{\varphi}\right) \\ \dot{\varepsilon}_z = A\sigma_{eq}^{n-1}\left(\frac{s_z}{\varphi}+\frac{I_1}{9\psi}\right) \end{matrix} \right\| \tag{49}$$

Thus, it is possible to apply the Olevsky model to finite element modeling in COMSOL Multiphysics, using local equilibrium eq. (49).

2.3 STEELMAKING WASTE: ELECTRIC ARC FURNACE DUST (EAFD)

One waste from the semi-integrated plants that generates great concern is the electric arc furnace dust (EAFD). This waste consists of metal oxides, lime and silica, and has been classified as dangerous due to the content of heavy metals such as zinc, cobalt, copper, lead or cadmium by the Brazilian Association of Technical Standards (ABNT 10004, 2004), the Environmental Protection Agency (EPA) in the United States of America (BAKKAR, 2014) and the European Waste Catalog (EPA, 2002). It represents one of the biggest problems of the electrical steel plant and cannot be disposed of in common landfills.

EAFD is generated during the melting of ferrous scrap in an electric arc furnace (EAF) and collected by large bag filters. The EAF, designed to manufacture steel from recycled ferrous scrap, as the main filler material, mixed with pig iron and/or direct-reduced iron, co-produces between 15 to 25 kg of EAFD per ton of steel (ARAÚJO; SCHALCH, 2014; GUÉZENNEC *et al.*, 2005).

The EAFD residue stabilization and solidification processes are simple and efficient. Some studies on this approach (using EAFD in the manufacture of ceramic blocks of clay, cement, concrete, etc.) have been conducted and have shown that, after this process, the resulting materials are in accordance with environmental standards and, in some cases, had some improved properties (HUAIWEI; XIN, 2011; LEDESMA *et al.*, 2017; SOUZA *et al.*, 2010; STATHOPOULOS *et al.*, 2013a).

In varying weight percentages, Gamea et al. (2022) added EAFD as a filler to unsaturated polyester (UP) resin. The outcome shown that adding EAFD particles to the UP matrix considerably changed the mechanical characteristics by raising the tensile strength by up to 42%. The UP/EAFD composites become harder up to 8.5% and reach their hardest point at 10 weight percent EAFD (GAMEA *et al.*, 2022).

The incorporation of EAFD in metal matrix composites has also proved to be a good alternative for recycling this waste. Adeosun et al (2012) studied the influence of the addition of EAFD on the mechanical properties of 6063 aluminum alloy, using the sand casting technique for the production of composites. Flores-Vélez et al (2001) used conventional powder metallurgy techniques to produce EAFD reinforced aluminum alloy composites. In both studies, it was demonstrated that the presence of EAFD as reinforcement in certain amounts shows gains in mechanical strength and microhardness in relation to the aluminum alloys used.

Alves et al (2018) investigated the influence of EAFD as reinforcement in AA7075 aluminum matrix composites by applying 5 wt. % reinforcement and comparing with AA7075 alloy as received. The composites were prepared by powder metallurgy (PM) technique, compacted with a pressure of 1500 MPa and sintered at a temperature of 500 °C for 5 hours in nitrogen atmosphere. In that work, the Vickers microhardness (HV) of the 5 wt.% EAFD-AA7075 composite was 46.4% higher than that of the unreinforced AA7075 alloy. The Young's modulus (E), in GPa, increased by about 98.5%. There was also an increase in the stored modulus (GPa) due to the reinforcement, as presented in the following Figure 18 (OLIVEIRA ALVES *et al.*, 2018).

Figure 18 – Storage modulus vs. temperature from DMA.

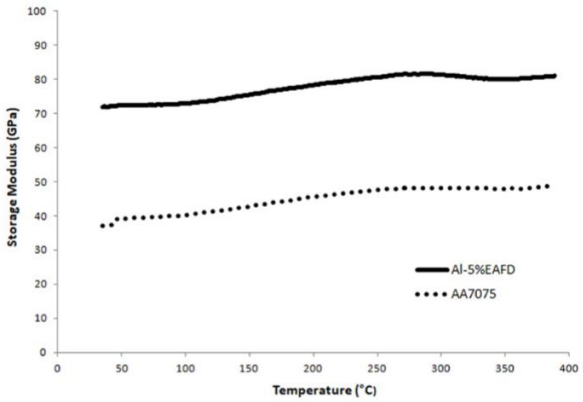

Source: Oliveira Alves et al. (2018).

2.4 AA7075 ALUMINUM ALLOY

The aluminum alloy AA7075 is widely used in the aeronautical (JHA; SREEKUMAR, 2008), maritime, automotive and defense industries due to its high ratio between mechanical strength and weight (JHA; SREEKUMAR, 2008; KUMAR; REDDY;

RAO, 2015). However, it is still the subject of several studies seeking to further improve its mechanical properties (AYE *et al.*, 2008; ISADARE *et al.*, 2012; VEERAVALLI *et al.*, 2016).

More recently, several research studies performed on AA7075 have focused on the evaluation of heat treatments on their mechanical properties, looking for a relationship between the formation of stable phases, mainly of the $MgZn_2$ phase, with the precipitation hardening of this material. These studies have shown that heat treatments have a strong impact on mechanical properties. However, the treatment time is long, taking up to more than 1 day, in the case of T6 treatment, which motivates the search for more efficient manufacturing methods (ESTRADA-RUIZ *et al.*, 2016; HUANG *et al.*, 1994; ISADARE *et al.*, 2012; MOLNÁROVÁ *et al.*, 2018; ZHANG *et al.*, 2019).

2.5 CRYSTALLITE SIZE AND MICRO-STRAIN DETERMINATION

In this section, Williamson–Hall (W–H) method for crystallite size and micro-strain determination will be described by X-Ray Difraction – XRD (WILLIAMSON; HALL, 1953). The XRD peak measured broadening normally consists of two parts, which are the physical and instrumental broadening. The corrected physical broadening (β) can be obtained using eq.(50):

$$\beta^2 = \beta_m^2 - \beta_i^2, \tag{50}$$

where β_m is the experimental full width at half maximum (FWHM) and β_i is the instrumental broadening obtained by Caglioti equation (CAGLIOTI; PAOLETTI; RICCI, 1958).

After subtracting the instrumental broadening, the corrected physical broadening (β) can be considered as the sum of widths due to small crystallite sizes (β_D) and lattice strains (β_ε)(SURYANARAYANA; NORTON, 1998) as shown by eq. (51):

$$\beta = \beta_D + \beta_\varepsilon, \tag{51}$$

The peak broadening due to the crystallite size β_D is expressed by eq. (52) (WILLIAMSON; HALL, 1953):

$$\beta_D = \frac{K\lambda}{D\cos\theta}, \quad (52)$$

where, K is a constant (K = 0.94 for small cubic crystal (MISHRA *et al.*, 2015)), λ is the wavelength of the X-rays used, D is the crystallite size and θ is the Bragg angle.

Similarly, the peak width due to lattice strain β_ε (eq.(53)) is:

$$\beta_\varepsilon = 4\varepsilon \tan\theta, \quad (53)$$

From eq. (52) and eq. (53), we get

$$\beta = \frac{K\lambda}{D\cos\theta} + 4\varepsilon \tan\theta, \quad (54)$$

or,

$$\beta\cos\theta = \varepsilon(4\sin\theta) + \frac{K\lambda}{D}, \quad (55)$$

Eq. (55), above, is an equation of a straight line of the type $y = ax + b$, where the slope a provides the value of the intrinsic strain ε and the intercept b gives the average particle size D, so $\varepsilon = a$ and $D = \frac{K\lambda}{b}$.

The micro-strain ε and the crystallite size D obtained by XRD analyses were used to calculate the dislocation density δ, expressed by the eq. (56) (BERA *et al.*, 2013).

$$\delta = \frac{2\sqrt{3}\langle\varepsilon^2\rangle^{\frac{1}{2}}}{(D\times b)}, \quad (56)$$

where δ is the dislocation density and b is the magnitude of the Burgers vector equal to $a_0/\sqrt{2}$ for an FCC Al alloy.

3 MATERIALS AND METHODS

This chapter describes the procedures adopted for the characterization of the starting powders: AA7075 and Electric Arc Furnace Dust (EAFD). The methodology to prepare the mixtures to produce composites of aluminum alloy matrix AA7075 reinforced with EAFD is presented. In addition, the procedures for the consolidation of samples by the Spark Plasma Sintering (SPS) technique, characterization of composites and finite element simulation of the SPS process are described. Figure 19 shows a flowchart of the general methodology used.

Figure 19 – Flowchart of the general methodology used.

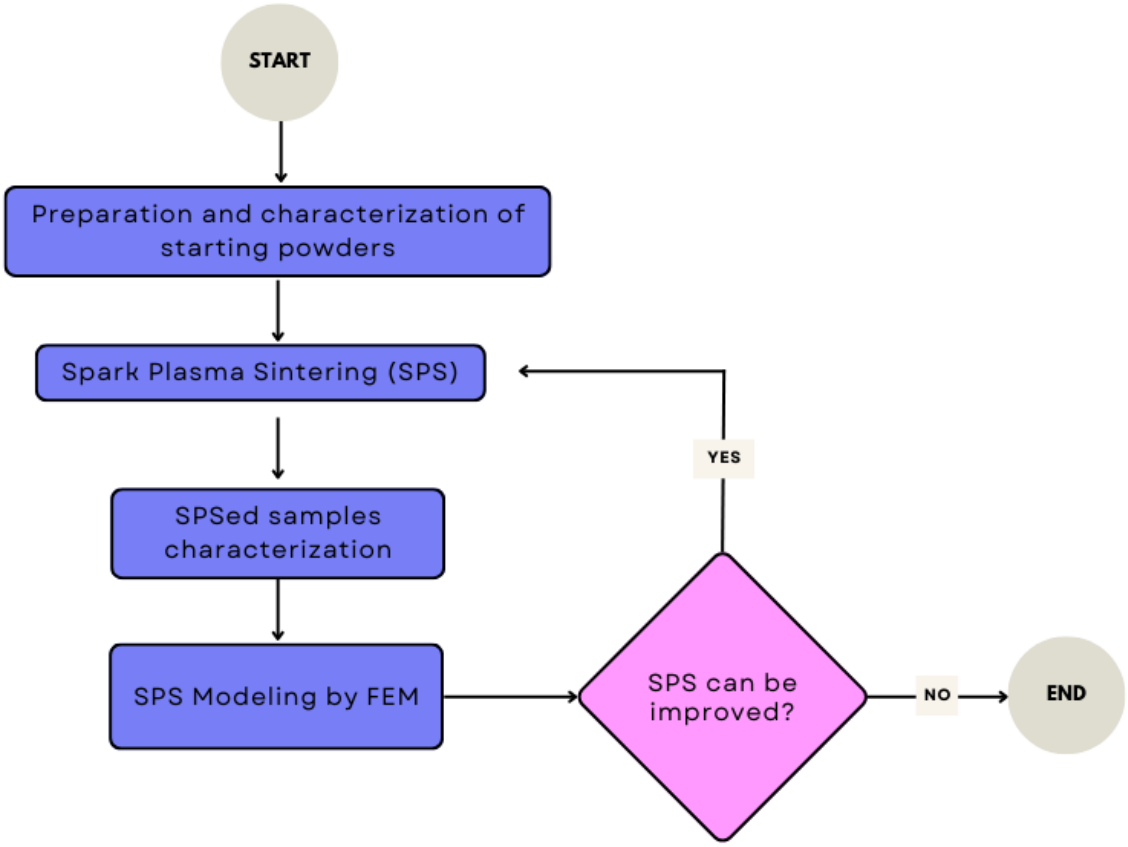

Source: The Author (2022)

3.1 7075 ALUMINUM ALLOY (AA7075)

The AA7075 powder produced by ALCOA (ALCOA, Brazil) was selected as matrix for the composite production. This powder has an average particle size of 30 μm. The powder was used both as-received and after ball-milling in a high-energy mill (SPEX), consisting in a 304 L stainless steel jar and SAE 52100 steel balls approximately 6.2 mm in diameter. The

powder was ball-milled in isopropyl alcohol for 1 h with 2 wt.% stearic acid ($CH_3(CH_2)_{16}COOH$). Milling was performed with a ball to powder weight ratio of 10:1 (GÖKÇE; FINDIK; KURT, 2011; OLIVEIRA ALVES *et al.*, 2018). The raw and ball-milled powders will be referred to hereafter as AA7075 and AA7075-M, respectively.

3.2 ELECTRIC ARC FURNACE DUST (EAFD)

The EAFD in its original form, supplied by the GERDAU Aço Norte plant located in the city of Recife, State of Pernambuco, Brazil, was selected as reinforcing material. This material was separated by sieving, with the sequence of sieves 65, 150, 200 and 270 mesh. The part of the powder that is used in the present study correspond to the two smaller size ranges, which are: grains that passed through the sieve of 200 mesh (particles in the range of 53-75 μm) and through the 270 mesh (particles smaller than 53 μm).

The procedures for characterizing this material are described in subsection 3.5.

3.3 PREPARATION OF STARTING POWDERS

The technique of high-energy milling in a vibratory mill type SPEX was applied in the production of starting powders.

Firstly, EAFD powders were sieved and two samples have been selected for the study: one with the particle size lower than 53 μm (noted as G1 hereafter) and the other with the particle size between 53 μm and 75 μm (noted as G2 hereafter).

Then, the G1 and G2 powders were ball-milled in liquid medium (isopropyl alcohol) for 1 h with the AA7075 powder (the pure AA7075 sample was also ball-milled in the same conditions, for the sake of comparison), and 2 wt.% stearic acid ($C_{18}H_{36}O_2$) of the total weight of the sample. The composite powders were prepared with 5, 10 and 15 wt.% EAFD with either G1 or G2 (representing 3.8, 7.7, 11.7 vol.% and 4.2, 8.4, 12.7 vol.% for G1 and G2, respectively, see part 4.2 for further details). Milling was performed with a ball to powder ratio of 10:1.

The nomenclature of the starting powders according to their contents are presented in Table 3. To indicate the sintered samples, an "S" was added to the end of the name of the corresponding starting powder.

Table 3 – Nomenclature of the starting powders according to their compositions.

	Content (wt.%)		
Sample	**G1**	**G2**	**AA7075**
AA7075 (as received)	-	-	100
AA7075-M (milled)	-	-	100
05G1	5	-	95
10G1	10	-	90
15G1	15	-	85
05G2	-	5	95
10G2	-	10	90
15G2	-	15	85

Source: The Author (2022)

3.4 SPARK PLASMA SINTERING (SPS)

The powders were consolidated by Spark Plasma Sintering – SPS (Dr Sinter SPS 632Lx, Fuji Electronic Industrial CO., Saitama, Japan) at the Plateforme Nationale CNRS de Frittage Flash (Toulouse, France). The EAFD-AA7075 powders were loaded into a graphite die. A sheet of graphitic paper was placed between the punch and the powder and between the die and the powder for easy removal. Figure 20 (a) shows the front view of the SPS machine used in this work, on the left of this image the vacuum chamber can be seen and on the right side the process control system. Figure 20 (b) shows the internal view of the chamber, where the SPS column is located, composed of the Inconel 600 electrodes, graphite tools, and the sample to be sintered.

Figure 20 – SPS Machine Used in This Work: (a) overview; (b) graphite tools.

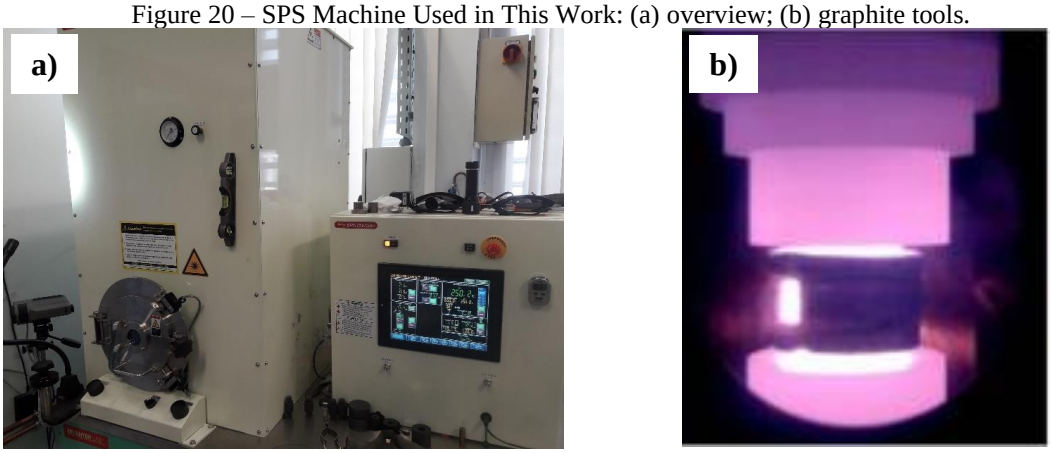

Source: The Author (2022)

The SPS run was performed in vacuum (residual cell pressure < 10 Pa) using a direct current pulse pattern of 40 ms: 7 ms (pulse on: pulse off). The temperature was controlled

using K-thermocouple inserted into a hole (3 mm deep) drilled on the outer surface of the die. The samples were heated with a heating rate of 100 °C/min to a temperature T_d (400, 500 or 550 °C) where a dwell time of t_d (0, 5, 15 or 30 min) was applied. A uniaxial charge P (corresponding to 25, 50 or 100 MPa in the compact) was applied at room temperature and maintained during the heating and dwell steps. Natural cooling was applied down to room temperature and the uniaxial load was gradually released at the same time. The Figure 21 represents one of the cycles used, with the following parameters: T_d = 550ºC, t_d = 15 min and P = 100 MPa.

Figure 21 – SPS cycle. The blue line represents the temperature cycle, while the orange line represents the pressure cycle.

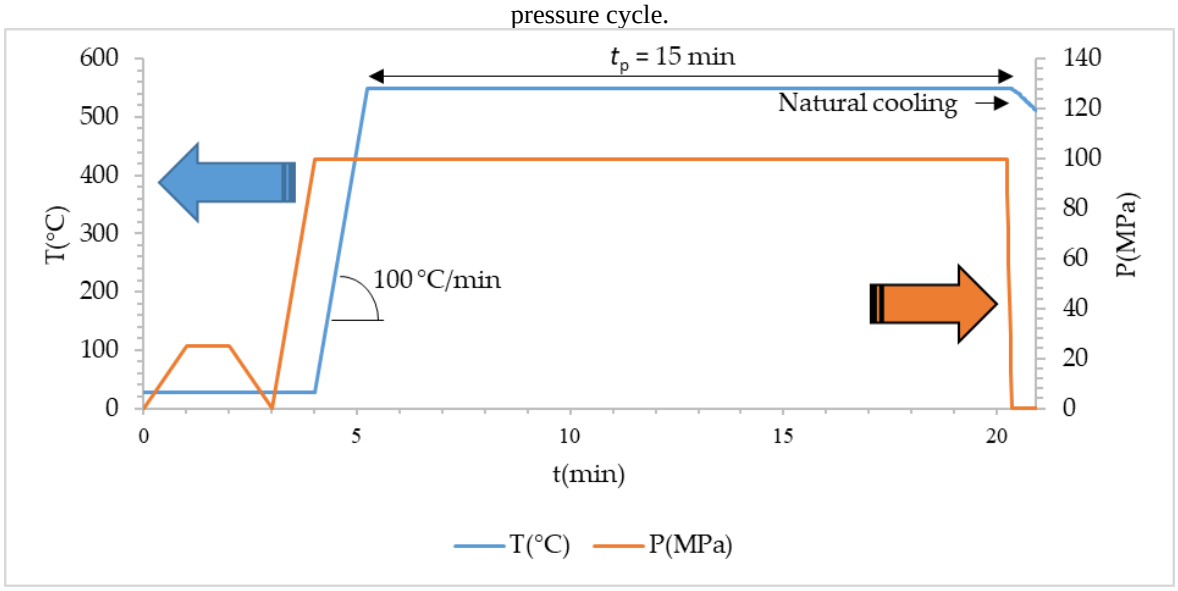

Source: The Author (2022)

SPS pellets were 8 or 20 mm in diameter and 3 mm thick. The graphitic paper remaining on the surface was removed by machining.

3.5 CHARACTERIZATION

The particle size analysis of EAFD powder (G1 and G2) was performed in liquid dispersing medium by laser diffraction (Malvern Instruments Mastersize 2000). The density of the powders and sintered samples was evaluated by He pycnometry (Micromeritics AccuPyc II 1340) and Archimedes'method (Sartorius YDK01), respectively. The chemical composition of powders (G1 and G2) was determined by X-ray fluorescence (XRF) spectrometry (Rigaku ZSX Primus II), at room temperature.Figure 22 shows the sequence of analyses performed on the powders.

Figure 22 – Powders characterization

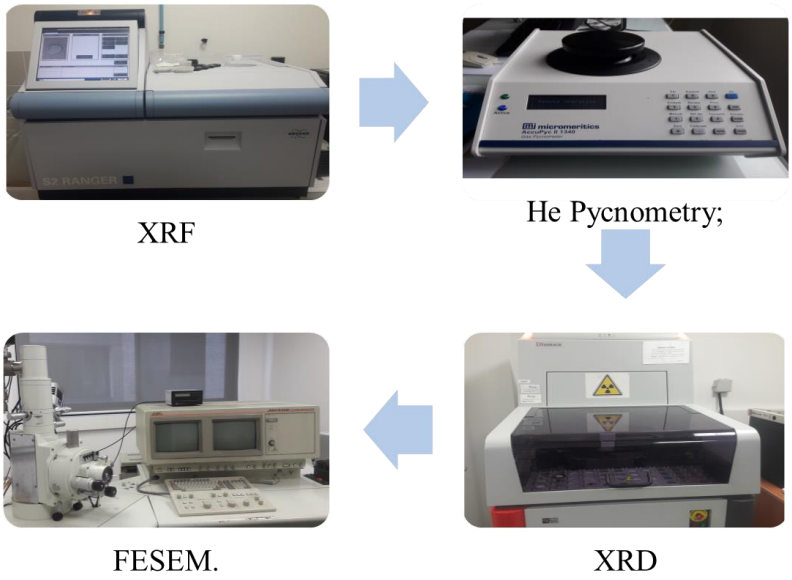

Source: The Author (2022)

The crystalline phases in the powders and sintered samples were detected and identified using X-ray diffraction (XRD, Bruker D4 (Cu K_α) in θ–2θ configuration), in the range of $10° < 2\theta < 100°$ with a step size of 0.02°, using $CuK_{\alpha 1}$ radiation (0.15406 nm), having the accelerating voltage of 40 kV. The crystallite size and the micro-strain have been estimated from the XRD patterns using the Williamson–Hall (W–H) method (WILLIAMSON; HALL, 1953). Figure 23 presents the sequence of analyses performed on the sintered samples.

Figure 23 – Characterization of the sintered samples

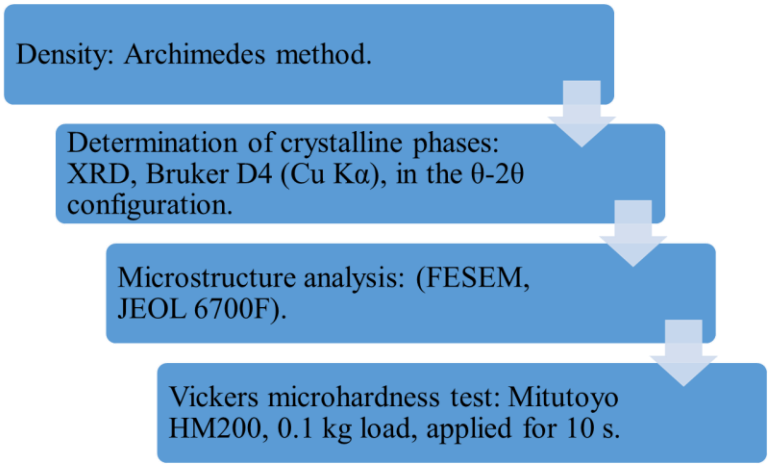

Source: The Author (2022)

In order to perform optical microscopy and scanning electron microscopy (SEM) to reveal the microstructure of the sintered samples, it is necessary to prepare the surface of the

samples by polishing and then performing a suitable chemical etching to reveal the grain boundary regions. The sintered samples were prepared for microstructural analyses using the following protocol (Figure 24). The graphitic paper remaining on the surface was removed by machining. Initially, in the water-based gridding of the SPSed samples, AA7075 and AA7075-EAFD composites, 1200 and 2400 SiC discs were used sequentially, for approximately 1 min each. Afterwards, to perform the polishing, FD1N-type black felt disks were used for 3 min each, with the following sequence: diamond suspension of 6μm, 3μm, and 1μm; amorphous silica suspension of 20 nm (CERRI; EVANGELISTA, 1999). At the end, the samples were cleaned with acetone (C_3H_6O) and dried with nitrogen, in order not to create new grooves and to avoid oxidation or other chemical reactions on the surface.

Figure 24 – Sample polishing protocol

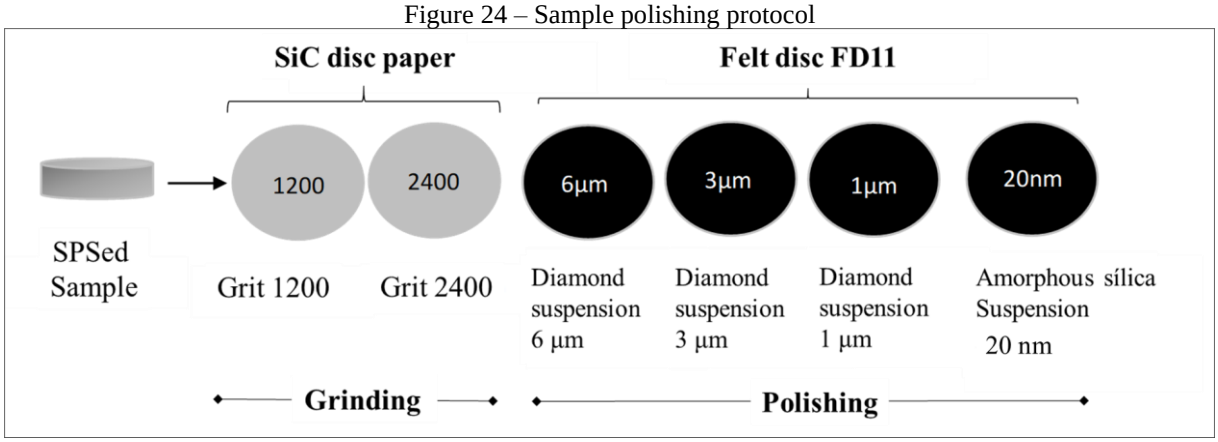

Source: The Author (2022)

To check the microstructure of the sample in order to assess information about grain size range, porosity and distribution of the phases present, it is necessary to proceed to the chemical attack of the surfaces. In this case a 10g NaOH + 100 ml H_2O solution was used (ZIPPERIAN, 2011) and the following immersion times were tested: 10s, 20s, 30s, 40s, 50s, 1min, 2min, and 5 min. To stop the attack, the samples were immersed in ethanol (EtOH) for 20s and then immersed in distilled water for 1 min under ultrasound cleaning. At the end, the samples were dried with nitrogen gas. The determination of the best etching time was carried out on 8 mm specimens that were sintered at heating rate 100°C/min, step temperature 500 °C, for 15 min, and subjected to axial pressure of 50 MPa.

After etching, optical microscopy was performed on the samples, using a Keyence VHX-1000 3D Optical Microscope, with magnification from x20 to x5000. The average grain size was estimated from the image by the ratio of the length of 4 randomly drawn lines to the

amount of grain outlines that intersect them. The samples were also observed using field-effect-gun scanning electron microscopy (FESEM, JEOL 6700F).

Vickers microhardness test was performed with a Mitutoyo Hardness Tester HM200 from CIRIMAT (Université de Toulouse, France). The samples before being submitted to this test were polished, in the same way as previously described for the metallography. The load applied during the test was 0.1 kg for 10s. Vickers microhardness (HV) averages were obtained from 10 identifications applied along the radius of the samples.

3.6 MODELLING BY THE FINITE ELEMENT METHOD

The sequence used for finite element modeling is shown in the Figure 25. The steps represented in the boxes in green are steps prior to modeling related to obtaining data from experimental results, in blue are the actual steps.

Figure 25 – Steps used to perform the modeling.

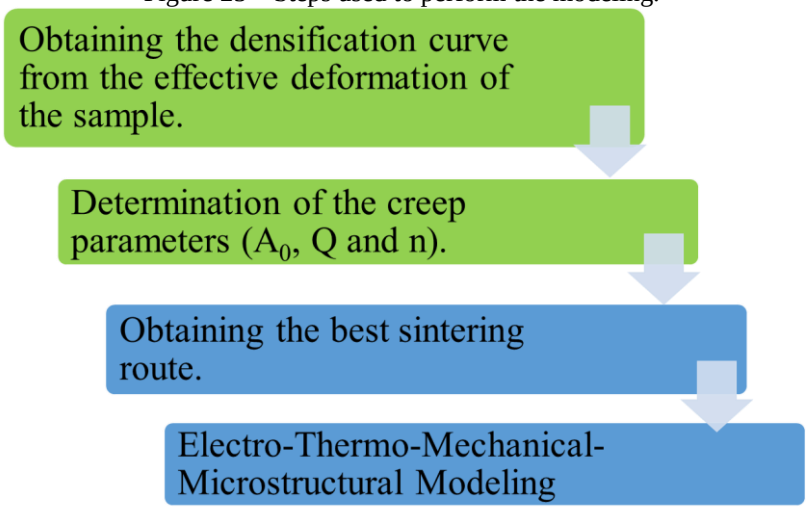

Source: The Author (2022)

3.6.1 Determining the creep parameters

For modeling the SPS by the finite element method, the first step is to obtain the densification curve of the AA7075 sample. For the modeling, the milled AA7075 sample (AA7075-M) was used, as it was the basis used for the fabrication of the EAFD /AA7075 composites.

The densification curve is calculated by the sample shrinkage that is provided by the SPS machine. To obtain the effective sample shrinkage Δh, it is necessary to subtract from the

total displacement Δh_t the punch displacement caused by the thermal expansion of the tools and the deformation generated by the applied pressure Δh_b, which is obtained from a cycle using the fully dense sample. Thus, the effective shrinkage of the specimen Δh can be expressed by $\Delta h = \Delta h_d - \Delta h_b$.

If mass is conserved, density can be obtained by eq. (57).

$$\rho = \frac{\rho_0 h_0}{h} = \rho_0 \frac{1}{1 - \frac{\Delta h}{h_0}} \tag{57}$$

Where: ρ_0 is the initial relative density, h_0 the initial height, h the height, Δh the change in height.

The following is how the values of Q, A_0 and n for the AA7075 were qualitatively obtained using Olevsky's method.

Obtaining the parameters can be done in a simple way, using the data from the SPS test. As reported above, by shrinking the sample it is possible to obtain the densification curve as a function of time, which allows to obtain the strain rate, all other parameters are provided by the SPS machine software. Making n vary discretely from 1 to 5, the parameters A_0 and Q are determined by the following linearized eq. (58).

$$n \ln\left(\frac{|\sigma_z|}{\left(\psi + \frac{2}{3}\varphi\right)^{\frac{n+1}{2n}} (1-\theta)^{\frac{n-1}{2n}} |\dot{\varepsilon}_z|^{1/n}} \right) - \ln(T) = -\ln(A_0) + \frac{Q}{RT} \tag{58}$$

which has the form: $y = a + bx$, where: $x = 1/T$; θ is the porosity; , σ_z is the applied stress, $\dot{\varepsilon}_z$ is the strain rate; φ and ψ are porosity-dependent parameters called, respectively, shear modulus (eq. (59)) and bulk modulus (eq. (60)), expressed by:

$$\varphi = (1-\theta)^2 \tag{59}$$

$$\psi = \frac{2}{3}\frac{(1-\theta)^3}{\theta} \tag{60}$$

To obtain A_0 and Q, the following relations are used: $A_0 = exp(-a)$ and $Q = bR$.

After determining the parameters, it is possible to solve the differential equation of the porosity, for each *n*, varying from 1 to 5, and compare it with the experimental result, to verify which set of values gives the modeling curve that is closest to the experiment.

$$\dot{\theta} = (1-\theta)\frac{(A_0/T)\exp\left(-\frac{Q}{RT}\right)|\sigma_z|^n}{\left(\psi+\frac{2}{3}\varphi\right)^{\frac{n+1}{2}}(1-\theta)^{\frac{n-1}{2}}} \quad (61)$$

For some materials, such as aluminum, the determination of *the n parameter* qualitatively is very complicated. The Li method (LI *et al.*, 2012) was used to help obtain *n* in a quantitative way, since it is not always possible to obtain *n* by the method developed by Manière.

3.6.2 Validation of the creep parameters

In order to validate the creep parameters obtained in the previous step, a numerical model representing a 8 mm diameter sample fabricated with the same SPS parameters used to assess the creep parameters was simulated, i.e.: pressure of 50 MPa, temperature = 500º C and dwell time = 15 min. Numerical results obtained were then compared with the experimental ones in order to validate the creep parameters used in this work.

3.6.2.1 Geometry

Due to the cylindrical symmetry of the SPS tools, 2D-aximetric modeling was performed as represented in the Figure 26. The dimensions of the main parts of the configurations used for sintering the 8 mm or 20 mm diameter samples, respectively named Φ8 and Φ20, are shown in Table 4.

Figure 26 – Geometries used in the FEM modeling: (a) Φ8; (b) Φ20.

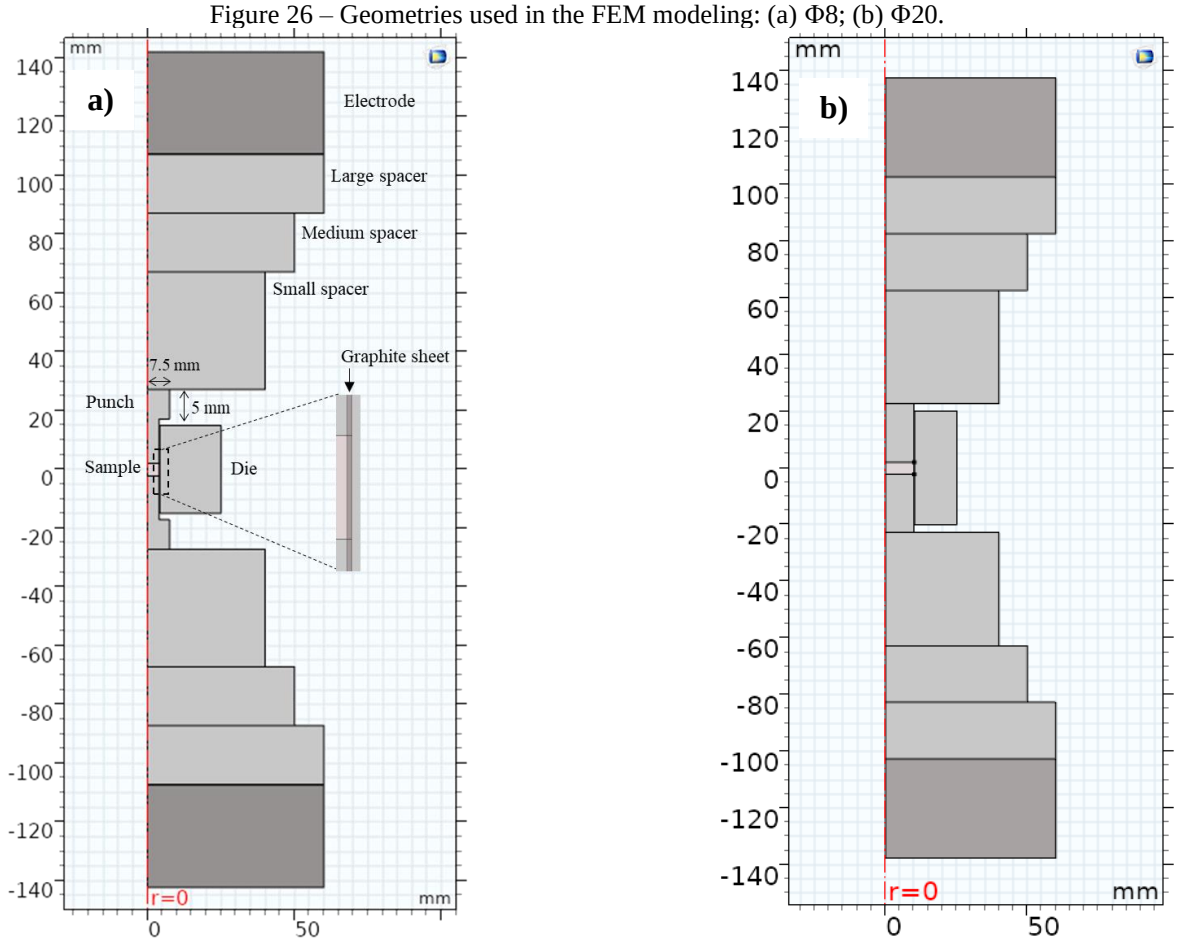

Source: The Author (2022)

Table 4 – SPS Setup Main Dimensions

	Φ 8	Φ 20	Material		Φ 8	Φ 20	Material
Punch				**Large Spacer**			
Height	22.55	20.55		Height	20	20	Graphite
Radius	4	10		Radius	60	60	
Die							
Height	30	40		**Electrode**			
Radius	25	25	Graphite	Height	35	35	Inconel 600
Small Spacer				Radius	60	60	
Height	40	40					
Radius	40	40		**Sample**			
Medium Spacer				Height	4.3	5	AA7075
Height	20	20		Radius	4	10	
Radius	50	50					

Source: The Author (2022)

3.6.2.2 Material

The properties of the materials used in the finite element modeling are shown in Table 5. The properties of graphite and Inconel 600 are already well known in the SPS literature (MANIÈRE *et al.*, 2018; MANIÈRE; TORRESANI; OLEVSKY, 2019; VAN DER LAAN *et al.*, 2021). For the aluminum alloy AA7075, the data for electrical conductivity, thermal conductivity and heat capacity at constant pressure were obtained from the work published by He *et al.* (HE *et al.*, 2019). All these parameters are temperature dependent, as presented in the Figure 27. The dependence of these properties on the porosity θ is also taken into account (OLEVSKY *et al.*, 2012).

Table 5 – Material properties

	Graphite (VAN DER LAAN *et al.*, 2021)	**Inconel 600** (VAN DER LAAN *et al.*, 2021)	**AA7075** (HE *et al.*, 2019; OLEVSKY *et al.*, 2012)
Electrical conductivity, σ_e (S/m)	$(1.7\cdot10^{-5}-1.87\cdot10^{-8}T+ +1.26\cdot10^{-11}T^2-2.44\cdot10^{-15}T^3)^{-1}$	$(9.82\cdot10^{-7} +1.6\cdot10^{-10}T)^{-1}$	$(1-\theta)\cdot(ER\_AA7075)^{-1}$
Thermal conductivity, λ (W/(m·K))	$123-6.99\cdot10^{-2}T+1.55\cdot10^{-5}T^2$	$10.1+1.57\cdot10^{-2}T$	$(1-1.5\theta - 0.5\theta^2)\cdot TC\_AA7075$
Density, ρ (kg/m³)	1904-0.01414T	8430	$(1-\theta)\cdot2810$
Thermal capacity, C_p (J/(kg·K))	$34.27+2.72T-9.6\cdot10^{-4}T^2$	$344+2.5\cdot10^{-1}T$	$(1-\theta)\cdot SH\_AA7075$

Source: The Author (2022)

Figure 27 – AA7075 properties: (a) Electrical resistivity; (b) Thermal conductivity; (c) Specific heat.

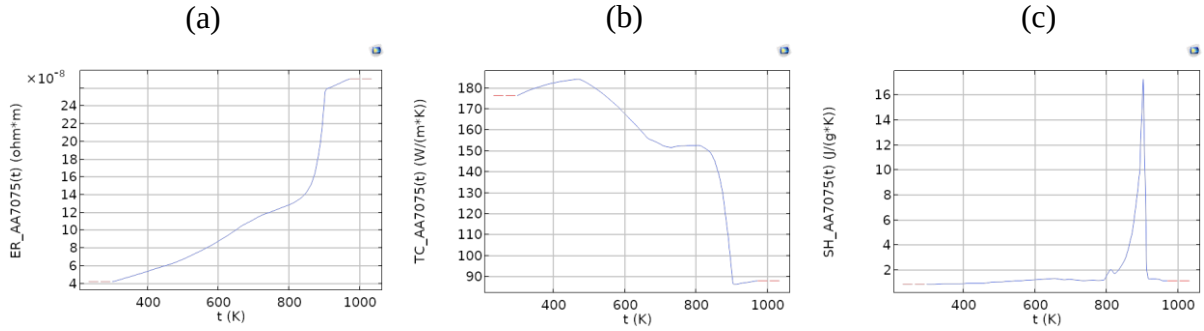

Source: The Author (2022)

3.6.2.3 Boundary conditions

The coupled modeling in COMSOL Multiphysics included the Electric Currents (ec), Heat Transfer in Solids (ht) and Solid Mechanics (solid) modules, and the Domain ODEs and DAEs module for solving the differential equations involving relative density (ρ) and grain size (G).

For the electrothermal modeling the following boundary conditions were applied, on the vertical walls it was considered that there is a radiative heat flux, considering the emissivity of graphite ε = 0.8 and the Inconel 600 electrode ε = 0.67 (MANIÈRE *et al.*, 2016d). As for the horizontal walls, it was considered that there is a conducto-convective heat flux for the two Inconel surfaces that are in contact with the water-cooling system, where the conducto-convective coefficient h_c = 880 $W \cdot m^{-2} \cdot K^{-1}$ was considered (MANIÈRE *et al.*, 2016d). Furthermore, due to the symmetry of the array, it was considered that the fluxes emitted and absorbed by the horizontal surfaces are counterbalanced. For the determination of the electrical and thermal contact resistances, the equations obtained from Manière *et al.* (MANIÈRE et al., 2017a) were used in this work.

To implement the mechanical modeling, boundary conditions presented in Figure 28 were used. The specimen was submitted to a pressure of 50 MPa in the upper part, and in the lower part the displacement in the vertical direction *z* was prescribed as null. In the vertical edge of the specimen, the displacement in the radial direction *r* was also prescribed as null. To consider the thermal effects in the mechanics, the modified Abouaf creep model was applied. To apply the Abouaf model, it is usually necessary to perform some creep tests to determine the parameters *c* and *f*. However, these parameters can be related to the parameters ϕ and ψ of the Olevsky model, as shown in the 2.2.2.5 subsection.

Figure 28 – Boundary conditions – Φ8

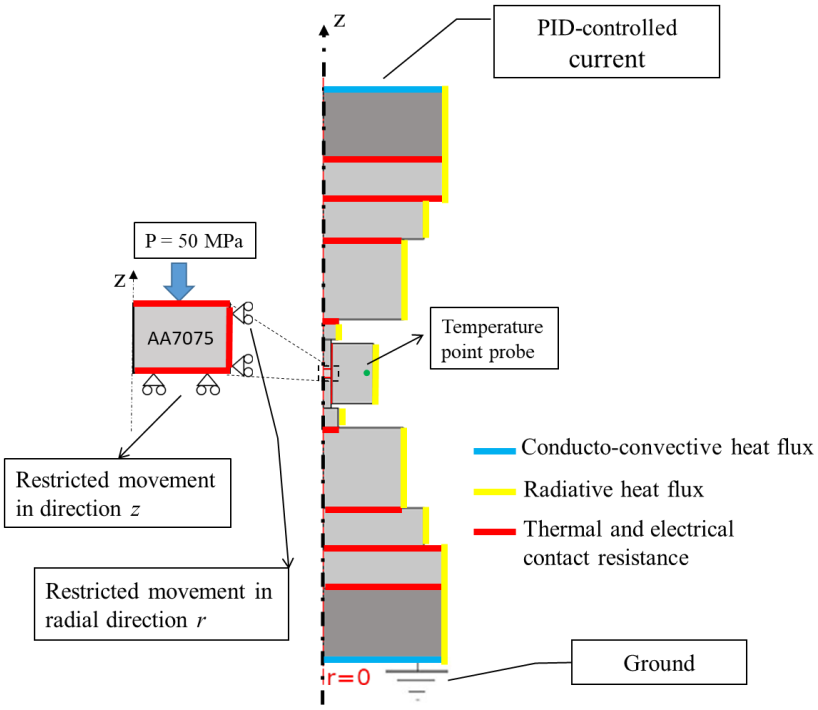

Source: The Author (2022)

The heating occurring during the SPS is due to the Joule effect, so the temperature is controlled by a PID controller, which allows to regulate the electrical input current. The point probe for measuring the temperature was positioned according to the K-type pyrometer used in the experiment, at half height of the mold and at a depth of 3 mm from its external surface. The PID parameters (k_P, k_I and k_D) used are shown in Table 6.

Table 6 – PID control parameters (Φ8)

Parameter	**Value**	**Description**
k_P	7.5	Proportional parameter
k_I	0.1	Integral parameter
k_D	40	Differential parameter

Source: The Author (2022)

3.6.2.4 Mesh used for simulation

The mesh used in the model is shown in Figure 29. This hybrid mesh has a total of 6318 elements, 5618 of which are triangular and 700 rectangular. The rectangular elements were used in the sample and graphite sheet region in order to obtain more accurate temperature and strain results.

Figure 29 – Mesh used in the model - Φ8

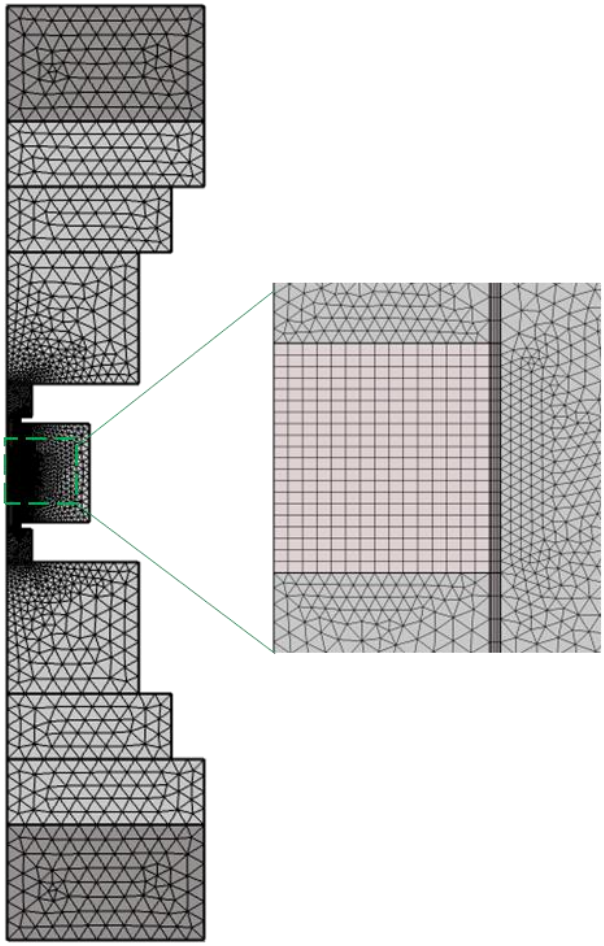

Source: The Author (2022)

3.6.3 Optimization of the SPS parameters by FEM

After validating the Olevsky constitutive model coefficients (A_0, Q and n) for an 8 mm diameter AA7075 sample using the Finite Element Method (FEM) to model its densification, we need to determine the best set of parameters to densify a 20 mm diameter sample (Figure 26(b)), as it is required to be produced for mechanical testing. As in the previous step, all modeling stages were performed in COMSOL Multiphysics software. Thereby, it was possible to vary the SPS parameters to optimize the process and obtain the best settings for pressure, temperature and dwell time. The SPS parameter sets tested are shown in Table 7.

The PID parameters used in the simulations are shown in Table 8. All material properties and boundary conditions are the same as in the previous section, with the exception of pressure and temperature.

Table 7 – SPS parameter sets

Pressure (MPa)	Temperature (°C)	Dwell time (min)
50	500	15
50	550	15
100	500	15
100	550	15

Source: The Author (2022)

Table 8 – PID control parameters (Φ20)

Parameter	Value	Description
k_P	10	Proportional parameter
k_I	0.1	Integral parameter
k_D	30	Differential parameter

Source: The Author (2022)

4 RESULTS AND DISCUSSIONS

This chapter presents and discusses the results obtained in the characterization of the starting powders used to produce AA7075/EAFD composites, presents the mechanical and microstructural characterization of the composites consolidated by the Spark Plasma Sintering (SPS) technique, and also the results obtained in the Finite Element Method (FEM) modeling of the SPS process.

4.1 PARTICLE SIZE ANALYSIS

In this subsection the PARTICLE SIZE ANALYSIS results of the starting powders used are presented. In 4.1.1 the particle size distribution results for the aluminum powders before (AA7075) and after grinding (AA7075-M) are presented. In 4.1.2, in turn, presents the particle size distribution results for Electric Arc Furnace Dust (EAFD).

4.1.1 AA7075 e AA7075-M

The particle-size distribution (PSD) of AA7075 powder before and after ball-milling is shown in Figure 30. The median particle size (D50) is equal to 33 μm for AA7075 (Figure 30a) and to 56 μm for AA7075-M (Figure 30b). The increase in particle size after 1 h of milling in an aluminum alloy (AA6061) was also observed by Rana *et al.* (RANA; BADHEKA; KUMAR, 2016). They showed that the particle size increased from 10–12 μm to 60–65 μm, and attributed this increase to cold welding between the particles, which results in the formation of agglomerates in which the particles are weakly joined at the point of contact. Both PSD are large, in agreement with the SEM observations, and interestingly the PSD for the AA7075-M powder is bimodal, with the minor component centered at about 500 μm, which could also reflect some effects of ball-milling, such as flaking and inter-particle bonding.

Figure 30 – Particle size distribution: (a) AA7075 powder; (b) AA7075-M powder. The solid lines represent the volume fraction and the dashed lines represent the cumulative volume.

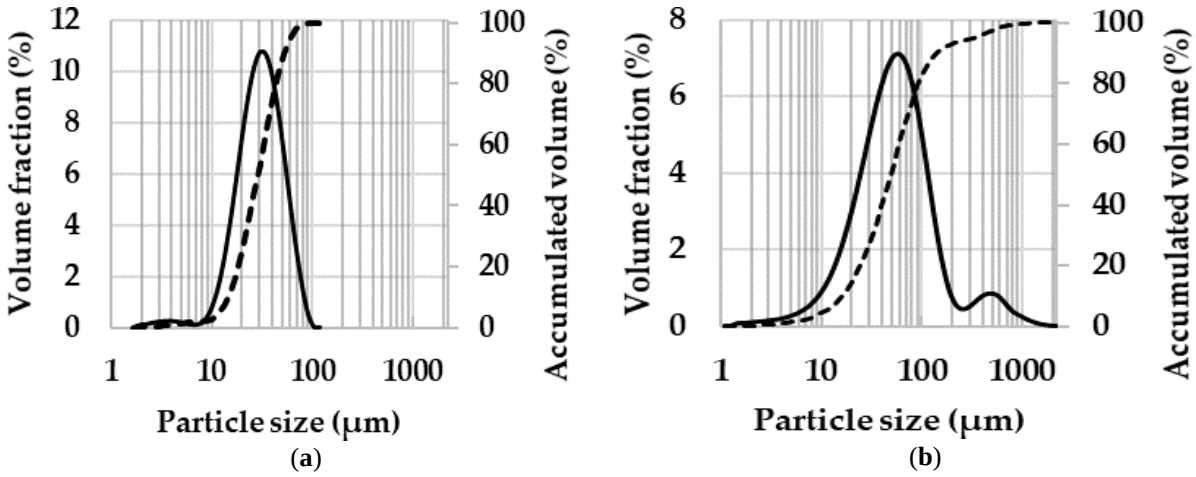

Source: The Author (2022).

4.1.2 Electric Arc Furnace Dust (EAFD)

Figure 31a and Figure 31b show the result of particle-size distribution (PSD) obtained by laser diffraction for EAFD powders called G1 (<53μm) and G2 (53-75 μm), respectively. From this analysis, it was found that the average particle size of G1 and G2 is 13.9 μm and 63.1 μm, respectively. In the PSD of EAFD-G1 (Figure 31a) a bimodal distribution can be observed, denoting the existence of two particle size populations, a portion consisting of fines formed by particles between 0.2 and 13.18 μm and a thicker portion with particles between 13.18 and 120.23 μm, each corresponding to approximately 50% of the volume. This heterogeneous distribution of EAFD was also observed in the results obtained by Tang *et al.*(TANG *et al.*, 2017). Furthermore, it is observed that about 6% is of particles larger than 53 μm, this may be associated with the wear of the sieve or the agglomeration of particles of the powder caused by performing the test in an aqueous medium. For the PSD of EAFD-G2 (Figure 31b) it is also possible to note the bimodal behavior, but with a large difference in peak height. The first group has particles between 0.24 and 17.40 μm, representing only around 12% of the accumulated volume, the remainder is between 17.40 and 158.50 μm. The particles outside the range of 53-75 μm can be explained by the existence of clusters of small particles that did not detach at the time of sieving, as seen in the SEM image, for particles below the lower limit. As for the particles of size above the range, it is justified by the presence of particles in the shape of rods (as can be seen in the SEM images), which allows the passage when the axes of these rods are in a position approximately perpendicular to the sieve hole area.

Figure 31 – Particle size distribution of the EAFD: (a) G1; (b) G2. The solid lines represent the volume fraction and the dashed lines represent the cumulative volume, both as a function of particle size.

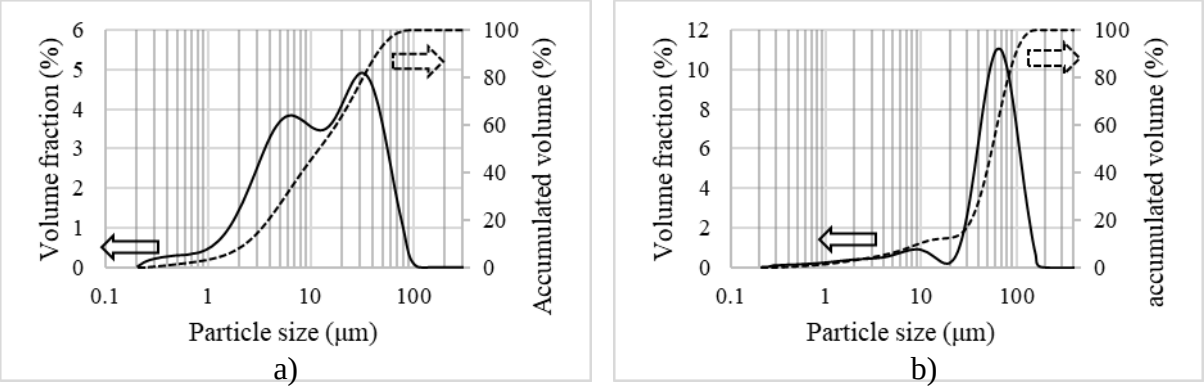

Source: The Author (2022).

4.2 DENSITY

Subsection 4.2.1 presents the density of the starting powders and 4.2.2 presents the density of the sintered composites.

4.2.1 Density of starting powder

The density of the starting powders (G1, G2) was measured by He pycnometry. Ten He purges were performed for each sample to obtain a stable value (Table 9). The difference between G1 and G2 densities is likely due to their different composition, as discussed hereafter. For AA7075, the density provided by the literature, 2.81 g/cm^3, was considered (THE ALUMINIUM ASSOCIATION, 2015). Due to the degree of uncertainty, only three significant figures will be considered for subsequent calculations.

Table 9 – Powder density (ρ_{exp}) of the starting powders.

Sample	**ρ_{exp} (g/cm^3)**
G1	3.7522 ± 0.0007
G2	3.4111 ± 0.0027

Source: The Author (2022).

To calculate the theoretical density ρ_{th} of the mixture between two materials with different densities, $\rho_1$and ρ_2, directly from the mass percentage, here called m_1 and m_2, we can use the following formula:

$$\rho_{th} = \frac{\rho_1 \rho_2}{m_1 \rho_2 + m_2 \rho_1} \tag{62}$$

In another way, we can calculate the density of the sample as a function of the volumetric percentage of the integral powders, as follows:

$$\rho_{th} = v_1 \rho_1 + v_2 \rho_2 \tag{63}$$

where:

$$v_1 = \frac{1}{1+\frac{m_2 \rho_1}{m_1 \rho_2}} \text{ and } v_1 + v_2 = 100\%$$

Thus, the theoretical density of the blends between AA7075 and EAFD, for 5, 10 and 15% residue (by mass) is presented in Table 10.

Table 10 – Theoretical density of composites

Sample	v(%)	$\rho_{th}(g/cm^3)$
5G1	3.79	2.85
10G1	7.69	2.88
15G1	11.68	2.92
5G2	4.16	2.83
10G2	8.39	2.86
15G2	12.70	2.89

Source: The Author (2022)

4.2.2 Density of the sintered AA7075/EAFD composites

The experimental density of the sintered pellets was measured using an Archimedes balance, the value considered is the average between 10 measurements. The relative density is the ratio between the experimental and theoretical density. Samples of 8 and 20 mm in diameter were produced by SPS (Figure 32).

Figure 32 – Some of the samples produced with a diameter of: a) 8 mm and b) 20 mm.

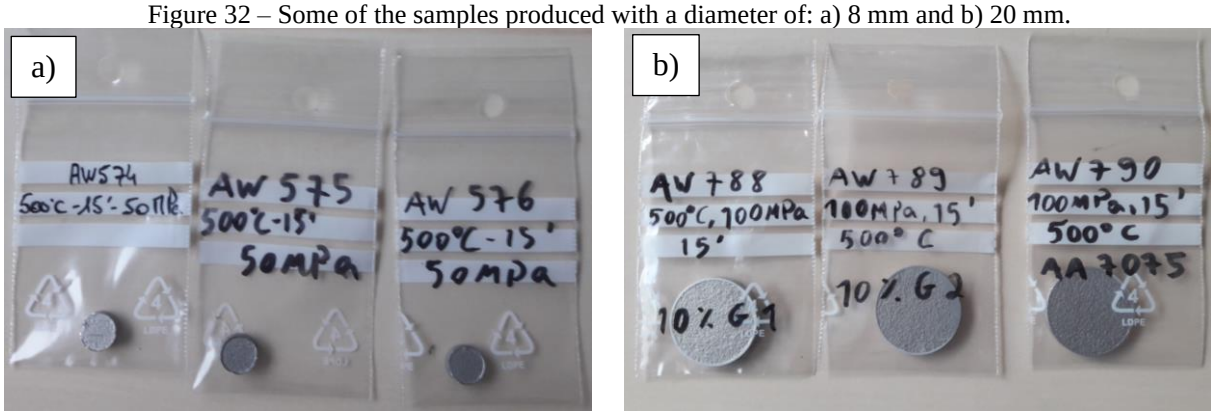

Source: The Author (2022).

4.2.2.1 Density of AA7075-EAFD composites

The relative densities of the sintered 8 and 20 mm diameter AA7075-EAFD samples as a function of their composition and SPS parameters are presented in Table 11 and Table 12, respectively.

Table 11 – 8 mm sintered sample density

Starting powder	SPS parameters			D_{th}(g/cm³)	ρ(%)
	T (°C)	P (MPa)	t (min)		
AA7075-M	500	25	0	2.81	94
AA7075-M	400	50	5	2.81	95
AA7075	500	50	15	2.81	98.4
AA7075-M	500	50	15	2.81	98.6
10G1	500	50	15	2.88	94.1
10G2	500	50	15	2.86	96.7
10G1	500	100	15	2.88	98.4

Source: The Author (2022)

Table 12 – 20 mm sintered sample density

Starting powder	SPS parameters			D_{th}(g/cm³)	ρ(%)
	T (°C)	P (MPa)	t (min)		
10G1	500	100	15	2.88	94.9
10G2	500	100	15	2.86	95.3
AA7075-M	500	100	15	2.81	97.8
10G2	550	100	15	2.86	97.3
AA7075	550	100	15	2.81	99.2
AA7075-M	550	100	15	2.81	99.3
5G1	550	100	30	2.85	96.5
10G1	550	100	30	2.88	97.5
15G1	550	100	30	2.92	98.2
5G2	550	100	30	2.83	99.1
10G2	550	100	30	2.86	97.2
15G2	550	100	30	2.89	100

Source: The Author (2022)

The relative density, combined with other results, is an alternative to know if the sintering was successful (GERMAN, 1996). One of the main difficulties in obtaining a complete densification is related to the release of gases during the beginning of the sintering. This was important because it decreased the vacuum level in the SPS chamber considerably. This fact occurred for all samples, including the sample composed only of aluminum powder AA7075, which did not undergo the milling process. This powder was sintered in its original form and also suffered this release of gases. This implies that this was not an effect of the high energy milling, as it occurred for all samples with and without milling.

The release of gases occurs from the absorption of humidity by the powders during storage, due to the hygroscopic characteristic (i.e. the ability to absorb humidity from the environment) of the oxide layer present in the aluminum powder particles. The oxide layer usually consists of an Al-$Al_2O_3 \cdot nH_2O$ type system, which includes hydrated aluminum oxide, $Al(OH)_3$, and physically adsorbed water (ARBUZOVA, 1976 apud HUO et al., 2010).

In the presence of water, the aluminum grains react with oxygen and form a thin amorphous layer of aluminum oxide, as follows:

$$2Al + 3H_2O \rightarrow Al_2O_3 + 3H_2$$

The change in vacuum in the chamber is associated with the release of oxygen and hydrogen gas from the samples due to the increased temperature and pressure. To get completely dense samples, these gases must be fully released, as they are one of the factors that prevent the reduction of the porosity of the material.

4.3 CHEMICAL COMPOSITION OF THE STARTING POWDERS

The chemical composition of the as-received AA7075 powder determined from EDX analysis is presented in Table 13.

Table 13 – Chemical composition of the AA7075 raw powder determined from EDX analysis.

	Si	**Cu**	**Cr**	**Mg**	**Zn**	**Al**
wt.%	0.10	1.38	0.27	1.71	5.06	91.48

Source: The Author (2022)

Table 14 shows the chemical composition of EAFD obtained by X-ray fluorescence (XRF). This test showed that EAFD (G1 and G2) is composed of several elements, consisting

mainly of iron and zinc. The difference in composition of G1 and G2 is due to the slight density difference between them (Table 9).

Table 14 – X-ray fluorescence (XRF) spectrometry (wt.%).

	Fe	**Zn**	**Ca**	**Mn**	**Si**	**Mg**	**Al**	**Pb**	**Gd**	**La**
G1	39.89	36.93	7.00	4.13	2.74	2.69	1.48	1.22	0.66	0.65
G2	45.33	28.80	7.66	2.99	4.98	2.90	2.02	1.22	0.40	-

	Cr	**K**	**Cu**	**Cl**	**Ti**	**Ba**	**S**	**P**	**Others, each***	**Others, total**
G1	0.52	0.43	0.31	0.27	0.19	0.17	0.16	0.12	0.11	0.44
G2	0.40	0.52	0.30	0.24	0.69	0.29	0.28	0.25	0.15	0.73

* Maximum value.

Source: The Author (2022)

From the data presented in Table 14, it can be highlighted that the EAFD is composed of a large percentage of Fe (between 40 and 45%), with strong presence also of Zn (between 29 and 37%), also presenting considerable values of Calcium (Ca) and Manganese (Mn), Silicon (Si) and Magnesium (Mg), which are the elements that will most influence the quality of the reinforcement.

4.4 X-RAY DIFFRACTION (XRD)

This section presents the XRD patterns of the starting powders and also of the sintered composites.

4.4.1 XRD patterns of the AA7075 and AA7075-M powders and the corresponding sintered samples

The XRD patterns of the AA7075 and AA7075-M powders and the corresponding sintered samples are shown in Figure 34(a). For all samples, only the aluminum peaks are detected (space group n 225 : $Fm\bar{3}m$; Schoenflies notation : O_h^5), showing that all other crystallized phases formed by the other alloying elements are below the detection limit of the technique (GRAULIS *et al.,* 2009). Figure 34(b) shows the magnification of the region around the (111) peak. The (111) peak shifts to a slightly higher 2θ angle, as seen in Figure 34(b) for sintered samples, which can be attributed to the partial dissolution of Zn, Mg and Cu in the Al

matrix as well as grain boundaries (YAZDIAN; KARIMZADEH; TAVOOSI, 2010). The values of crystallite size and intrinsic strain for all samples are shown in Table 2. To obtain these parameters, the values of FWHM and Bragg angle of the first five peaks of the diffraction pattern, indexed as (111), (200), (220), (311) and (222), were used. The high-energy ball-milling process led to a decrease in crystallite size and an increase in lattice strain, due to the severe plastic deformation of the powders during the process, as was reported by several authors (ABDOLI; ASGHARZADEH; SALAHI, 2009; BERA *et al.,* 2013). The plastic deformation generates stresses that imply the formation of subgrain boundaries, thus, grain refinement occurs as the distortions in the lattice increase. The crystallite size is about 61 and 45 nm and strain is about 0.07 and 0.12%, for AA7075 and AA7075-M, respectively. Table 2 also shows the estimated value of the density of dislocations for each sample, which was obtained using eq. (56). Comparing values for AA7075 and AA7075M highlights that milling considerably increases the density of dislocations (DAYANI *et al.,* 2017; TOOZANDEHJANI *et al.,* 2017). Moreover, sintering reduces the density of dislocations, as it increases the size of the crystallite and decreases the strain of the lattice. In addition, by comparing AA7075-MS with AA7075-S, it is possible to notice that the density of dislocations for the former is about four times higher than for the latter, which influences directly the strength and hardness of these samples, as it will be discussed hereafter.

Using Bragg′s Law for cubic structures, the lattice parameter a_0 of the powder and consolidated samples was calculated. Comparing the lattice parameter of the powder samples (0.40549 nm for AA7075 and 0.40553 nm for AA7075M) shows that there is no significant variation. The same occurs for AA7075-S and AA7075-MS, with lattice parameters of 0.40498 and 0.40491 nm, respectively. Comparing the consolidated samples with the powder samples, there is a reduction of about 0.13–0.15%. The reduction in the a_0 occurs due to the formation of a supersaturated AA7075 solid solution caused by the dissolution of smaller Zn and Cu atoms in the Al lattice (TAVOOSI; ENAYATI; KARIMZADEH, 2008; YAZDIAN; KARIMZADEH; TAVOOSI, 2010).

Figure 33 – (a) XRD patterns of the AA7075 and AA7075-M powders and the corresponding sintered samples; (b) higher magnification of the region around the (111) peak. All patterns are normalized to the (111) peak.

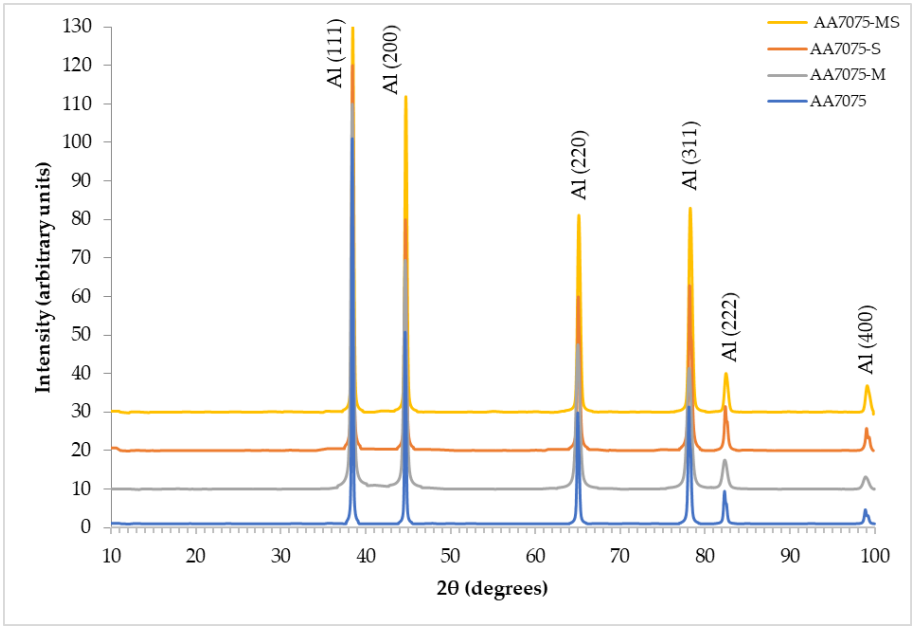

(**a**)

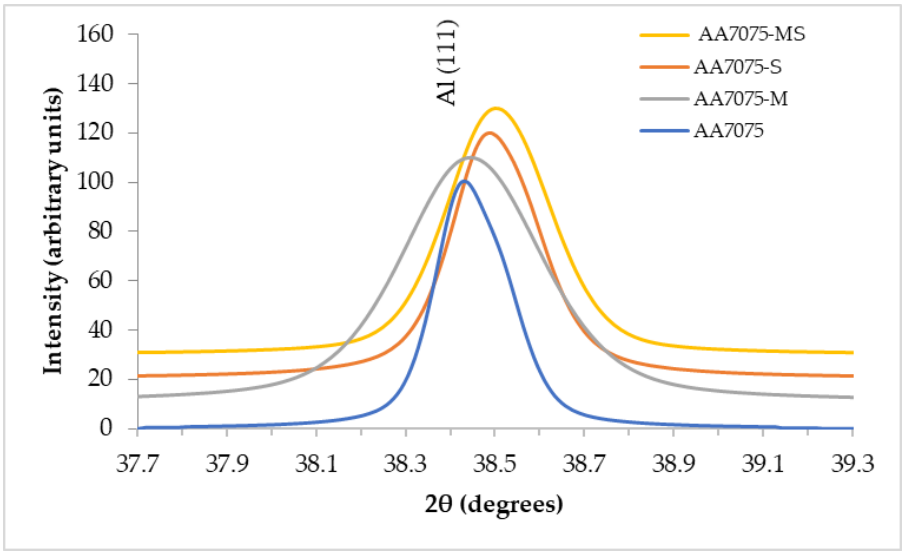

(**b**)

Source: The Author (2022)

Table 15 – Crystallite size D (nm), micro-strain ε (%), lattice parameter a_0 (nm) and dislocation density $\delta(m^{-2})$ powders and dense samples as deduced from the XRD patterns.

Sample	D (nm)	ε (%)	a_0 (nm)	$\delta(m^{-2})$
AA7075	61	0.07	0.40549	1.37×10^{14}
AA7075-M	45	0.12	0.40553	3.26×10^{14}
AA7075-S	80	0.02	0.40498	2.96×10^{13}
AA7075-MS	77	0.08	0.40491	1.32×10^{14}

Source: The Author (2022)

The relative density of the AA7075-S and AA7075-MS sintered samples is 99.2 ± 0.1% and 99.3 ± 0.2%, respectively, using 2.81 g/cm^3 for the theoretical density of AA7075. The XRD patterns of the sintered samples (Figure 34) are similar to those of the corresponding powders.

From the Williamson–Hall method, it was found that the crystallite size of the sample AA7075-S was 80 nm, about 32% larger than its starting powder, and its micro-strain was reduced from 0.07% to 0.02% after sintering. The crystallite size and micro-strain in the sintered AA7075-MS sample are 77 nm and 0.08%, respectively. The crystallite size of this sintered sample is approximately 70% larger than that of its powder. Such results are in good agreement with those obtained by Rana et al., (2009).

4.4.2 XRD patterns of the composites

Table 14 shows the chemical composition of EAFD obtained by X-ray fluorescence (XRF). This test showed that EAFD (G1 and G2) is composed of several elements, consisting mainly of iron and zinc. The difference in composition of G1 and G2 is due to the slight density difference between them (Table 9).

Table 16 – X-ray fluorescence (XRF) spectrometry (wt.%).

	Fe	Zn	Ca	Mn	Si	Mg	Al	Pb	Gd	La
G1	39.89	36.93	7.00	4.13	2.74	2.69	1.48	1.22	0.66	0.65
G2	45.33	28.80	7.66	2.99	4.98	2.90	2.02	1.22	0.40	-
	Cr	**K**	**Cu**	**Cl**	**Ti**	**Ba**	**S**	**P**	**Others, each***	**Others, total**
G1	0.52	0.43	0.31	0.27	0.19	0.17	0.16	0.12	0.11	0.44
G2	0.40	0.52	0.30	0.24	0.69	0.29	0.28	0.25	0.15	0.73

* Maximum value.

Source: The Author (2022).

The XRD patterns (Figure 34) reveal the presence of ZnO and Fe_3O_4 and/or $ZnFe_2O_4$ as major compounds for both the G1 and G2 EAFD powders. Indeed, Fe_3O_4 and $ZnFe_2O_4$ share the spinel structure with close cell parameters and it cannot be concluded here if it is one or the other compound.

The comparison of the relative intensities of the most intense and well separated peaks for each phase, i.e. (311) for Fe_3O_4, (101) for ZnO and (011) for SiO_2, shows that there is more SiO_2 in G2 than in G1, reinforcing the result obtained in XRF, in which it was shown that the presence of the element silicon in G2 is almost double that in G1. On the other hand, results show that the ratio between ZnO and Fe_3O_4 is similar for both powders.

Figure 34 – XRD Patterns of the G1 (Bottom) and G2 (Top) EAFD Powders

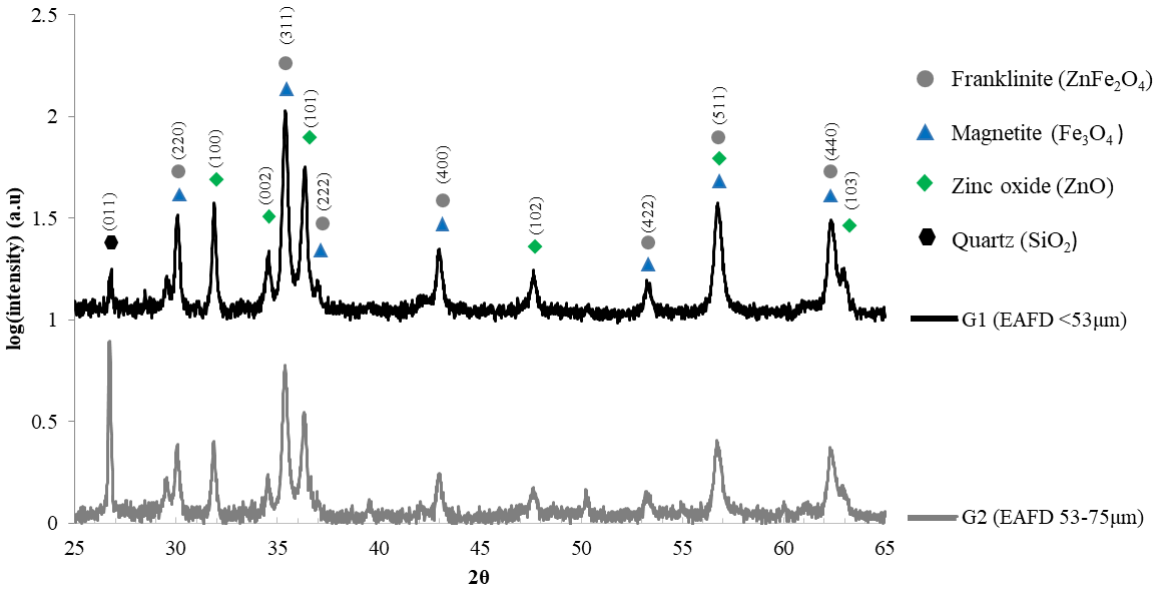

Source: The Author (2022).

The XRD patterns of the powders and sintered samples prepared using the G1 EAFD powder (Figure 35) show intense Al peaks due to the AA7075 matrix and weak peaks attributed to the various oxides present in the EAFD. Note that even for 15 wt.% EAFD, the latter peaks are barely detected. The similarity between the XRD patterns of powders and SPSed samples suggests that no reaction took place during sintering as no new phase was detected. The XRD patterns of the sintered AA7075 and G2/EAFD - AA7075 composites (Figure 36) show similar features.

Figure 35 – XRD patterns of the powders and sintered G1/EAFD - AA7075 composites.

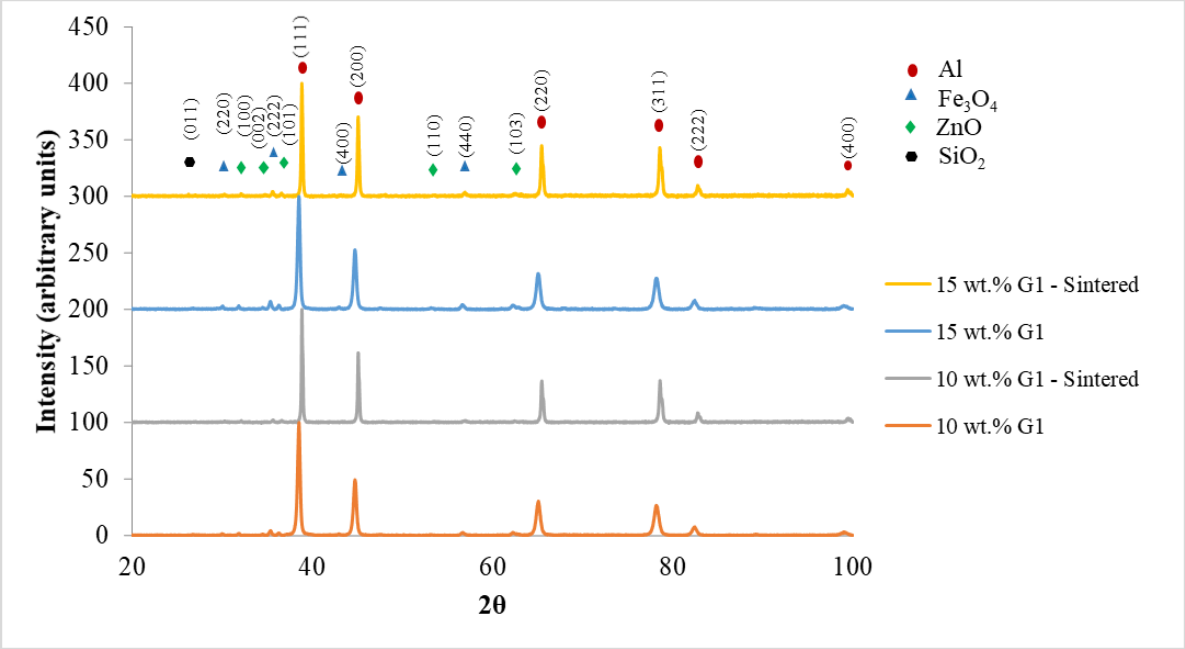

Source: The Author (2022).

Figure 36 – XRD patterns of the sintered AA7075 and G2/EAFD - AA7075 composites.

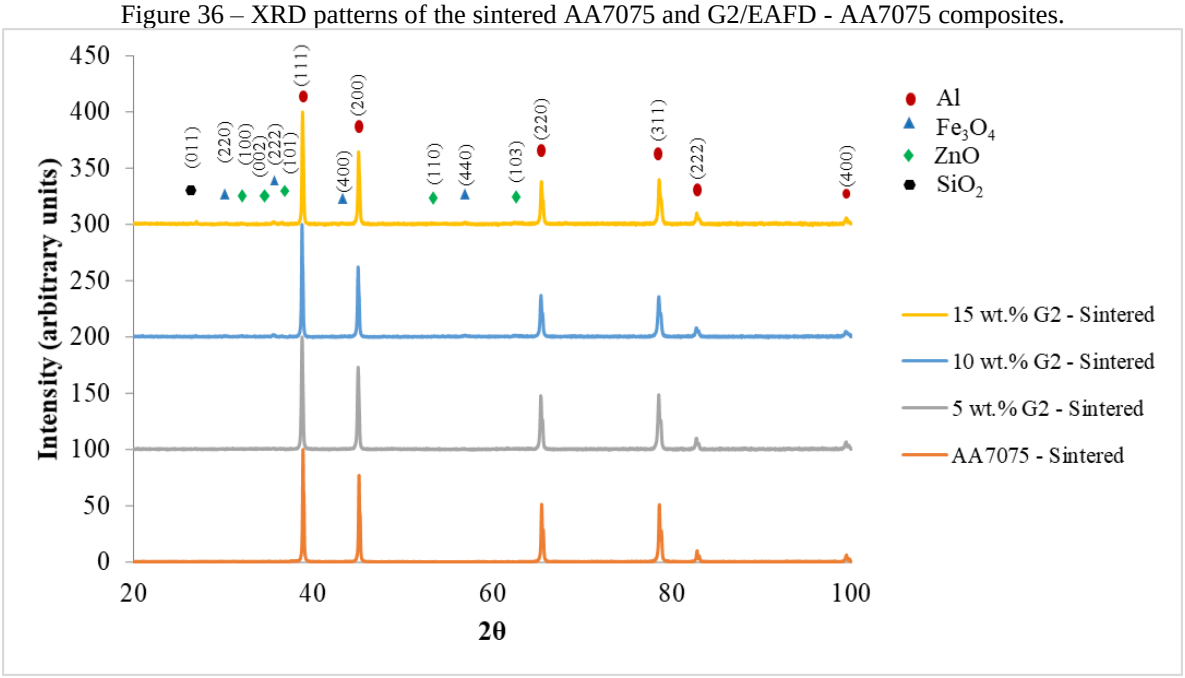

Source: The Author (2022).

4.5 POWDER MICROSTRUCTURE

Subsection 4.5.1 presents the microstructure results of the AA7075 aluminum powders before and after milling. Subsection 4.5.2 presents the microstructure results of the EAFD powders (G1 and G2).

4.5.1 FESEM images of the AA7075

Typical FESEM images of the AA7075 powder at medium (Figure 37 (a)) and higher (Figure 37 (b)) magnifications show rounded particles with a spherical or more elongated shape and a large size distribution, consistent with the gas atomization practices employed for its production (HUO *et al.*, 2010). For the AA7075-M powder, the particles have taken the shape of micrometric flakes about 1 μm thick and with lateral dimensions in the range 10–100 μm, which is a typical morphology for milled soft metals for a short time (≤5 h), as reported in previous works (DAYANI *et al.*, 2017; RAZAVI-TOUSI; SZPUNAR, 2015). In particular, Razavi-Tousi and Szpunar (RAZAVI-TOUSI; SZPUNAR, 2015) found that using various milling conditions, aluminum particles always tend to form disc-shaped particles for short milling times due to cold welding. For longer times (10–50 h), the particle size and its final shape are determined by the equilibrium between cold welding and fracture processes.

Figure 37 – FESEM images of the powders: (a) AA7075 (as-received powder); (b) higher magnification of the boxed area in (a); (c) AA7075-M (milled powder); (d) higher magnification of the boxed area in (c).

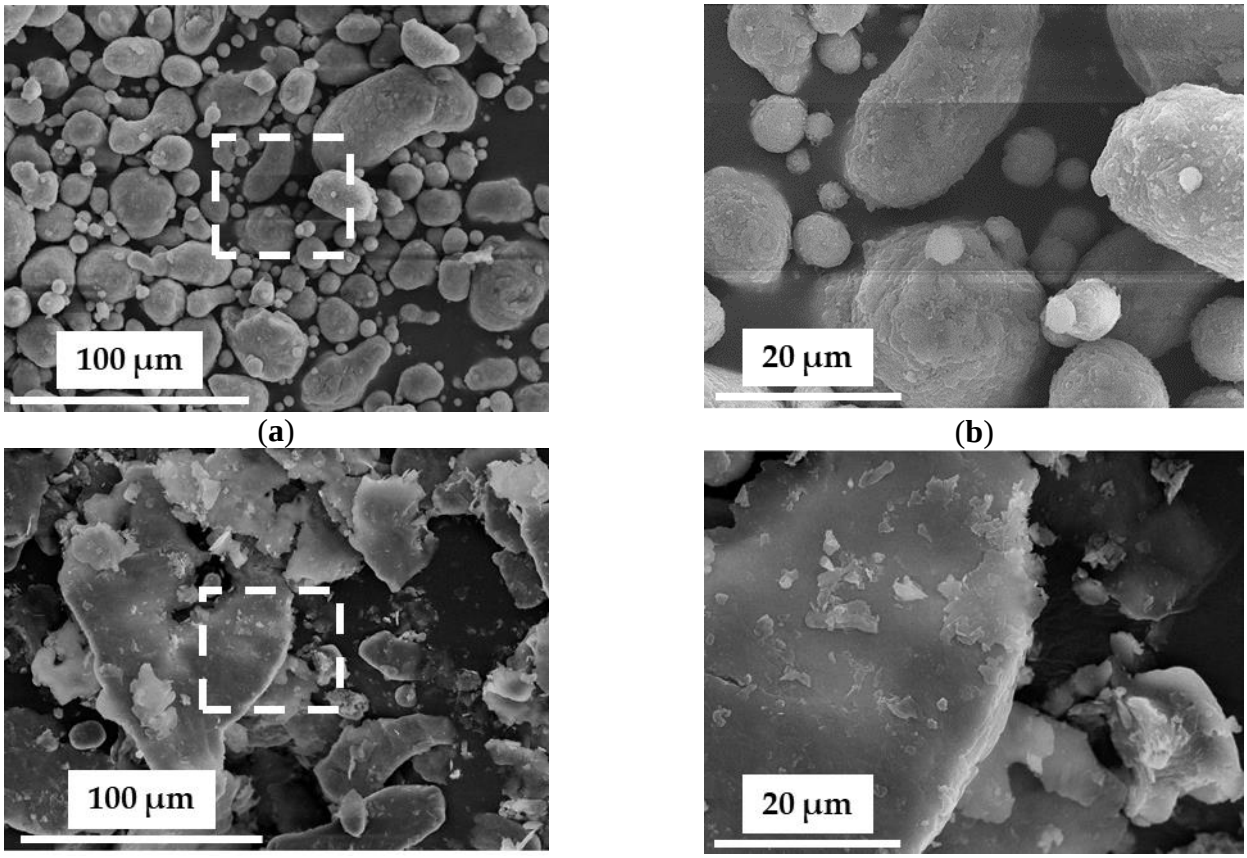

(**a**) (**b**)

(**c**) (**d**)

Source: The Author (2022)

4.5.2 FESEM images of the EAFD (G1 and G2)

FESEM images (Figure 38) of G1 and G2 reveal that they are made up of spherical agglomerates about 50-80 µm in diameter, with submicronic particles in the 0.1 – 1 µm range. This suggests that the agglomerates could be relatively easily broken by milling. A little bit of rod-like particles are also observed (about 300 µm long and 30 µm wide), notably for G2 (inset in Figure 38c). Several authors have verified the presence of these spherical agglomerates formed by fine particles or fine particles covering larger particles. Rocabois pointed out spherical shapes formed from spinel-type metal oxides XFe_2O_4 (X = Fe, Zn, or Mn)(NIUBÓ *et al.*, 2009; OLIVEIRA ALVES *et al.*, 2018; P. ROCABOIS *et al.*, 2000).

Figure 38 – FESEM images of the G1 (a-b) and G2 (c-f) EAFD powder: d) is a magnification from the boxed area in c) and f) is a magnification from the boxed area in d).

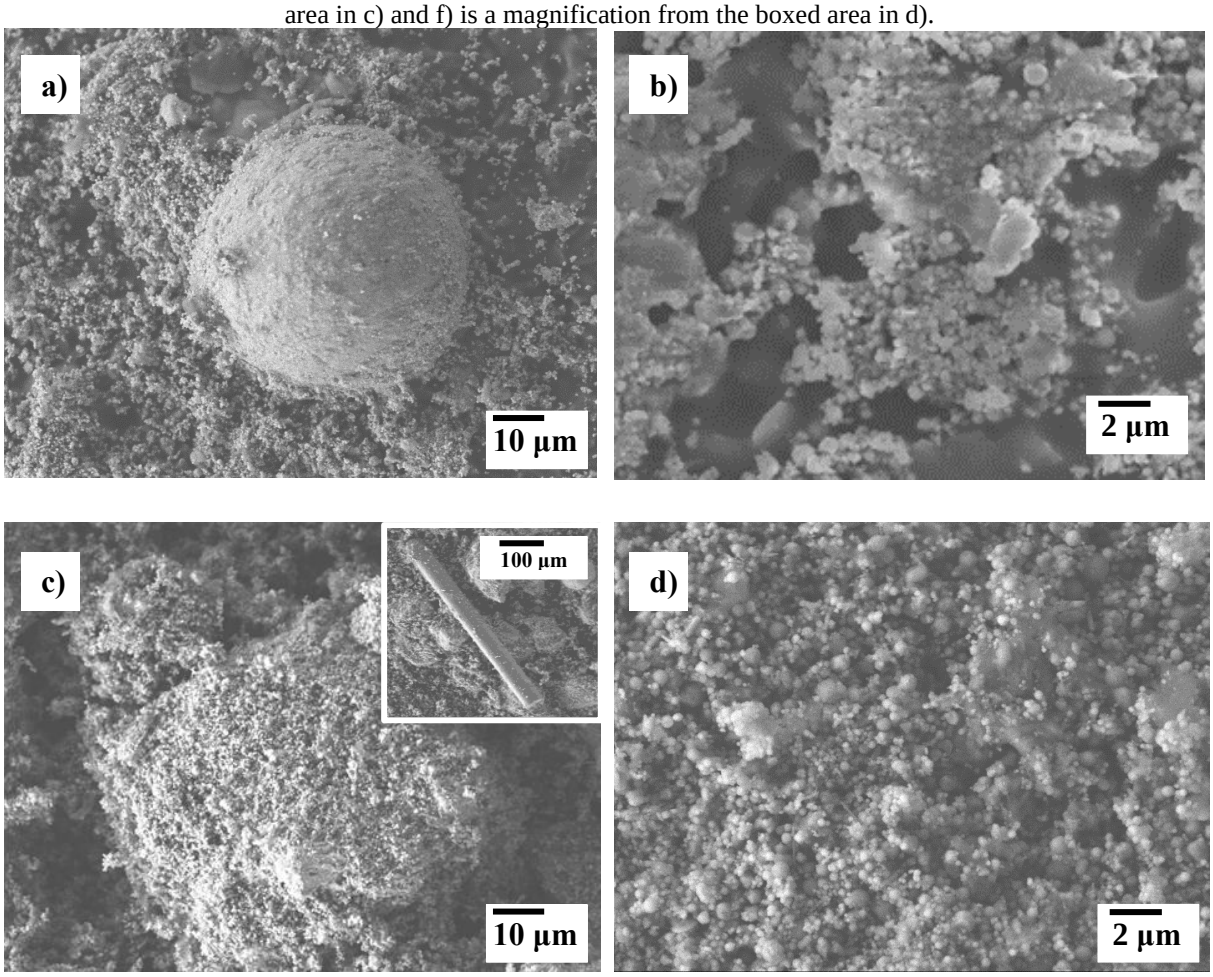

Source: The Author (2022)

For the composite powders the EAFD particles are homogeneously dispersed at the surface of the AA7075 flakes (Figure 39). No micrometric EAFD agglomerates are observed.

Figure 39a and Figure 39b show, respectively, the appearance of the starting powders 15G1 and 05G2 at low magnification. Figure 39c and Figure 39d show higher magnification of selected areas in Figure 39a and Figure 39b, respectively. It is noticed that these powders are very similar, differing only in the surface area covered by EAFD on the AA7075 flakes.

Figure 39 – FESEM images of EAFD - A7075 powders; a) 5 wt.% G2 - A7075; b) is a magnification from the boxed area in a); c) 15 wt.% G1/EAFD - A7075; d) is a magnification from the boxed area in c).

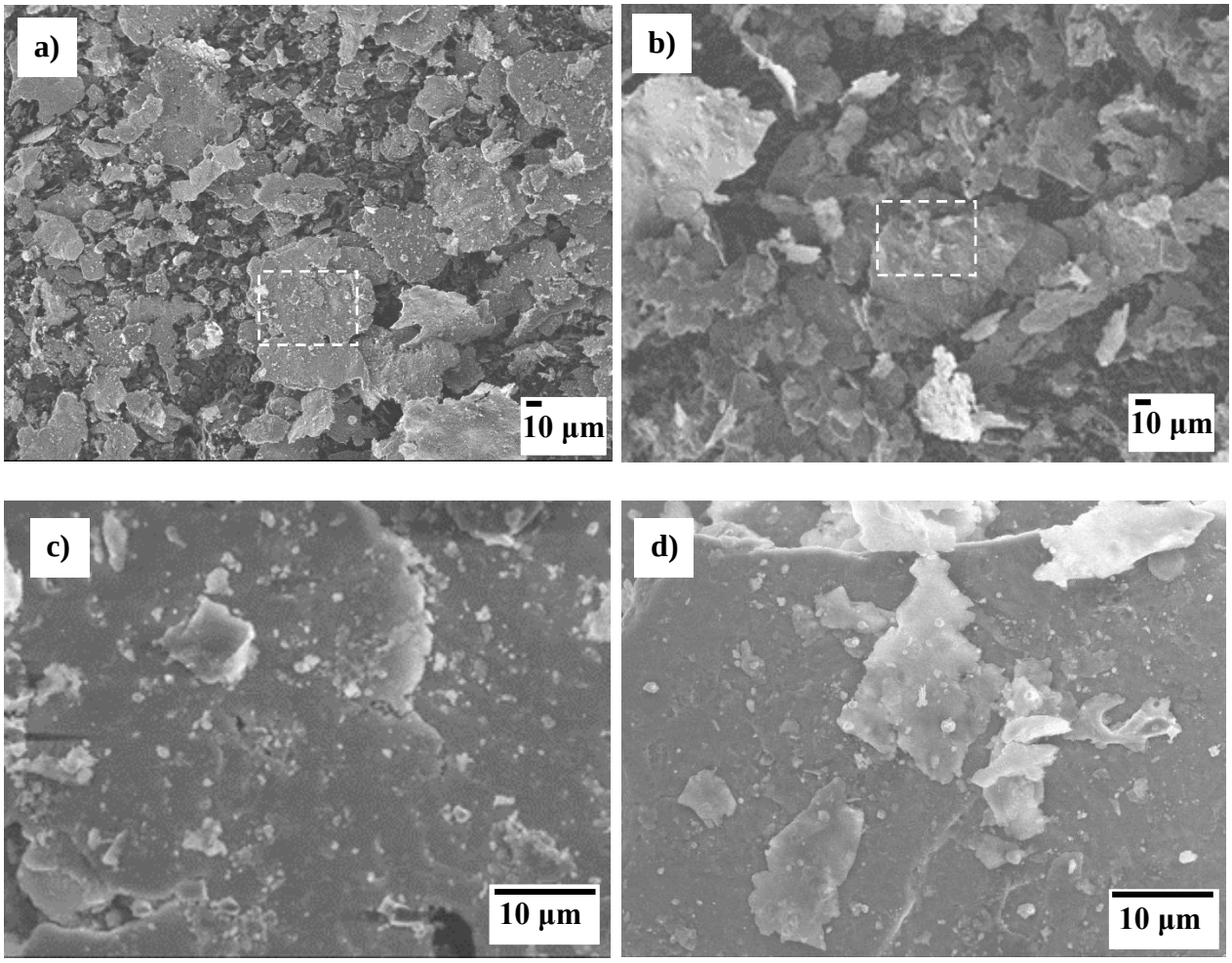

Source: The Author (2022)

4.6 MICROSTRUCTURE OF THE SINTERED SAMPLES

Subsection 4.6.1 presents the results obtained in the determination of the sample preparation protocol for microstructural analysis and in subsection 4.6.2 the images obtained by Optical Microscopy.

4.6.1 Determination of the sample preparation protocol for microstructural analysis

Figure 40 shows the appearance of the sample as sintered (Figure 40a), including the graphite sheet (Papyex), and the mirror appearance obtained after application of the polishing protocol (Figure 40b).

Figure 40 – Macroscopic aspect of the sample: a) as SPSed and b) after polishing.

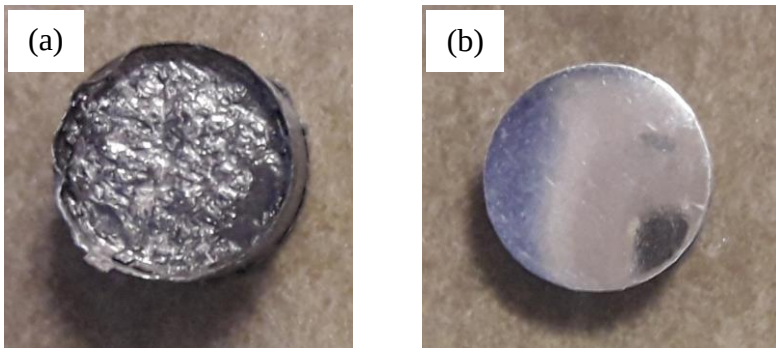

Source: The Author (2022)

The optical microscopy images, as a function of etching time, of the wafers produced with 100% of the AA7075 powder as received are shown in Figure 41 (all images presented have a magnification of 1000x). In the case of the samples composed only of AA7075 in its original form, it can be seen that an etch time of 10s is sufficient to reveal the microstructure. Above this time, we can notice that the solution starts to corrode the interior of the grain, which is not interesting to characterize the samples.

Figure 41 – Optical images of AA7075 samples as a function of etching time: (a) 10s; (b) 20s; (c) 30s; (d) 40s; (e) 50s; (f) 1 min; (g) 2 min; and (h) 5 min

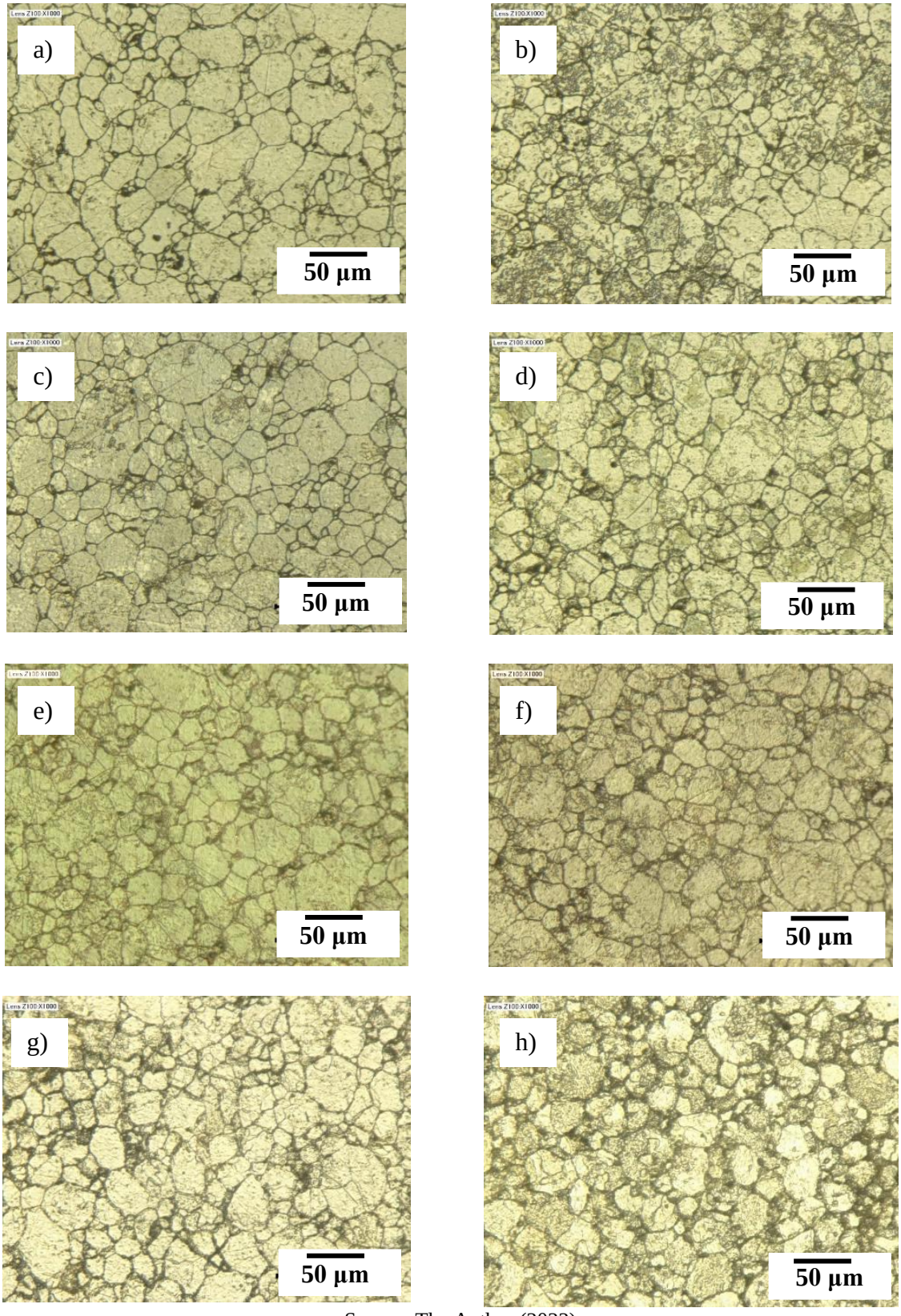

Source: The Author (2022)

Based on the results obtained with AA7075 samples, it was decided to check whether the same chemical etching time, 10s, could also be applied to the EAFD/AA7075 composites produced under the same SPS conditions. In all cases studied in this work, the chemical etching time of 10s proved to be adequate to reveal the microstructure of the samples. Finally, the images obtained under these conditions are shown in Figure 42. It is possible to observe the lamellar appearance of the ground aluminum particles and the evidence of porosity between the particles.

Figure 42 – Optical image of sintered composites: a) 10 wt.% G1; b) 10 wt.% G2.

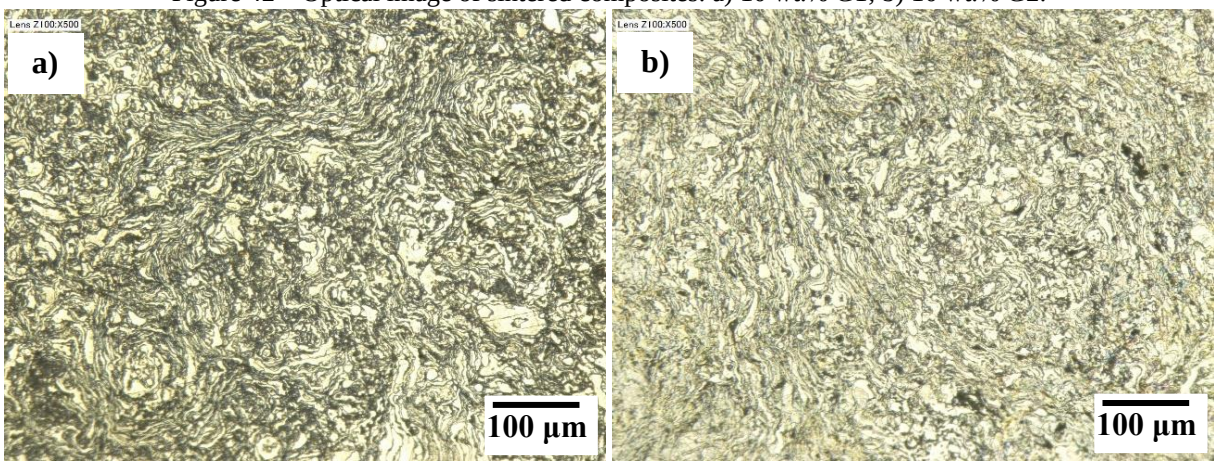

Source: The Author (2022)

4.6.2 Optical Microscopy

In this section, the surface images of the SPSed samples obtained by optical microscopy are presented. Optical microscopy images of the surface of the sintered samples (Figure 43) reveal only very little or no porosity, in agreement with the relative densities higher than 99%. For the sintered AA7075 (Figure 43a), the grain shape is mostly isotropic, reflecting the shape of the particles in the corresponding powder. It is equal to 34 ± 2 µm, which is close to the median value for the corresponding powder (33 µm), indicating no or very little grain growth during SPS. The sintered AA7075-M (Figure 43b) exhibits a lamellar morphology, with a few micrometers in thickness and dozens in length, as for the starting powder. Some grains are observed on the thin side and some on the broad side, indicating no preferential orientation with respect to the pressing axis.

Figure 43 – Optical images of the sintered samples: (a) AA7075, (b) AA7075-M.

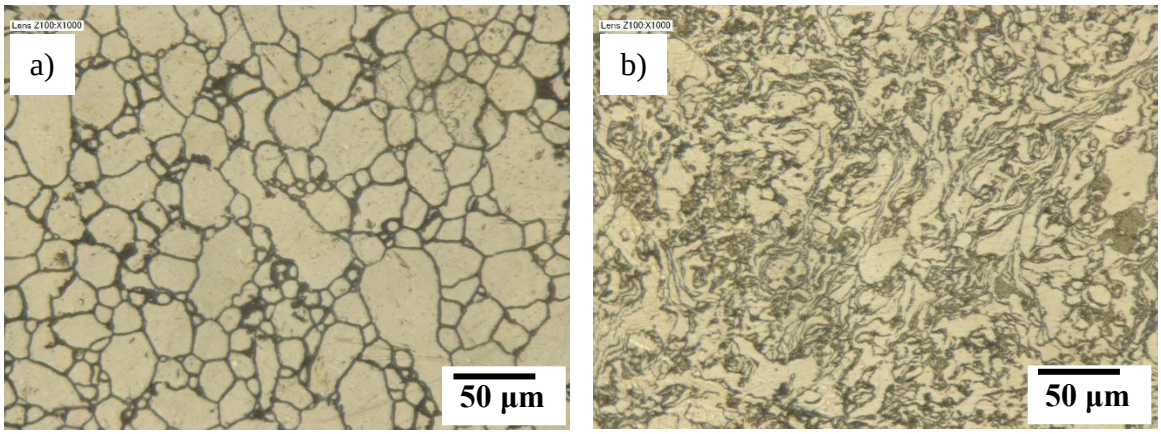

Source: The Author (2022)

4.7 MECHANICAL TESTS

Figure 44 shows the identation points of one of the analyzed samples. Three-point bending tests on 2 x 2 x 16 mm^3 bars were performed (MTS Systems 1/M) at loading rate of 0.1 mm/min.

Figure 44 – View of indentation points of one of the samples studied.

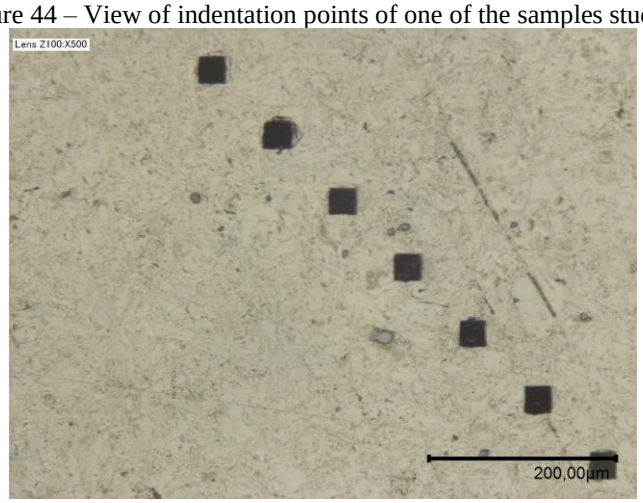

Source: The Author (2022)

4.7.1 AA7075 and AA7075-M

Table 16 compares the Vickers microhardness values obtained for 8 mm in diameter and 3mm thick samples sintered from AA7075 powder (as received) and AA7075-M powder (milled for 1h) from Alcoa, fabricated with the following SPS parameters: heating rate =

100°C/min; dwell temperature = 500 °C; dwell time = 15 min; axial pressure = 50 MPa, with the standard machine current pulse.

Table 17 – Microhardness

Starting Powder	Microhardness (HV)
AA7075	87±4
AA7075-M	109±2

Source: The Author (2022)

Microhardness results show that milling has a beneficial effect in increasing the hardness of the AA7075 alloy, since the sample produced from the aluminum alloy milled for one hour (AA7075-M) shows an increase of approximately 25% over the original powder (AA7075).

In order to obtain specimens with adequate size for the production of specimens for 3-point bending test, specimens with a diameter of 20 mm were produced from Alcoa's aluminum alloy. Among the SPS configurations tested, the most effective set of parameters were as follows: heating rate = 100°C/min; dwell temperature = 550 °C; dwell time = 15min and axial pressure = 100 MPa, with the standard machine current pulse.

The results of the mechanical tests for specimens with a diameter of 20 mm are presented in Table 18. Both the Vickers microhardness HV (HV) and transverse rupture strength σ_u (MPa) are higher for AA7075-MS than for AA7075-S, whereas the transverse rupture strain ε_u is lower. These results could reflect the changes in crystallite size, micro-strain and dislocation density caused by ball-milling for the AA7075-M powder, which are associated with both dislocation and solid solution strengthening. It is well known that metals sintered from milled powders tend to have higher hardness and strength than powders sintered as received due to grain refinement; however, they tend to become less ductile (VALIEV *et al.,* 2016; ZHU; WU, 2018). Increasing the strength of metals without major losses of ductility still remains a challenge in materials engineering (LIU *et al.,* 2019). Post-heat treatments, such as annealing, are used to regain ductility (QUEUDET *et al.,* 2017; RANA *et al.,* 2009), reducing the residual stress of dense samples. The residual stress in materials is undesirable as it can cause pre-existing cracks that result in material damage or early fracture (LIU *et al.,* 2014). Research on methods to recover the ductility without reducing the strength of dense metallic samples is of great interest for further works. Higher dislocation density makes plastic deformation more difficult, as dislocations interact with each other and act as barriers that hinder their own movement. Thus, the increase in the dislocation density in a metal increases the yield strength

of the material (COURTNEY, 2005). The solid solution strengthening occurs due to the presence of other elements (such as Zn, Mg, Cu) alloyed with the Al matrix as solute atoms that differ from the matrix atoms in size, which can cause a variation in the strain fields. These created local strain fields interact with the dislocations and prevent their movement, also causing an increase in the yield strength of the material (MA *et al.,* 2014). Therefore, these two strengthening mechanisms are associated with each other, as the greater the dislocation density, the greater their interaction with the local strain fields created by the elements in solid solution.

Table 18 – Mechanical properties of the AA7075-S and AA7075-MS samples: Vickers microhardness H (HV), transverse rupture strength σ_u (MPa), transverse rupture strain ε_u (—).

Sample	**H (HV)**	**σ_u (MPa)**	**ε_u (—)**
AA7075-S	86 ± 2	498 ± 12	$(5.9 \pm 0.4)\cdot 10^{-2}$
AA7075-MS	108 ± 2	550 ± 5	$(3.2 \pm 0.1)\cdot 10^{-2}$
AA7075-AC (KALKANLI; YILMAZ, 2008)	—	≅ 400	—
AA7075-T6 (KALKANLI; YILMAZ, 2008)	—	≅ 450	—

Source: The Author (2022)

It is interesting to underline that the values for the present samples prepared by the one-step SPS technique are higher than those reported for samples prepared by conventional manufacturing processes using long periods of heat treatment. For example, AA7075 samples prepared by casting and T6 thermal treatment (BARADESWARAN; ELAYA PERUMAL, 2014) showed a bending strength equal to about 330 MPa. Using a vertical squeeze casting process, Kalkanli and Yilmaz (KALKANLI; YILMAZ, 2008) obtained AA7075 samples with a bending strength equal to about 400 MPa (as-cast) and 450 MPa (T6).

4.7.2 EAFD/AA7075 composites

The Vickers microhardness changes considerably upon the increase in EAFD content, as observed in Figure 45. Results show that 15 wt.% G1/AA7075 and 15 wt.% G2/AA7075 composites have a hardness 55% and 40% higher than AA7075, respectively.

It was noticed that the microhardness values do not tend to vary with position, indicating that the SPSed composites are homogeneous.

Figure 45 – Vickers microhardness of G1, G2 and AA7075 samples *versus* EAFD content.

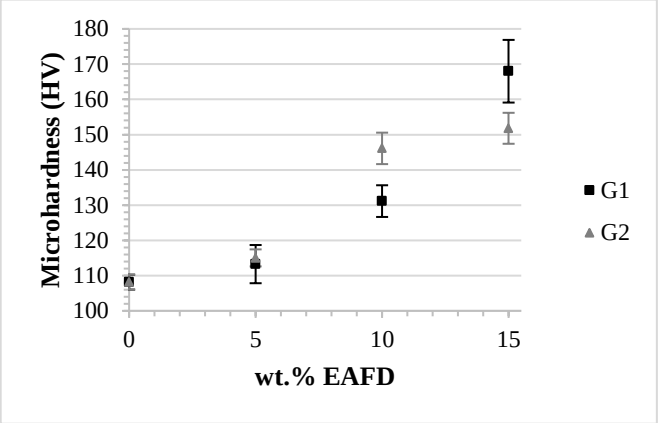

Source: The Author (2022)

The results presented in Figure 45 demonstrate that both EAFD size ranges (G1 and G2) indicate that they possibly have application potential as reinforcement in AA7075 matrix composites, mainly in parts produced on the basis of AA7075 that need greater microhardness without increasing the cost of production. In this sense, EAFD seems to be a good alternative to replace some conventional particulate reinforcements used in composites with AA7075 matrix, such as SiC, TiC and Al_2O_3, among others (ALANEME; SANUSI, 2015; BALAJI; SATEESH; HUSSAIN, 2015; CANAKCI; VAROL, 2014; KARUNANITHI; GHOSH; BERA, 2014; PRADEEP DEVANEYAN; GANESH; SENTHILVELAN, 2017; RANA; BADHEKA; KUMAR, 2016; RAO, 2017; SHEN *et al.*, 2014; VENKATESAN *et al.*, 2014).

According to references (FLORES-VÉLEZ *et al.*, 2001) and (ADEOSUN *et al.*, 2012), the maximum improvement in mechanical properties of Al matrix composites occurs by using around 10 wt.% EAFD. However, it was observed in the present work an increase in microhardness (Hv) up to 15 wt.% of EAFD. In the reference sample, produced from the AA7075, the Vickers microhardness value obtained was 108 Hv, whereas in composites with 15% EAFD, the microhardness reached 152 Hv using G2 (EAFD with particle size between 53 µm and 75 µm), and 168 Hv using G1 (EAFD with particle size smaller than 53 µm). This difference is probably related to the technique of Spark Plasma Sintering used in this research, which has several advantages over conventional production techniques (TOKITA, 2013; ZHANG *et al.*, 2014), among them the ability to produce materials with very low porosity and prevent grain growth. Using a conventional powder metallurgy technique, Flores-Vélez et al. (FLORES-VÉLEZ *et al.*, 2001) reported that the relative density of EAFD/Al composites decreases as a function of the EAFD content, when using 10 wt.% of EAFD the relative density was 85%. In contrast, the relative density of the EAFD/AA7075 composites produced

by us using the SPS technique varied between 96.5 and 100%, even using a shorter cycle, showing the superiority of this technique over conventional powder metallurgy techniques.

4.8 FINITE ELEMENT MODELING – AA7075

This section presents the results obtained by modeling the Spark Plasma Sintering (SPS) process by Finite Element Method (FEM).

4.8.1 Determination of the creep parameters Q, A_0 and n

For the determination of the creep parameters of Olevsky's model, the starting powder AA7075 processed by high-energy milling for 1 hour was used. The SPS parameters used for the sintering of this material were as follows: applied pressure = 50 MPa; heating rate = 100 ºC/min; dwell temperature = 500 ºC; dwell time = 15 min. The sample used for this test was 8 mm.

The Figure 46 shows the curves referring to the displacement of the upper punch in the Z axis. The curve presented in blue describes the displacement in the vertical direction (z-axis) during the densification of the sample. This displacement is the result of the densification of the sample and also the thermal expansion of the SPS machine tools. The curve presented in red corresponds to a cycle in which the sample is completely dense, that is, this displacement is a result only of the thermal expansion of the tools. To obtain the curve of effective densification it is necessary to subtract the red curve from the blue one, and by doing this, the gray curve is obtained.

Figure 46 – SPS machine piston displacement as a function of time.

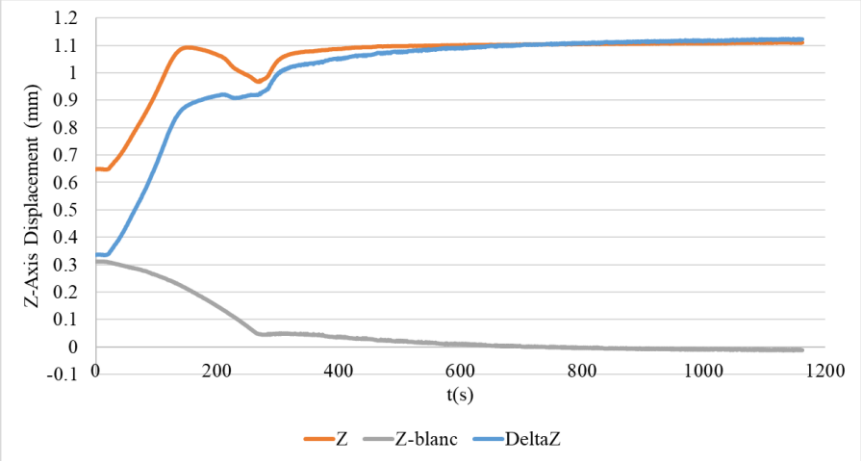

Source: The Author (2022).

From the effective Z-displacement, we can obtain the densification curve for the AA7075 alloy, which is presented in Figure 47.

Figure 47 – Densification curve for AA7075 powder.

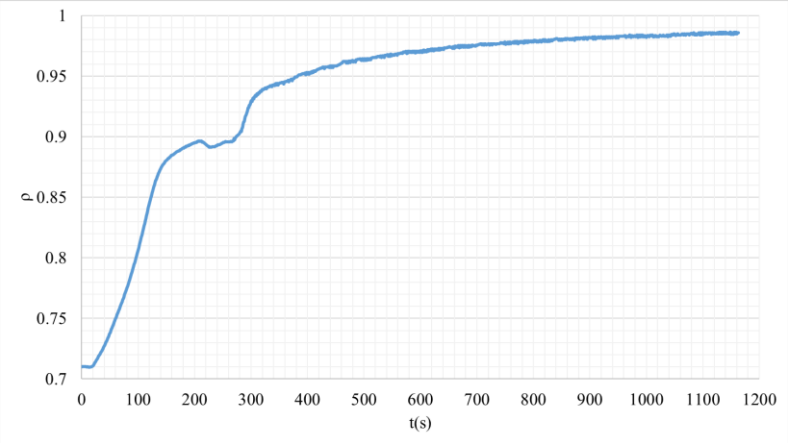

Source: The Author (2022).

After obtaining the densification curve, Olevsky's method was used to obtain the creep parameters Q, A_0 and n of AA7075. Figure 48 shows the curves obtained by regressions with n varying from 1 to 5.

Figure 48 – Linear regression to determine A_0, Q and n qualitatively.

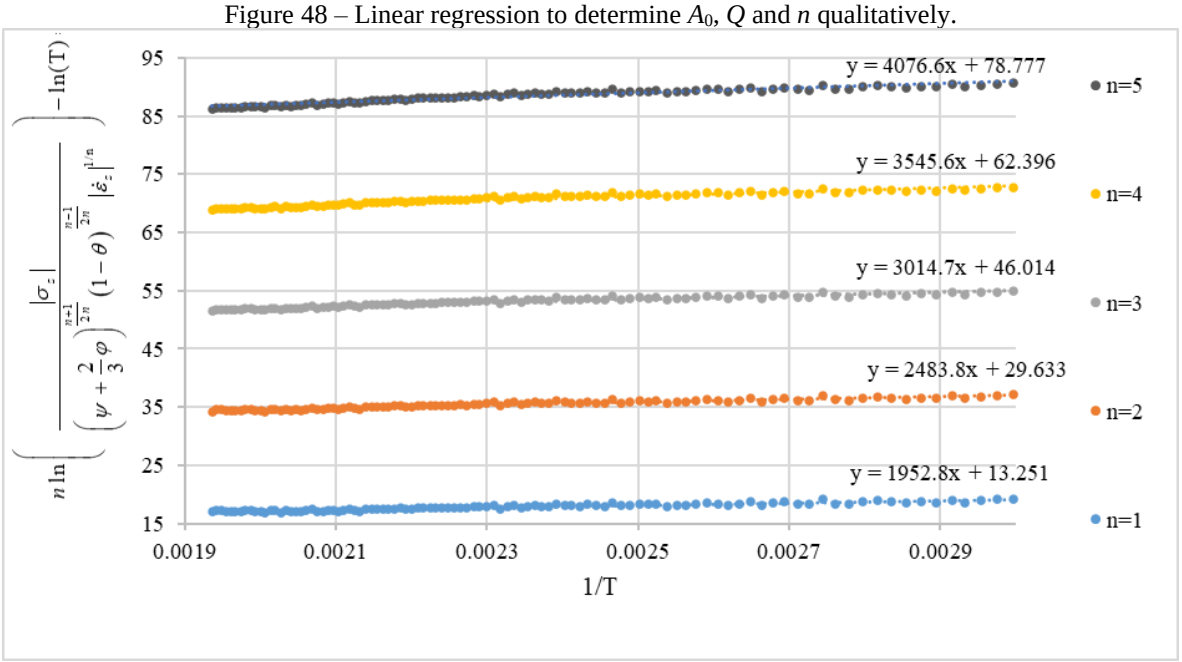

Source: The Author (2022)

The values of Q and A_0 are obtained from the coefficients of the equations of the lines shown in Figure 48, and are presented in Table 19.

Table 19 – Values of Q and A_0 depending of each n.

n	Q(kJ/mol)	A_0(1/s)
1	16.2	1.76E-06
2	20.7	1.35E-13
3	25.1	1.04E-20
4	29.5	7.98E-28
5	33.9	6.13E-35

Source: The Author (2022)

From the determination of the creep parameters, it was possible to obtain the densification curves as a function of time and compare them with the experimental values, as illustrated in Figure 49. Results show that the value of n evaluated qualitatively is between 3 and 4, but it is difficult to state what the exact value is. Therefore, the method of Li *et al*(LI *et al.*, 2012) was used to obtain the n parameter in a quantitative way.

Figure 49 – Comparison between the experimental density and the density obtained numerically.

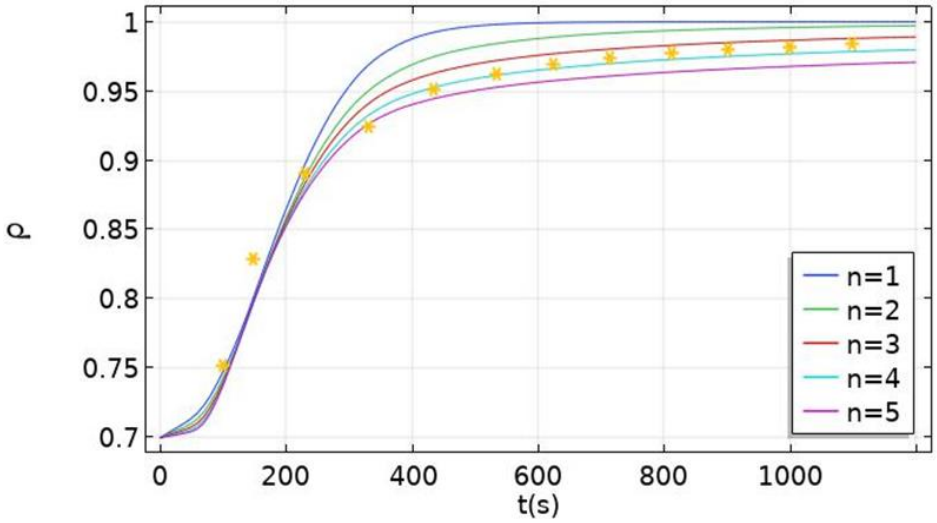

Source: The Author (2022)

To determine the n exponent by the method of Li *et al.*, three temperatures were adopted to perform the experiment: 150, 200 and 250 °C. For each test, the pressure varied between 10 and 50 MPa, with an increment of 10 MPa at each step. The punch displacement (sample shrinkage) and pressure levels as a function of time are presented in Figure 40.

Figure 50 – Tests performed to determine the n exponent.

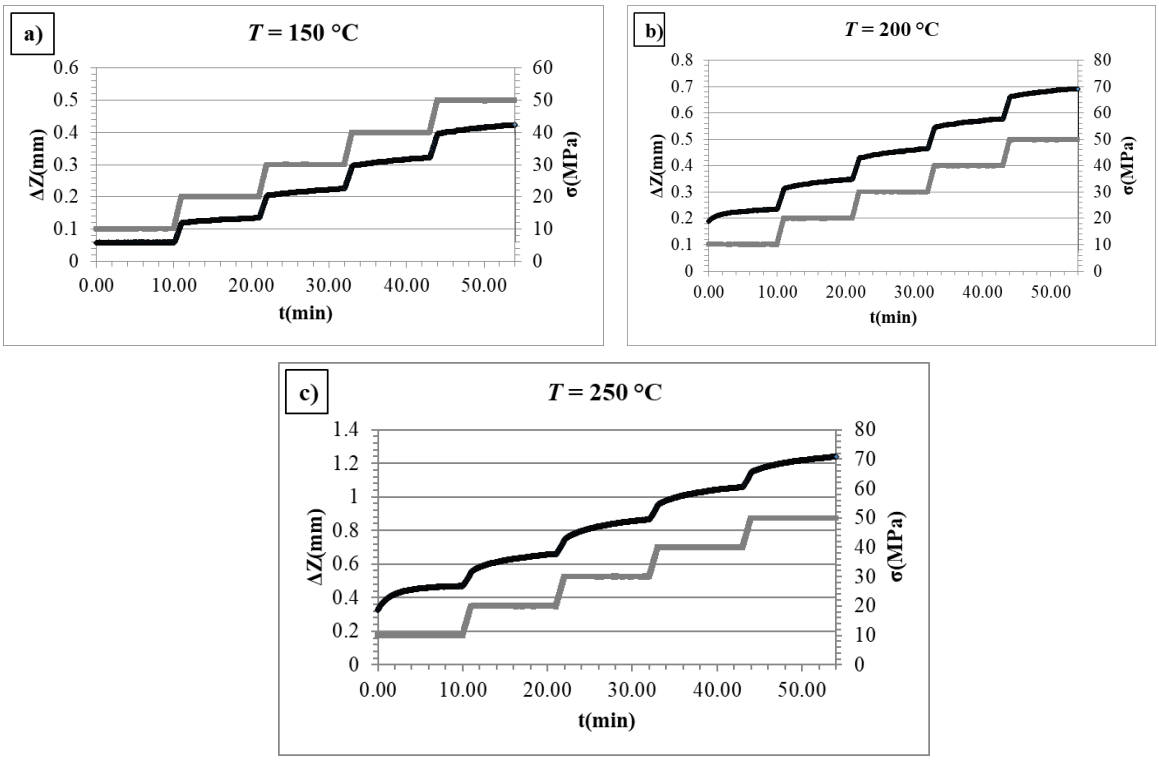

Source: The Author (2022)

From the shrinkage data of the specimen as a function of time, presented in Figure 50, it can be highlighted that the total shrinkage of the specimen increases as a function of the temperature at which the test is performed. Using the method of Li *et al.* (LI *et al.*, 2012), the exponents n of the power creep law were determined, and the respective values are presented in Table 20.

Table 20 – *n* values obtained by using Li *et al.* method.

T_{test} (°C)	n	Standard Deviation
150	3.05	±0.16
200	4.02	±1.17
250	4.58	± 1.16

Source: The Author (2022)

As presented in Table 20, the average value of n obtained by the method of Li *et al*(LI *et al.*, 2012). is approximately 3.88. An analysis between the two methods induces n = 4. Thus, the activation energy *Q* of the AA7075 alloy is 29.5 kJ/mol and the A_0 factor is $7.98e^{-28}$ s^{-1}.

4.8.2 Creep Data Validation via FEM

In order to use the creep data in the finite element modeling, it is necessary to verify if they are reliable, in order to develop a robust predictive numerical tool for future tests, that can predict some important results from the sintering of samples by SPS, such as: final density, particle size, etc. For this, the SPS cycle of sample AA7075 was modeled using Comsol Multiphysics, with the following sintering parameters: pressure of 50 MPa, temperature = 500º C and dwell time = 15 min. After that, the numerical results were compared with the experimental ones.

The Figure 51 shows the PID-controlled temperature obtained numerically (solid blue line) compared to the experimental temperature data measured during the process (green circles). It can be highlighted that the temperature curve obtained with the simulation is very close to the experimental one, proving the effectiveness of the PID controller used.

Figure 51 – PID-Controlled temperature obtained by simulation and experimentally

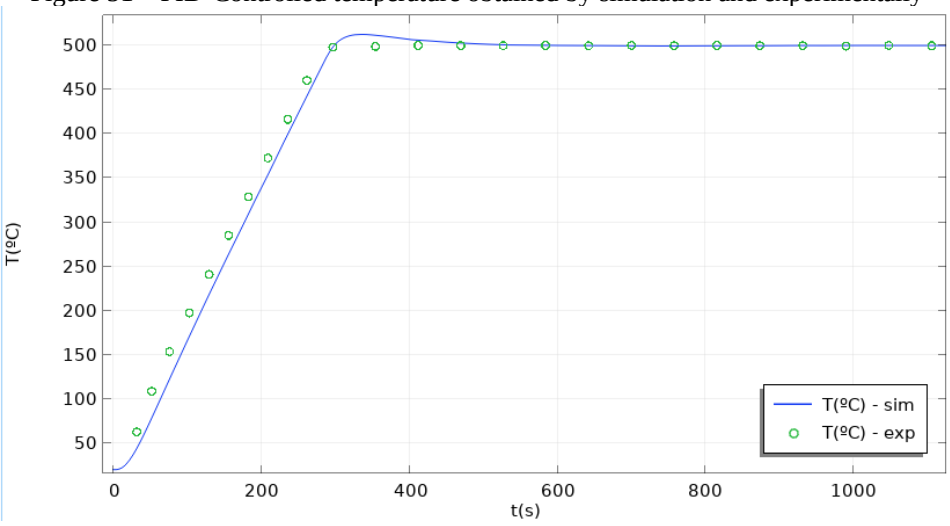

Source: The Author (2022)

The curve showing the evolution of the relative density according to the time of the process is presented in Figure 52. The continuous curve (in blue) represents the result obtained by simulation, while the asterisks (in green) represent the data obtained experimentally. It is possible to notice that at the end of the sintering process, numerical and experimental values are very close, since experimental value reaches 98.6% while simulation value reaches 98.0%. It demonstrates that this method can be used to predict the best set of parameters that should be adopted to optimize the densification of the sintered samples.

Figure 52 – Evolution of the relative density according to the sintering time obtained in the simulation *versus* the experimental one

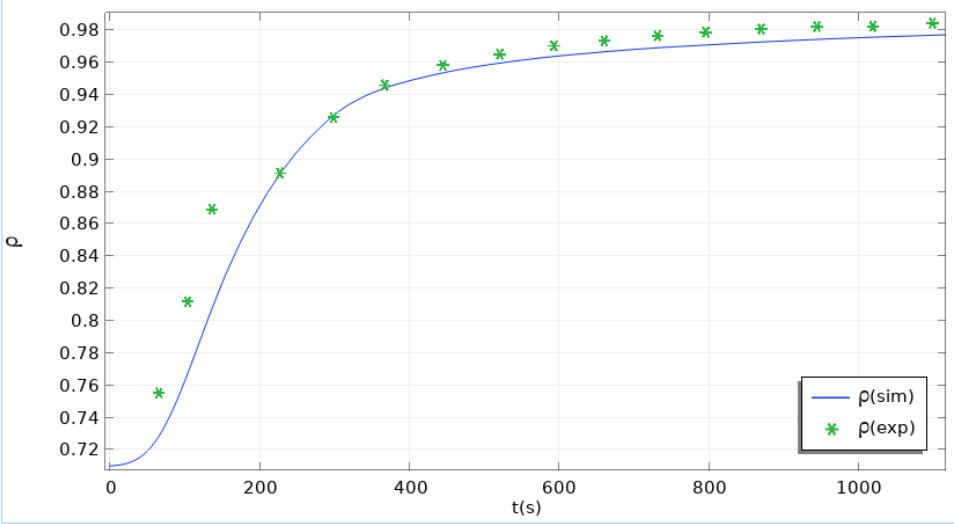

Source: The Author (2022)

Figure 53 illustrates the distribution of the relative density in the AA7075 sample at the end of the sintering process, obtained by simulation with COMSOL Multiphysics software. Results show that the density of the sample is quite homogeneous, proving that the temperature is well distributed throughout the sample, as can be seen in the Figure 54.

Figure 53 – Distribution of the simulated relative density obtained at the end of the sintering process.

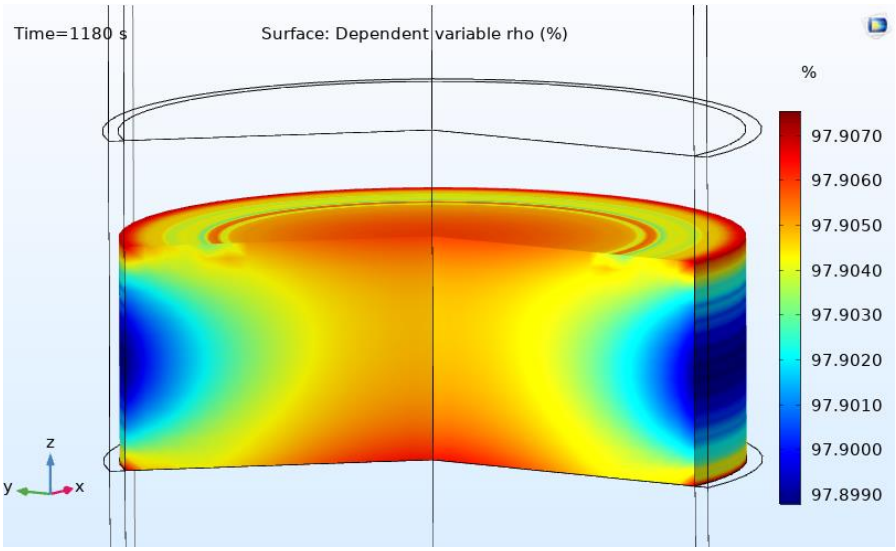

Source: The Author (2022)

Figure 54 shows the temperature distribution between the punches, mold and sample during the SPS cycle. Figure 54a shows the temperature at the moment near the beginning of the SPS cycle (100s), Figure 54b the temperature at the end of heating (288s), Figure 54c at

the moment near the middle of the dwell time (700s) and Figure 54d at the end of the cycle (1180s). It is possible to notice that during heating the highest temperatures occur in the pistons, already at the dwell time the temperatures of the set punches/mold/sample are very close, around 500° C, according to the color scale, ensuring a homogeneous temperature distribution in the sample and, consequently, the uniformity of the sample density and also of the medium particle size. At all times it is noted that the temperature in the sample is homogeneous, as previously stated.

Figure 54 – Temperature distribution on the 8 mm sample as a function of time elapsed after the start of sintering: a) 100 s; b) 280 s; c)700 and d) 1180s.

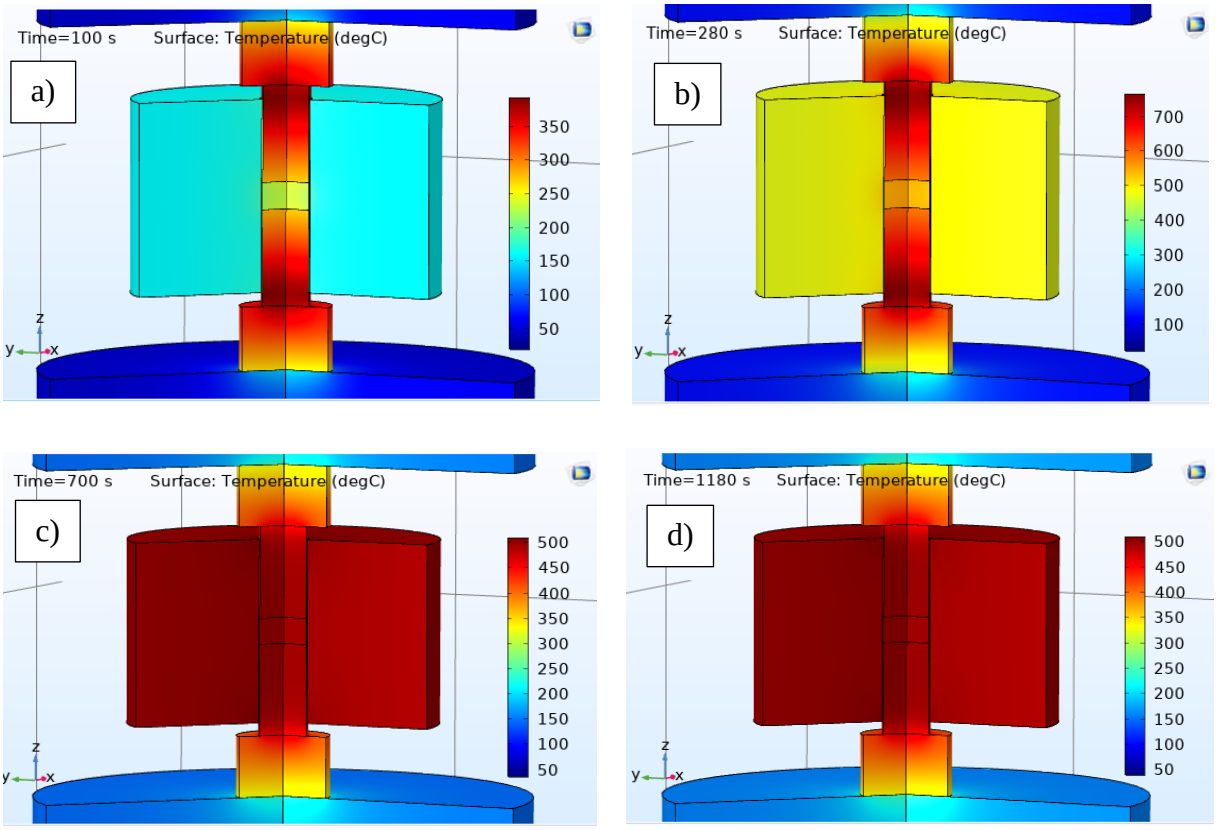

Source: The Author (2022)

4.8.3 Optimization of the SPS parameters using FEM

From the creep data (obtained from subsection 4.8.1), it was possible to model using the Finite Element Method (FEM) the densification of 20 mm diameter samples for 4 sets of sintering parameters fabricated by the SPS technique, obtaining the best configuration of pressure, plateau temperature and time. The densification curve of AA7075 for each set of parameters is presented in Figure 55, by using a heating rate of 100 °C/min for each case

(pattern of the machine used). The curve represented by a green continuous line (50 MPa, 500 °C, 15 min) had the lowest relative densification (97.78%). As it is possible to notice in Figure 55, the best sintering route is the one represented by the red dashed line, which leads to the highest densification (99.67%). This curve was obtained by using the parameters: 100 MPa, 550 °C, 15 min. Therefore, those parameters were applied experimentally and the sintered sample showed a relative density of 99.3% (Table 12), which is very close to what was obtained in the simulation.

Figure 55 – Densification curves of AA7075 obtained by FE simulation using 4 sets of sintering parameters

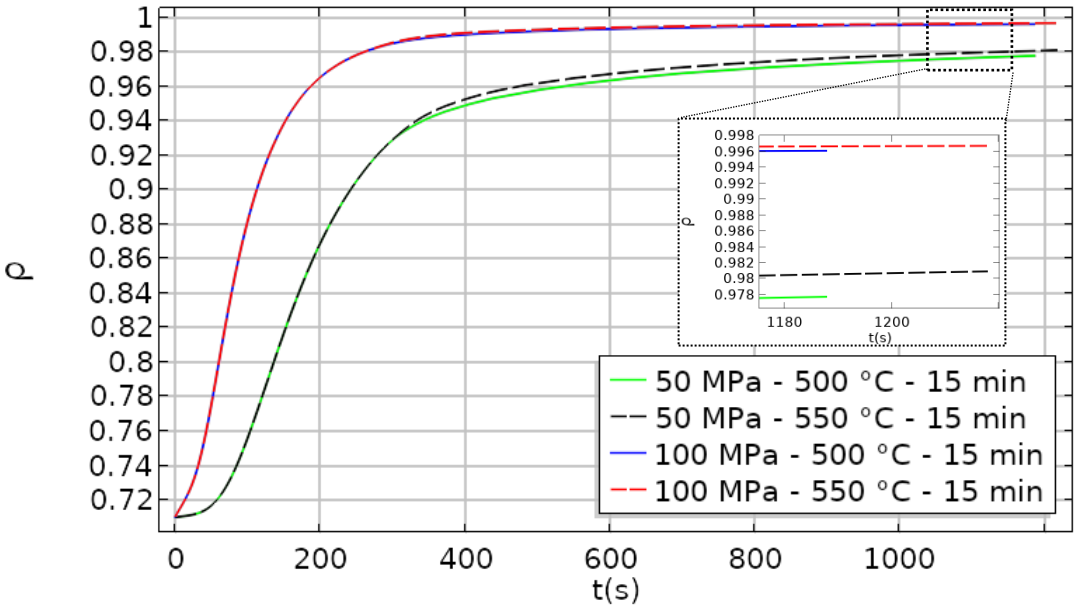

Source: The Author (2022)

The relative density and grain size representing the predicted microstructure of the 20 mm diameter SPSed sample using the optimized parameters are presented in Figure 45. In Figure 56(a) it can be seen that the relative density of sample AA7075 obtained by FEM simulation for the parameters 100 MPa, 550 °C and 15 min is quite homogeneous, with a variation very close to zero, which is expected for a conductive sample sintered by SPS. The Figure 56(b) shows the grain size at the end of the SPS cycle. The initial grain size is 33 µm, in the simulation it was obtained that at the end of the cycle the average size becomes approximately 34 µm, being practically equal throughout the sample. This value is in agreement with the experimentally obtained result (SOARES *et al.*, 2021) and induces an activation energy for grain growth Q_G = 61kJ/mol. For pure aluminum, the Q_G value is about 50 kJ/mol (OLEVSKY *et al.*, 2012), which suggests that the elements added to aluminum to form the AA7075 alloy slightly increase the value of this activation energy.

Figure 56 – Microstructure prediction of the 20 mm diameter SPSed sample with the optimized parameters: (a) relative density; (b) grain size.

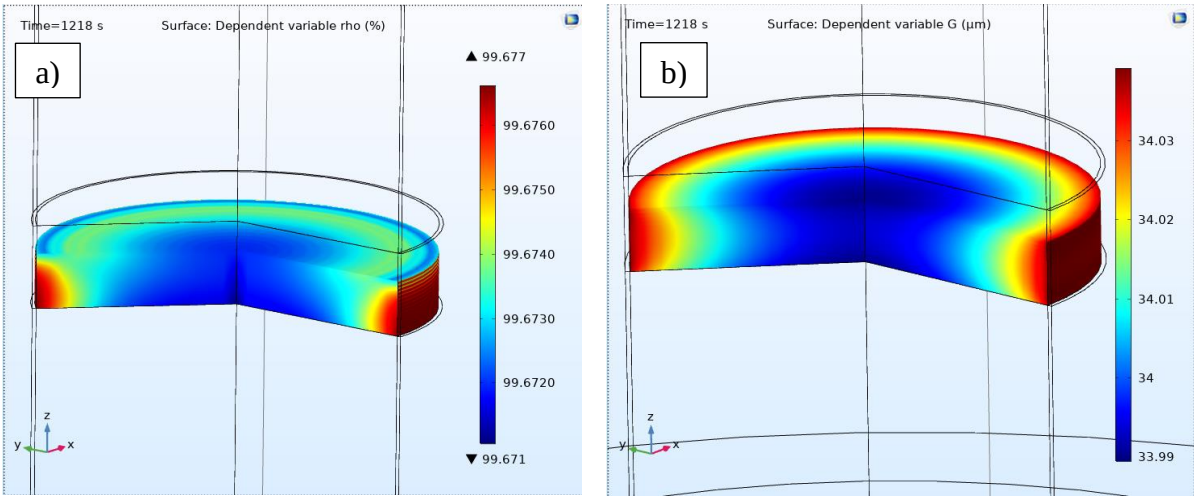

Source: The Author (2022)

The Figure 57 shows the evolution of the average grain size according to the sintering time. Simulation results show that grain growth starts at about 250 s after the start of the cycle, when the sample reaches about 450 °C.

Figure 57 – Average grain size as a function of sintering time

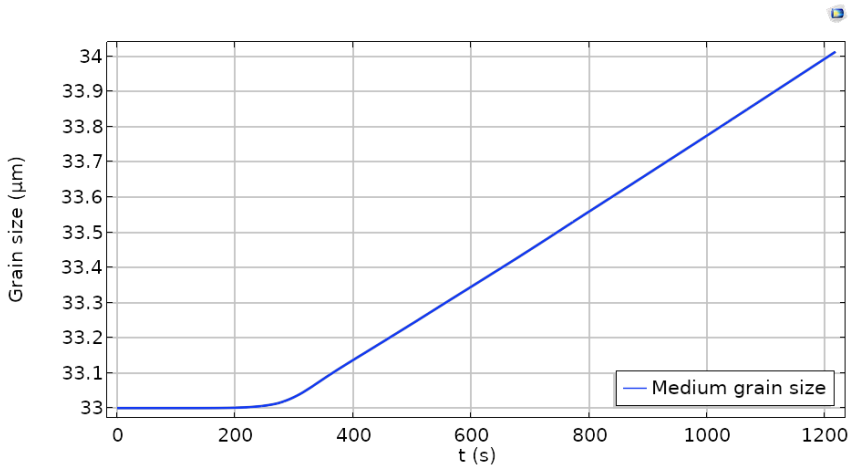

Source: The Author (2022)

The homogeneity of both density and grain size throughout the sample can be explained by the temperature distribution throughout the process. Figure 58 (a) shows the temperature field during heating at 100s, while Figure 58 (b) shows the temperature field at the beginning of the plateau (288s) and Figure 58 (c) shows the temperature field at the end of the SPS cycle (1218s). In all three cases it is possible to see that the temperature is homogeneous.

Figure 58 – Distribution of the temperature in the sample and the SPS equipment during SPS sintering: (a) at 100s, (b) at 288s, (c) at 1218s

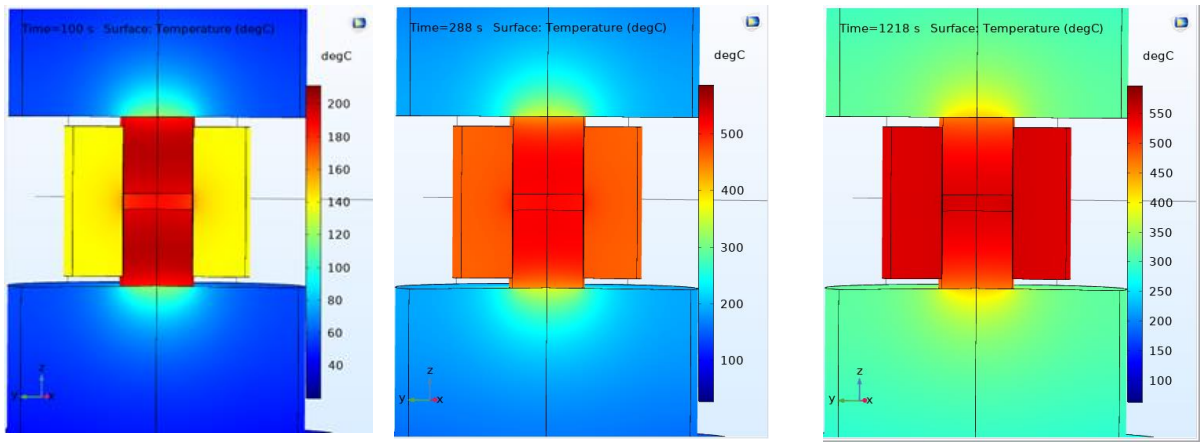

(a) (b) (c)

Source: The Author (2022)

The use of the finite element method (FEM), through the COMSOL Multiphysics software, proved to be a good option to reduce the number of experiments and material loss, since the results obtained by this method are very close to the experimental ones. Thus, it can be seen that the FEM is a good predictive tool to estimate the final properties of the sample as a function of the SPS parameters used.

5 CONCLUSION

EAFD-AA7075 composites with different EAFD content (5, 10 and 15 wt.%) and two particle sizes (noted G1 and G2) were produced by Spark Plasma Sintering - SPS (550 °C, 100 MPa, 30 min). The samples were almost or fully dense (97-100%). An electrothermal-mechanical-microstructural numerical model based on the Finite Element Method was developed that helped to define the best sintering route and able to predict the microstructural characteristics of the sample (density, grain size and porosity) as a function of the parameters used. According to the results obtained, the following conclusions can be drawn:

- From particle-size analysis, it was found that the average particle size of G1 - EAFD (<53μm) and G2 - EAFD (53-75 μm), is 13.9 μm and 63.1 μm, respectively. The XRD patterns reveal the presence of ZnO and Fe_3O_4 and/or $ZnFe_2O_4$ as major compounds for both the G1 and G2 EAFD powders.
- For both EAFD size ranges (G1 and G2), the Vickers microhardness considerably increases upon the increase in EAFD content. Thus, 15 wt.% G1/AA7075 and 15 wt.% G2/AA7075 composites have a hardness 55 and 40% higher than AA7075, respectively. The XRD analysis showed that no reaction took place between EAFD and the AA7075 matrix during sintering.
- The morphology of powders is retained in the bulk samples, with EAFD particles dispersed among AA7075 micrometric lamellar grains. Low porosity is observed along AA7075 grains that exhibit good cohesion.
- The creep parameters of the aluminum alloy AA7075 were determined from the experimental data provided by the SPS machine. The activation energy Q of the AA7075 alloy obtained was 29.5 kJ/mol and the A0 factor was 7.98e-28 s-1. The power law fluence exponent n was 4.
- From the numerical model developed, the best sintering route was obtained by using the parameters: 100 MPa, 550 °C, 15 min, predicting a densification of 99.67%. Therefore, these parameters were applied experimentally and the sintered sample showed a relative density of 99.3%, which is very close to what was obtained in the simulation, showing that the model is adequate.

6 SUGGESTIONS FOR FUTURE RESEARCH

From the present work, many topics can be further explored in order to advance in the development of new materials from SPS technique. Some of them are suggested below:

- Testing the influence of other reinforcements on the mechanical and microstructural properties of the AA7075 matrix or other aluminum alloys;

- Application of other milling times and/or other type of milling (such as cryomilling) in the production of the composites;

- Modeling and development of samples with complex geometries;

- Optimization of the SPS process using different optimization methods.

REFERENCES

ABDOLI, H.; ASGHARZADEH, H.; SALAHI, E. Sintering behavior of Al-AlN-nanostructured composite powder synthesized by high-energy ball milling. **Journal of Alloys and Compounds**, v. 473, n. 1–2, p. 116–122, 2009.

ABOUAF, M.; CHENOT, J. L.; RAISSON, G.; BAUDUIN, P. Finite element simulation of hot isostatic pressing of metal powders. **International Journal for Numerical Methods in Engineering**, v. 25, n. 1, p. 191–212, 1988.

ADEOSUN, S. O.; AKPAN, E. I.; SEKUNOWO, O. I.; AYOOLA, W. A.; BALOGUN, S. A. Mechanical Characteristics of 6063 Aluminum-Steel Dust Composite. **Mechanical Engineering**, v. 2012, p. 9, 2012.

ALANEME, K. K.; SANUSI, K. O. Microstructural characteristics, mechanical and wear behaviour of aluminium matrix hybrid composites reinforced with alumina, rice husk ash and graphite. **Engineering Science and Technology, an International Journal**, v. 18, n. 3, p. 416–422, 2015. Disponível em: <http://dx.doi.org/10.1016/j.jestch.2015.02.003>.

Alcoa Brazil. Available online: Disponível em: <https://www.alcoa.com/brasil/pt/default.asp>. Acesso em: 5 jun. 2019.

ALSHEYAB, M. A. T.; KHEDAYWI, T. S. Effect of electric arc furnace dust (EAFD) on properties of asphalt cement mixture. **Resources, Conservation and Recycling**, v. 70, p. 38–43, 2013.

AMAN, Y.; GARNIER, V.; DJURADO, E. Spark plasma sintering kinetics of pure α-alumina. **Journal of the American Ceramic Society**, v. 94, n. 9, p. 2825–2833, 2011.

ANSELMI-TAMBURINI, U.; GENNARI, S.; GARAY, J. E.; MUNIR, Z. A. Fundamental investigations on the spark plasma sintering/synthesis process. **Materials Science and Engineering A**, v. 407, n. 1–2, p. 24–30, 2005.

ARAÚJO, J. A.; SCHALCH, V. Recycling of electric arc furnace (EAF) dust for use in steel making process. **Journal of Materials Research and Technology**, v. 3, n. 3, p. 274–279, 2014.

ARNAUD, C.; MANIÈRE, C.; CHEVALLIER, G.; ESTOURNÈS, C.; MAINGUY, R.; LECOUTURIER, F.; MESGUICH, D.; WEIBEL, A.; DURAND, L.; LAURENT, C. Dog-bone copper specimens prepared by one-step spark plasma sintering. **Journal of Materials Science**, v. 50, n. 22, p. 7364–7373, 2015.

ASSOCIAÇÃO BRASILEIRA DE NORMAS TÉCNICAS (ABNT). **NBR 10004: Resíduos sólidos – classificação**. Rio de Janeiro: ABNT, 2004.

ASTRÖM, K. J.; HÄGGLUND, T. **Control PID avanzado**. Madrid: Pearson, 2009. 488 p.

AYE, S. W. H.; LWIN, K. T.; WAING, W.; KHINE, K. The Effect of Ageing Treatment of Aluminum Alloys for Fuselage Structure-Light Aircraft. **Engineering and Technology**, v. 2, n. 10, p. 576–579, 2008. Disponível em: <http://waset.org/publications/13023>.

BAKKAR, A. Recycling of electric arc furnace dust through dissolution in deep eutectic ionic liquids and electrowinning. **Journal of Hazardous Materials**, v. 280, p. 191–199, 2014.

BALAJI, V.; SATEESH, N.; HUSSAIN, M. M. Manufacture of Aluminium Metal Matrix Composite (Al7075-SiC) by Stir Casting Technique. **Materials Today: Proceedings**, v. 2, n. 4–5, p. 3403–3408, 2015.

BARADESWARAN, A.; ELAYA PERUMAL, A. Study on mechanical and wear properties of Al 7075/Al2O 3/graphite hybrid composites. **Composites Part B: Engineering**, v. 56, p. 464–471, 2014. Disponível em: <http://dx.doi.org/10.1016/j.compositesb.2013.08.013>.

BARRENECHE, C.; NAVARRO, M. E.; NIUBÓ, M.; CABEZA, L. F.; FERNÁNDEZ, A. I. Use of PCM-polymer composite dense sheet including EAFD in constructive systems. **Energy and Buildings**, v. 68, n. PARTA, p. 1–6, 2014.

BERA, S.; CHOWDHURY, S. G.; ESTRIN, Y.; MANNA, I. Mechanical properties of Al7075 alloy with nano-ceramic oxide dispersion synthesized by mechanical milling and consolidated by equal channel angular pressing. **Journal of Alloys and Compounds**, v. 548, p. 257–265, 2013.

CAGLIOTI, G.; PAOLETTI, A.; RICCI, F. P. Choice of collimators for a crystal spectrometer for neutron diffraction. **Nuclear Instruments**, v. 3, n. 4, p. 223–228, 1958.

CANAKCI, A.; VAROL, T. Microstructure and properties of AA7075/Al-SiC composites fabricated using powder metallurgy and hot pressing. **Powder Technology**, v. 268, p. 72–79, 2014.

CERRI, E.; EVANGELISTA, E. Metallography of Aluminium alloys. **Talat**, p. 20, 1999.

CIUCCIO, M. T. P. **Estudo de tendências e oportunidades no desenvolvimento sustentável para a reciclagem de veículos e seus materiais**. São Carlos: UFSCar, 2004. 191 p.

COMSOL. **COMSOL Multiphysics - Version 5.4: Reference Manual**2018.

COURTNEY, T. H. **Mechanical behavior of materiasl**. 2. ed. Long Grove: Waveland Press, 2005.

CREMER, G. D. **Powder Metallurgy**. US Pat: 2 355 954, 1944.

DAYANI, D.; SHOKUHFAR, A.; VAEZI, M. R.; REZAEI, S. R. J.; HOSSEINPOUR, S. Structural and mechanical evaluation of a nanocrystalline A1–5 wt %si alloy produced by mechanical alloying. **Metals**, v. 7, n. 9, 2017.

ENVIRONMENTAL PROTECTION AGENCY. **European waste catalogue and hazardous waste list**. Wexford: EPA, 2002. 1–49 p.

ESTRADA-RUIZ, R. H.; FLORES-CAMPOS, R.; TREVIÑO-RODRÍGUEZ, G. A.; HERRERA-RAMÍREZ, J. M.; MARTÍNEZ-SÁNCHEZ, R. Wear resistance analysis of the aluminum 7075 alloy and the nanostructured aluminum 7075 - silver nanoparticles composites. **Journal of Mining and Metallurgy, Section B: Metallurgy**, v. 52, n. 00, p. 11–11, 2016. Disponível em: <http://www.doiserbia.nb.rs/Article.aspx?ID=1450-53391600011E>.

FLORES-VÉLEZ, L. M.; CHÁVEZ, J.; HERNÁNDEZ, L.; DOMÍNGUEZ, O. Characterization and properties of aluminum composite materials prepared by powder metallurgy techniques using ceramic solid wastes. **Materials and Manufacturing Processes**, v. 16, n. 1, p. 1–16, 2001.

GAMEA, E. G.; ANWAR, A.; EZZAT, A. A.; EL-RAFEY, M. E. Utilization of electric arc furnace dust as a filler for unsaturated polyester resin. **Process Safety and Environmental Protection**, v. 159, p. 1194–1202, 1 mar. 2022.

GERMAN, R. M. **Sintering Theory and Practice**. New York: Wiley, 1996. 568 p.

GÖKÇE, A.; FINDIK, F.; KURT, A. O. Microstructural examination and properties of premixed Al-Cu-Mg powder metallurgy alloy. **Materials Characterization**, v. 62, n. 7, p. 730–735, 2011.

GRASSO, S.; SAKKA, Y.; MAIZZA, G. Electric current activated/assisted sintering (ECAS): A review of patents 1906-2008. **Science and Technology of Advanced Materials**, v. 10, n. 5, 2009.

GRAULIS, S.; CHATEIGNER, D.; DOWNS, R. T.; YOKOCHI, A. F. T.; QUIRÓS, M.; LUTTEROTTI, L.; MANAKOVA, E.; BUTKUS, J.; MOECK, P.; LE BAIL, A. Crystallography Open Database - An open-access collection of crystal structures. **Journal of Applied Crystallography**, v. 42, n. 4, p. 726–729, 2009.

GUÉZENNEC, A. G.; HUBER, J. C.; PATISSON, F.; SESSIECQ, P.; BIRAT, J. P.; ABLITZER, D. Dust formation in Electric Arc Furnace: Birth of the particles. **Powder Technology**, v. 157, n. 1–3, p. 2–11, 2005.

GUILLON, O.; GONZALEZ-JULIAN, J.; DARGATZ, B.; KESSEL, T.; SCHIERNING, G.; RÄTHEL, J.; HERRMANN, M. Field-assisted sintering technology/spark plasma sintering:

Mechanisms, materials, and technology developments. **Advanced Engineering Materials**, v. 16, n. 7, p. 830–849, 2014.

HAMUYUNI, J.; HALLI, P.; TESFAYE, F.; LEIKOLA, M.; LUNDSTRÖM, M. A sustainable methodology for recycling electric arc furnace dust. Em: Minerals, Metals and Materials Series, 2018, [...]. Springer International Publishing, 2018. v. Part F6, p. 233–240.

HE, M.; ZHANG, Z.; MAO, W.; LI, B.; BAI, Y.; XU, J. Numerical and experimental study on melt treatment for large-volume 7075 alloy by a modified annular electromagnetic stirring. **Materials**, v. 12, n. 5, 2019.

HUAIWEI, Z.; XIN, H. An overview for the utilization of wastes from stainless steel industries. **Resources, Conservation and Recycling**, v. 55, n. 8, p. 745–754, 2011.

HUANG, Z. W.; LORETTO, M. H.; SMALLMAN, R. E.; WHITE, J. The Mechanism of Nucleation and Precipitation in 7075-0.7 Li Alloy. v. 42, n. 2, p. 549–559, 1994.

HULBERT, D. M.; ANDERS, A.; DUDINA, D. v.; ANDERSSON, J.; JIANG, D.; UNUVAR, C.; ANSELMI-TAMBURINI, U.; LAVERNIA, E. J.; MUKHERJEE, A. K. The absence of plasma in “spark plasma sintering”. **Journal of Applied Physics**, v. 104, n. 3, p. 0–7, 2008.

HUNGRÍA, T.; GALY, J.; CASTRO, A. Spark plasma sintering as a useful technique to the nanostructuration of piezo-ferroelectric materials. **Advanced Engineering Materials**, v. 11, n. 8, p. 615–631, 2009.

HUO, S. H.; QIAN, M.; SCHAFFER, G. B.; CROSSIN, E. **Aluminium powder metallurgy**. [s.l.] Woodhead Publishing Limited, 2010. 655–701 p.

IAB (INSTITUTO AÇO BRASIL). **Relatório de Sustentabilidade**. Disponível em: <https://www.acobrasil.org.br/relatoriodesustentabilidade/>. Acesso em: 11 jul. 2022.

INOUE, K. **Apparatus for Electrically Sintering Discrete Bodies**. US Pat: 3 250 892, 1966a.

INOUE, K. **Electric-Discharge Sintering**. US Pat: 3 241 956, 1966b.

ISADARE, A. D.; AREMO, B.; ADEOYE, M. O.; OLAWALE, O. J.; SHITTU, M. D. Effect of heat treatment on some mechanical properties of 7075 aluminium alloy. **Materials Research**, v. 16, n. 1, p. 190–194, 2012.

JHA, A. K.; SREEKUMAR, K. Metallurgical studies on cracked Al-5.5Zn-2.5Mg-1.5Cu aluminum alloy injector disc of turbine rotor. **Journal of Failure Analysis and Prevention**, v. 8, n. 4, p. 327–332, 2008.

KALKANLI, A.; YILMAZ, S. Synthesis and characterization of aluminum alloy 7075 reinforced with silicon carbide particulates. **Materials and Design**, v. 29, n. 4, p. 775–780, 2008.

KARUNANITHI, R.; GHOSH, K. S.; BERA, S. Effect of dispersoid size and volume fraction on aging behavior and mechanical properties of TiO2-dispersed AA7075 alloy composites. **Metallurgical and Materials Transactions A: Physical Metallurgy and Materials Science**, v. 45, n. 9, p. 4062–4072, 2014.

KUMAR, P. V.; REDDY, G. M.; RAO, K. S. Microstructure, mechanical and corrosion behavior of high strength AA7075 aluminium alloy friction stir welds – Effect of post weld heat treatment. **Defence Technology**, v. 11, n. 4, p. 362–369, 2015. Disponível em: <http://dx.doi.org/10.1016/j.dt.2015.04.003>.

LANGER, J.; HOFFMANN, M. J.; GUILLON, O. Direct comparison between hot pressing and electric field-assisted sintering of submicron alumina. **Acta Materialia**, v. 57, n. 18, p. 5454–5465, 2009.

LEDESMA, E. F.; JIMÉNEZ, J. R.; AYUSO, J.; FERNÁNDEZ, J. M.; DE BRITO, J. Experimental study of the mechanical stabilization of electric arc furnace dust using fluid cement mortars. **Journal of Hazardous Materials**, v. 326, p. 26–35, 2017.

LI, W.; OLEVSKY, E. A.; MCKITTRICK, J.; MAXIMENKO, A. L.; GERMAN, R. M. Densification mechanisms of spark plasma sintering: Multi-step pressure dilatometry. **Journal of Materials Science**, v. 47, n. 20, p. 7036–7046, 2012.

LIU, Y.; CAI, S.; XU, F.; WANG, Y.; DAI, L. Enhancing strength without compromising ductility in copper by combining extrusion machining and heat treatment. **Journal of Materials Processing Technology**, v. 267, n. December 2018, p. 52–60, 2019.

LIU, Z. F.; ZHANG, Z. H.; LU, J. F.; KORZNIKOV, A. V.; KORZNIKOVA, E.; WANG, F. C. Effect of sintering temperature on microstructures and mechanical properties of spark plasma sintered nanocrystalline aluminum. **Materials and Design**, v. 64, p. 625–630, 2014.

MA, K.; WEN, H.; HU, T.; TOPPING, T. D.; ISHEIM, D.; SEIDMAN, D. N.; LAVERNIA, E. J.; SCHOENUNG, J. M. Mechanical behavior and strengthening mechanisms in ultrafine grain precipitation-strengthened aluminum alloy. **Acta Materialia**, v. 62, n. 1, p. 141–155, 2014.

MANIÈRE, C. **Spark Plasma Sintering : couplage entre les approches Modélisation, Instrumentation et Matériaux**. 2015. 2015. Disponível em: <https://tel.archives-ouvertes.fr/tel-01362029/document>.

MANIÈRE, C.; DURAND, L.; BRISSON, E.; DESPLATS, H.; CARRÉ, P.; ROGEON, P.; ESTOURNÈS, C. Contact resistances in spark plasma sintering: From in-situ and ex-situ determinations to an extended model for the scale up of the process. **Journal of the European Ceramic Society**, v. 37, n. 4, p. 1593–1605, 2017a. Disponível em: <http://dx.doi.org/10.1016/j.jeurceramsoc.2016.12.010>.

MANIÈRE, C.; DURAND, L.; CHEVALLIER, G.; ESTOURNÈS, C. A spark plasma sintering densification modeling approach: from polymer, metals to ceramics. **Journal of Materials Science**, v. 53, n. 10, p. 7869–7876, 2018.

MANIÈRE, C.; DURAND, L.; WEIBEL, A.; CHEVALLIER, G.; ESTOURNÈS, C. A sacrificial material approach for spark plasma sintering of complex shapes. **Scripta Materialia**, v. 124, p. 126–128, 2016a. Disponível em: <http://dx.doi.org/10.1016/j.scriptamat.2016.07.006>.

MANIÈRE, C.; DURAND, L.; WEIBEL, A.; ESTOURNÈS, C. Spark-plasma-sintering and finite element method: From the identification of the sintering parameters of a submicronic α-alumina powder to the development of complex shapes. **Acta Materialia**, v. 102, p. 169–175, 2016b.

MANIÈRE, C.; KUS, U.; DURAND, L.; MAINGUY, R.; HUEZ, J.; DELAGNES, D.; ESTOURNÈS, C. Identification of the Norton-Green Compaction Model for the Prediction of the Ti–6Al–4V Densification During the Spark Plasma Sintering Process. **Advanced Engineering Materials**, v. 18, n. 10, p. 1720–1727, 2016c.

MANIÈRE, C.; NIGITO, E.; DURAND, L.; WEIBEL, A.; BEYNET, Y.; ESTOURNÈS, C. Spark plasma sintering and complex shapes: The deformed interfaces approach. **Powder Technology**, v. 320, p. 340–345, out. 2017b. Disponível em: <https://linkinghub.elsevier.com/retrieve/pii/S0032591017305880>.

MANIÈRE, C.; PAVIA, A.; DURAND, L.; CHEVALLIER, G.; AFANGA, K.; ESTOURNÈS, C. Finite-element modeling of the electro-thermal contacts in the spark plasma sintering process. **Journal of the European Ceramic Society**, v. 36, n. 3, p. 741–748, fev. 2016d. Disponível em: <http://dx.doi.org/10.1016/j.jeurceramsoc.2015.10.033>.

MANIERE, C.; PAVIA, A.; DURAND, L.; CHEVALLIER, G.; BLEY, V.; AFANGA, K.; PEIGNEY, A.; ESTOURNÈS, C. Pulse analysis and electric contact measurements in spark plasma sintering. **Electric Power Systems Research**, v. 127, p. 307–313, 2015. Disponível em: <http://dx.doi.org/10.1016/j.epsr.2015.06.009>.

MANIÈRE, C.; TORRESANI, E.; OLEVSKY, E. A. Simultaneous spark plasma sintering of multiple complex shapes. **Materials**, v. 12, n. 2, p. 1–14, 2019.

MARDER, R.; ESTOURNÈS, C.; CHEVALLIER, G.; CHAIM, R. Plasma in spark plasma sintering of ceramic particle compacts. **Scripta Materialia**, v. 82, p. 57–60, 2014a.

MARDER, R.; ESTOURNÈS, C.; CHEVALLIER, G.; CHAIM, R. Spark and plasma in spark plasma sintering of rigid ceramic nanoparticles: A model system of YAG. **Journal of the European Ceramic Society**, v. 35, n. 1, p. 211–218, 2015. Disponível em: <http://dx.doi.org/10.1016/j.jeurceramsoc.2014.08.001>.

MARDER, R.; ESTOURNÈS, C.; CHEVALLIER, G.; KALABUKHOV, S.; CHAIM, R. Spark plasma sintering of ductile ceramic particles: Study of LiF. **Journal of Materials Science**, v. 49, n. 15, p. 5237–5245, 2014b.

MARTINS, D.; GRUMBACH, F.; MANIÈRE, C.; SALLOT, P.; MOCELLIN, K.; BELLET, M.; ESTOURNÈS, C. In-situ creep law determination for modeling Spark Plasma Sintering of TiAl 48-2-2 powder. **Intermetallics**, v. 86, p. 147–155, 2017.

METZ, J. C.; MACIEL, E. F.; GARBIN, M.; MODOLO, R. C. E.; MORAES, C. A. M.; GOMES, L. B.; BREHM, F. A. Influence of electric arc furnace dust and lime kiln waste in Portland cement hydration. **Ambiente Construído**, v. 20, n. 4, p. 225–241, dez. 2020.

MISHRA, S. K.; ROY, H.; LOHAR, A. K.; SAMANTA, S. K.; TIWARI, S.; DUTTA, K. A comparative assessment of crystallite size and lattice strain in differently cast A356 aluminium alloy. **IOP Conference Series: Materials Science and Engineering**, v. 75, n. 1, 2015.

MOLNÁROVÁ, O.; MÁLEK, P.; VESELÝ, J.; MINÁRIK, P.; LUKÁČ, F.; CHRÁSKA, T.; NOVÁK, P.; PRŮŠA, F. The influence of milling and spark plasma sintering on the microstructure and properties of the Al7075 alloy. **Materials**, v. 11, n. 4, 2018.

MUHD, F. N.; AMIR, F.; MOHAMED, M. A. W.; SHAFIQ, N.; MALKAWI, A. B. Utilization of eafd in concrete composite. Em: Materials Science Forum, 2017, [...]. Trans Tech Publications Ltd, 2017. v. 894 MSF, p. 72–75.

MUNIR, Z. A.; QUACH, D. v.; OHYANAGI, M. Electric current activation of sintering: A review of the pulsed electric current sintering process. **Journal of the American Ceramic Society**, v. 94, n. 1, p. 1–19, 2011.

MUÑOZ, S.; ANSELMI-TAMBURINI, U. Temperature and stress fields evolution during spark plasma sintering processes. **Journal of Materials Science**, v. 45, n. 23, p. 6528–6539, 2010.

NIUBÓ, M.; FERNÁNDEZ, A. I.; CHIMENOS, J. M.; HAURIE, L. A possible recycling method for high grade steels EAFD in polymer composites. **Journal of Hazardous Materials**, v. 171, n. 1–3, p. 1139–1144, 15 nov. 2009.

NORIMAT. **NORIMAT**. Disponível em: <https://www.norimat.com/en/>. Acesso em: 15 ago. 2022.

OLEVSKY, E. A. Theory of sintering: From discrete to continuum. **Materials Science and Engineering R: Reports**, v. 23, n. 2, p. 41–100, 1998.

OLEVSKY, E. A.; GARCIA-CARDONA, C.; BRADBURY, W. L.; HAINES, C. D.; MARTIN, D. G.; KAPOOR, D. Fundamental aspects of spark plasma sintering: II. Finite element analysis of scalability. **Journal of the American Ceramic Society**, v. 95, n. 8, p. 2414–2422, 2012.

OLEVSKY, E. A.; KANDUKURI, S.; FROYEN, L. Consolidation enhancement in spark-plasma sintering: Impact of high heating rates. **Journal of Applied Physics**, v. 102, n. 11, 2007.

OLEVSKY, E. A.; KUSHNAREV, B.; MAXIMENKO, A.; TIKARE, V.; BRAGINSKY, M. Modelling of anisotropic sintering in crystalline ceramics. **Philosophical Magazine**, v. 85, n. 19, p. 2123–2146, 2005.

OLEVSKY, E. A.; TIKARE, V.; GARINO, T. Multi-scale study of sintering: A review. **Journal of the American Ceramic Society**, v. 89, n. 6, p. 1914–1922, 2006.

OLEVSKY, E.; FROYEN, L. Constitutive modeling of spark-plasma sintering of conductive materials. **Scripta Materialia**, v. 55, n. 12, p. 1175–1178, 2006.

OLIVEIRA ALVES, E.; ARAÚJO AMARO, D. R.; DE OLIVEIRA SILVA, E. C.; DE ARAÚJO FILHO, O. O.; BEZERRA ALVES, K. G. Study on effect of EAFD particulate reinforcement in AA7075 Aluminum matrix composites. **Materials Research-Ibero-american Journal of Materials**, v. 21, n. 6, p. e20170779, 2018. Disponível em: <http://dx.doi.org/10.1590/1980-5373-mr-2017-0779>.

ORRÙ, R.; LICHERI, R.; LOCCI, A. M.; CINCOTTI, A.; CAO, G. Consolidation/synthesis of materials by electric current activated/assisted sintering. **Materials Science and Engineering R: Reports**, v. 63, n. 4–6, p. 127–287, 2009.

P. ROCABOIS; J.C. HUBER; E. LECTARD; F. PATISSON. Thermodynamic assessment of the oxide phase in the Fe–Zn–O system: application to the dust formation in EAF. (K. Hilpert, F. W. Froben, L. Singheiser) Em: Proceedings of the 10th International IUPAC Conference on High Temperature Materials Chemistry, 2000, Julich, Germany. [...]. Julich, Germany: 2000. p. 1–12.

PAVIA, A.; DURAND, L.; AJUSTRON, F.; BLEY, V.; CHEVALLIER, G.; PEIGNEY, A.; ESTOURNÈS, C. Electro-thermal measurements and finite element method simulations of a

spark plasma sintering device. **Journal of Materials Processing Technology**, v. 213, n. 8, p. 1327–1336, 2013. Disponível em: <http://dx.doi.org/10.1016/j.jmatprotec.2013.02.003>.

PRADEEP DEVANEYAN, S.; GANESH, R.; SENTHILVELAN, T. On the Mechanical Properties of Hybrid Aluminium 7075 Matrix Composite Material Reinforced with SiC and TiC Produced by Powder Metallurgy Method. **Indian Journal of Materials Science**, v. 2017, p. 1–6, 2017.

QUEUDET, H.; LEMONNIER, S.; BARRAUD, E.; GUYON, J.; GHANBAJA, J.; ALLAIN, N.; GAFFET, E. One-step consolidation and precipitation hardening of an ultrafine-grained Al-Zn-Mg alloy powder by Spark Plasma Sintering. **Materials Science and Engineering A**, v. 685, n. October 2016, p. 227–234, 2017.

RANA, H. G.; BADHEKA, V. J.; KUMAR, A. Fabrication of Al7075 / B_4C Surface Composite by Novel Friction Stir Processing (FSP) and Investigation on Wear Properties. **Procedia Technology**, v. 23, p. 519–528, 2016. Disponível em: <http://linkinghub.elsevier.com/retrieve/pii/S2212017316300597>.

RANA, J. K.; SIVAPRAHASAM, D.; SEETHARAMA RAJU, K.; SUBRAMANYA SARMA, V. Microstructure and mechanical properties of nanocrystalline high strength Al-Mg-Si (AA6061) alloy by high energy ball milling and spark plasma sintering. **Materials Science and Engineering A**, v. 527, n. 1–2, p. 292–296, 2009.

RAO, T. B. An Experimental Investigation on Mechanical and Wear Properties of Al7075/SiCp Composites: Effect of SiC Content and Particle Size. **Journal of Tribology**, v. 140, n. 3, p. 031601, 2017.

RAZAVI-TOUSI, S. S.; SZPUNAR, J. A. Effect of ball size on steady state of aluminum powder and efficiency of impacts during milling. **Powder Technology**, v. 284, p. 149–158, 2015.

RECKZIEGEL, V. N.; SCHNEIDER, I. A. H.; OSÓRIO, E.; LEMOS, L. Caracterização para o aproveitamento do resíduo de um triturador de sucata em uma usina siderúrgica. 2012.

SANTANACH, J. G.; WEIBEL, A.; ESTOURNS, C.; YANG, Q.; LAURENT, C.; PEIGNEY, A. Spark plasma sintering of alumina: Study of parameters, formal sintering analysis and hypotheses on the mechanism(s) involved in densification and grain growth. **Acta Materialia**, v. 59, n. 4, p. 1400–1408, 2011.

SCHWERTZ, M.; KATZ, A.; SORREL, E.; LEMONNIER, S.; BARRAUD, E.; CARRADÒ, A.; D'ASTORG, S.; LERICHE, A.; NARDIN, M.; VALLAT, M. F.; KOSIOR, F. Coupled Electro-Thermo-Mechanical Finite Element Modeling of the Spark Plasma Sintering

Technique. **Metallurgical and Materials Transactions B: Process Metallurgy and Materials Processing Science**, v. 47, n. 2, p. 1263–1273, 2016.

SHEN, Q.; WU, C.; LUO, G.; FANG, P.; LI, C.; WANG, Y.; ZHANG, L. Microstructure and mechanical properties of Al-7075/B_4C composites fabricated by plasma activated sintering. **Journal of Alloys and Compounds**, v. 588, p. 265–270, 2014. Disponível em: <http://dx.doi.org/10.1016/j.jallcom.2013.11.089>.

SINTERMAT. **SINTERMAT**. Disponível em: <https://sinter-mat.com/en/homepage/>. Acesso em: 15 ago. 2022.

SOARES, E.; BOUCHONNEAU, N.; ALVES, E.; ALVES, K.; FILHO, O. A.; MESGUICH, D.; CHEVALLIER, G.; LAURENT, C.; ESTOURNÈS, C. Microstructure and mechanical properties of AA7075 aluminum alloy fabricated by spark plasma sintering (SPS). **Materials**, v. 14, n. 2, p. 1–11, 2021.

SOUZA, C. A. C.; MACHADO, A. T.; LIMA, L. R. P. A.; CARDOSO, R. J. C. Stabilization of electric-arc furnace dust in concrete. **Materials Research**, v. 13, n. 4, p. 513–519, 2010.

STATHOPOULOS, V. N.; PAPANDREOU, A.; KANELLOPOULOU, D.; STOURNARAS, C. J. Structural ceramics containing electric arc furnace dust. **Journal of Hazardous Materials**, v. 262, p. 91–99, 2013a.

STATHOPOULOS, V. N.; PAPANDREOU, A.; KANELLOPOULOU, D.; STOURNARAS, C. J. Structural ceramics containing electric arc furnace dust. **Journal of Hazardous Materials**, v. 262, p. 91–99, 15 nov. 2013b.

SURYANARAYANA, C.; NORTON, M. G. **X-Ray Diffraction**. New York: Springer, 1998.

TANG, H.; WANG, L.; SUN, W.; HU, Y.; HAN, H.; ZHAI, J. Electric arc furnace dust as magnetic carrier particles for removal of micro-fine particles from suspensions. **Separation and Purification Technology**, v. 176, p. 220–230, 2017.

TAVOOSI, M.; ENAYATI, M. H.; KARIMZADEH, F. Softening behaviour of nanostructured Al-14 wt% Zn alloy during mechanical alloying. **Journal of Alloys and Compounds**, v. 464, n. 1–2, p. 107–110, 2008.

TAYLOR, G. F. **Apparatus for Making Hard Metal Compositions**. US Pat: 1 896 854, 1933.

THE ALUMINIUM ASSOCIATION. International Alloy Designations and Chemical Composition Limits for Wrought Aluminum and Wrought Aluminum Alloys With Support for On-line Access From: Aluminum Extruders Council Use of the Information. **The Aluminum Association, Arlington, Virginia**, n. Enero 2015, p. 31, 2015.

TOKITA, M. **Spark Plasma Sintering (SPS) Method, Systems, and Applications**. [s.l.] Elsevier Inc., 2013. 1149–1177 p.

TOKITA, M. Recent and future progress on advanced ceramics sintering by Spark Plasma Sintering. **Nanotechnologies in Russia**, v. 10, n. 3–4, p. 261–267, 2015.

TOOZANDEHJANI, M.; MATORI, K. A.; OSTOVAN, F.; AZIZ, S. A.; MAMAT, M. S. Effect of milling time on the microstructure, physical and mechanical properties of Al-Al2O3 nanocomposite synthesized by ball milling and powder metallurgy. **Materials**, v. 10, n. 11, 2017.

VALIEV, R. Z.; ESTRIN, Y.; HORITA, Z.; LANGDON, T. G.; ZEHETBAUER, M. J.; ZHU, Y. T. Fundamentals of superior properties in bulk NanoSPD materials. **Materials Research Letters**, v. 4, n. 1, p. 1–21, 2016.

VAN DER LAAN, A.; EPHERRE, R.; CHEVALLIER, G.; BEYNET, Y.; WEIBEL, A.; ESTOURNÈS, C. Fully coupled electrothermal and mechanical simulation of the production of complex shapes by spark plasma sintering. **Journal of the European Ceramic Society**, v. 41, n. 7, p. 4252–4263, 1 jul. 2021.

VANMEENSEL, K.; LAPTEV, A.; HENNICKE, J.; VLEUGELS, J.; VAN DER BIEST, O. Modelling of the temperature distribution during field assisted sintering. **Acta Materialia**, v. 53, n. 16, p. 4379–4388, 2005.

VEERAVALLI, R. R.; NALLU, R.; MOHAMMED MOULANA MOHIUDDIN, S.; RAO, V. R.; RAMANAIAH, N.; SARCAR, M. M. M.; VEERAVALLI, R. R.; NALLU, R.; MOHAMMED MOULANA MOHIUDDIN, S. Mechanical and tribological properties of AA7075-TiC metal matrix composites under heat treated (T6) and cast conditions. **Journal of Materials Research and Technology**, v. 5, n. 4, p. 377–383, 2016. Disponível em: <http://dx.doi.org/10.1016/j.jmrt.2016.03.011>.

VENKATESAN, K.; RAMANUJAM, R.; SHANBHAG, Vignesh. V.; YALAMOORI, Nitin. N.; REDDY, D. V. Preparation, Characterization and Machinability of Al7075-Al_2O_3 Matrix Composite Using Multi Layer Coated Carbide Insert. **Procedia Materials Science**, v. 5, p. 1819–1828, 2014. Disponível em: <http://linkinghub.elsevier.com/retrieve/pii/S2211812814008347>.

VERMA, R. K.; MAHESH, N. S.; ANWAR, M. I. Numerical analysis of powder compaction to obtain high relative density in ‘601AB’’ aluminum powder’. **SAS Technol.**, v. 11, n. 1, p. 79–84, 2012. Disponível em: <http://www.msruas.ac.in/pdf_files/sastechJournals/May2012/11.pdf>.

VOISIN, T.; MONCHOUX, J.-P.; COURET, A. Near-Net Shaping of Titanium-Aluminum Jet Engine Turbine Blades by SPS. *Em*: **Spark Plasma Sintering of Materials**. Cham: Springer International Publishing, 2019. p. 713–737.

WILLIAMSON, G. K.; HALL, W. H. X-ray line broadening from filed aluminium and wolfram. **Acta Metallurgica**, v. 1, n. 1, p. 22–31, 1953.

YAZDIAN, N.; KARIMZADEH, F.; TAVOOSI, M. Microstructural evolution of nanostructure 7075 aluminum alloy during isothermal annealing. **Journal of Alloys and Compounds**, v. 493, n. 1–2, p. 137–141, 2010. Disponível em: <http://dx.doi.org/10.1016/j.jallcom.2009.12.144>.

ZAVALIANGOS, A.; ZHANG, J.; KRAMMER, M.; GROZA, J. R. Temperature evolution during field activated sintering. **Materials Science and Engineering A**, v. 379, n. 1–2, p. 218–228, 2004.

ZHANG, Y.; JIN, S.; TRIMBY, P. W.; LIAO, X.; MURASHKIN, M. Y.; VALIEV, R. Z.; LIU, J.; CAIRNEY, J. M.; RINGER, S. P.; SHA, G. Dynamic precipitation, segregation and strengthening of an Al-Zn-Mg-Cu alloy (AA7075) processed by high-pressure torsion. **Acta Materialia**, v. 162, p. 19–32, 2019. Disponível em: <https://doi.org/10.1016/j.actamat.2018.09.060>.

ZHANG, Z. H.; LIU, Z. F.; LU, J. F.; SHEN, X. B.; WANG, F. C.; WANG, Y. D. The sintering mechanism in spark plasma sintering - Proof of the occurrence of spark discharge. **Scripta Materialia**, v. 81, p. 56–59, 2014.

ZHU, Y. T.; WU, X. L. Ductility and plasticity of nanostructured metals: differences and issues. **Materials Today Nano**, v. 2, n. September, p. 15–20, 2018.

ZIPPERIAN, D. C. **Metallographic Handbook**. 1. ed. Tucson: PACE Technologies, 2011. 344 p.

APPENDIX A – FIRST PUBLISHED ARTICLE

materials

MDPI

Article

Microstructure and Mechanical Properties of AA7075 Aluminum Alloy Fabricated by Spark Plasma Sintering (SPS)

Elder Soares [1], Nadège Bouchonneau [1], Elizeth Alves [1], Kleber Alves [1], Oscar Araújo Filho [1], David Mesguich [2], Geoffroy Chevallier [2], Christophe Laurent [2] and Claude Estournès [2,*]

[1] Mechanical Engineering Department, Federal University of Pernambuco (UFPE), Av. da Arquitetura, S/N, Recife, PE 50.740-550, Brazil; elder.soares52@gmail.com (E.S.); nadege.bouchonneau@gmail.com (N.B.); elizeth_oliveira@yahoo.com.br (E.A.); kleber.gbalves@ufpe.br (K.A.); oscaroaf98@hotmail.com (O.A.F.)

[2] CIRIMAT, Université de Toulouse, CNRS, Université Paul-Sabatier, 118 Route de Narbonne, 31062 Toulouse CEDEX 9, France; mesguich@chimie.ups-tlse.fr (D.M.); chevallier@chimie.ups-tlse.fr (G.C.); laurent@chimie.ups-tlse.fr (C.L.)

* Correspondence: estournes@chimie.ups-tlse.fr; Tel.: +33-(0)5-6155-6109

Abstract: AA7075 aluminum alloy is widely used for several high-technology applications for its high mechanical strength to weight ratio but is still the subject of several studies seeking a further increase in its mechanical properties. A commercial powder is used, either as-received or after ball-milling. Dense AA7075 samples are prepared in one step by Spark Plasma Sintering, at 550 °C with a holding time of 15 min and a uniaxial pressure of 100 MPa. No additional heat treatment is performed. Laser granulometry, X-ray diffraction and optical- and scanning electron microscopy show that both grain size and morphology are preserved in the dense samples, due to the relatively low temperature and short sintering time used. The samples prepared using the ball-milled powder exhibit both higher Vickers microhardness and transverse fracture strength values than those prepared using the raw powder, reflecting the finer microstructure.

Keywords: Spark Plasma Sintering (SPS); aluminum alloy; microstructure; mechanical properties

Citation: Soares, E.; Bouchonneau, N.; Alves, E.; Alves, K.; Araújo Filho, O.; Mesguich, D.; Chevallier, G.; Laurent, C.; Estournès, C. Microstructure and Mechanical Properties of AA7075 Aluminum Alloy Fabricated by Spark Plasma Sintering (SPS). *Materials* **2021**, *14*, 430. https://doi.org/10.3390/ma14020430

Received: 22 December 2020
Accepted: 12 January 2021
Published: 16 January 2021

1. Introduction

Powder metallurgy (PM) technology has been of interest to several industrial sectors for decades. The necessity for metallic materials with improved mechanical and physical properties to satisfy the current requirements has resulted in development of new manufacturing processes [1,2]. The AA7075 aluminum alloy is widely used in the aeronautical, marine, automotive and defense industries for its high mechanical strength to weight ratio [3,4], but is still the subject of several studies seeking to further improve its mechanical properties [5].

The manufacture of aluminum alloy parts commonly uses powder metallurgy processes, such as cold isostatic pressing (CIP), hot isostatic pressing (HIP), hot pressing (HP), hot extrusion and hot rolling. These are competitive with respect to casting and extrusion, but it involves the degassing of the powder for several hours and several more hours (1–5 h) at relatively high temperatures [6,7], which makes the process expensive [1,2,8]. Moreover, the long cycle time and high temperatures lead to the growth of the grains, to the detriment of the final properties.

Recent research has enabled the development of a new unconventional sintering technology that has emerged as one of the best techniques for consolidating metallic powders. Although several nomenclatures are used to describe the method, including pulsed electric current sintering (PECS), field assisted sintering (FAST), field-activated sintering technique, and current-activated pressure-assisted densification, it is often named Spark Plasma Sintering (SPS) [1,9,10]. During the last decade, the SPS technique has been used to consolidate a wide variety of materials, producing them with high density in a short processing time [11–14].

APPENDIX B - SECOND PUBLISHED ARTICLE

materials

MDPI

Article

Electric Arc Furnace Dust Recycled in 7075 Aluminum Alloy Composites Fabricated by Spark Plasma Sintering (SPS)

Elder Soares [1], Nadège Bouchonneau [1], Elizeth Alves [1], Kleber Alves [1], Oscar Araújo Filho [1], David Mesguich [2], Geoffroy Chevallier [2,3], Nouhaila Khalile [2], Christophe Laurent [2] and Claude Estournès [2,*]

[1] Mechanical Engineering Department, Federal University of Pernambuco (UFPE), Av. da Arquitetura, s/n, Recife 50740-550, PE, Brazil
[2] CIRIMAT, Université de Toulouse, CNRS, Université Paul-Sabatier, 118 Route de Narbonne, CEDEX 9, 31062 Toulouse, France
[3] Plateforme Nationale CNRS de Frittage Flash (PNF2), Module de Haute Technologie, Université Toulouse 3—Paul-Sabatier, 118 Route de Narbonne, CEDEX 9, 31062 Toulouse, France
* Correspondence: claude.estournes@univ-tlse3.fr; Tel.: +33-(0)5-6155-6109

Abstract: The reuse of industrial waste, such as electric arc furnace dust (EAFD) as reinforcement in aluminum matrix composites (AMC), is still little explored even though it has shown potential to improve the mechanical properties, such as hardness and mechanical strength, of AMCs. To propose a new alternative for EAFD recycling, AA7075-EAFD composites were produced by spark plasma sintering (SPS). The starting powders were prepared by high-energy milling with different weight fractions of EAFD in two particle size ranges added to an AA7075 matrix. SEM shows that the distribution of reinforcement particles in the matrix is homogeneous with no agglomeration of the particles. XRD patterns of initial powders and the SPS-sintered (SPSed) samples suggest that there was no reaction during sintering (no additional peaks were detected). The relative density of all SPSed samples exceeded 96.5%. The Vickers microhardness of the composites tended to increase with increasing EAFD content, increasing from 108 HV (AA7075 without reinforcement) up to 168 HV (56% increase). The maximum microhardness value was obtained when using 15 wt.% EAFD with a particle size smaller than 53 µm (called G1), showing that EAFD presents a promising potential to be applied as reinforcement in AA7075 matrix composites.

Keywords: electric arc furnace dust; waste recycling; powder metallurgy; spark plasma sintering; aluminum matrix composites

Citation: Soares, E.; Bouchonneau, N.; Alves, E.; Alves, K.; Filho, O.A.; Mesguich, D.; Chevallier, G.; Khalile, N.; Laurent, C.; Estournès, C. Electric Arc Furnace Dust Recycled in 7075 Aluminum Alloy Composites Fabricated by Spark Plasma Sintering (SPS). *Materials* **2022**, *15*, 6587. https://doi.org/10.3390/ma15196587

Academic Editor: Daniela Kovacheva

Received: 9 August 2022
Accepted: 16 September 2022
Published: 22 September 2022

1. Introduction

Electric arc furnace (EAF) technology is used for the production of steel from recycled ferrous scrap mixed with cast iron and/or direct reduced iron, but in the process, it also produces 15–25 kg of electric arc furnace dust (EAFD) per ton of steel [1,2]. EAFD, which is considered a waste product, is a generic name for powders mainly composed of oxides (principally ZnO, Fe_3O_4/$ZnFe_2O_4$), and their composition may vary on a day-to-day basis depending on the process conditions including feedstock composition, furnace temperature, production time, and the type of furnace used [3]. Moreover, EAFD is classified as hazardous by several agencies, including the Brazilian Association of Technical Standards [4], the Environmental Protection Agency [5], and the European Waste Catalog [6], due to its content of metals such as zinc, cobalt, copper, lead, and cadmium. Therefore, despite it being considered a renewable resource [7] and a secondary raw material [8], finding a suitable use for the EAFD represents a strong challenge, and some studies have reported recycling it as filler in composite materials with polymer [9,10], ceramic [11], cement [12], concrete [7], and metal matrix [13–15]. Regarding the latter, aluminum matrix composites (AMCs) in particular are of great interest because alloys such as the 7075 aluminum alloy (AA7075) exhibit characteristics (low density, high strength-to-weight ratio) that are of great